Title

Miniaturized Bio-sensing Systems for Wearable Devices in Small Animal Model Studies

Author

Xia, Xing

Publication Date

2023

UNIVERSITY OF CALIFORNIA,
IRVINE

Miniaturized Bio-sensing Systems for Wearable Devices in Small Animal Model Studies

DISSERTATION

submitted in partial satisfaction of the requirements
for the degree of

DOCTOR OF PHILOSOPHY

in Electrical and Computer Engineering

by

Xing Xia

Dissertation Committee:
Professor Hung Cao, Chair
Professor Amir Rahmani
Professor G.P. Li

2023

DEDICATION

To my parents and friends

TABLE OF CONTENTS

Page

LIST OF FIGURES

LIST OF TABLES

ACKNOWLEDGEMENTS

First and foremost, I would like to express my deep gratitude to my PhD committee members, Professor G.P. Li, and Professor Amir Rahmani. Your invaluable guidance and willingness to participate in my PhD Qualifying Exam and PhD Defense have been greatly appreciated.

My thanks also extend to the UCI faculty, staff, and alumni, who have supported me throughout my research journey. I am particularly grateful to Professor Susana Cohen-Cory for our enlightening discussions on Xenopus and tadpoles, to Professor Michelle Khine for her astute suggestions and to Professor Stuart A Kleinfelder for his beneficial courses.

I would like to recognize the Integrated Nanosystems Research Facility (INRF) staff - Marc Palazzo, Jake Hes, C.Y. Lee, Mo Kebaili and Richard Chang - for their unwavering support and invaluable education on cleanroom microfabrication. Thanks to Kaveh Shahverdi for conversations on wireless power circuits. Special thanks to Dr. Ich Tran for his expertise in material science and our engaging discussions.

I am deeply thankful to our collaborators, Professor Ron Frostig, Frostig Lab members, Dr. Mehwish Saba Bhatti, Gabriel Hui, and Jordan Saltzman. Your cooperation and guidance have been pivotal to my journey into rodent research. I also wish to acknowledge Professor Xiangmin Xu and Xu Lab members, particularly Dr. Hai Zhang, for the invaluable experience in animal surgery and experiment, as well as the inspiration derived from our collaboration. Heartfelt thanks to Professor J.-C. Chiao and his research group at Southern Methodist University, particularly Professor Chiao and Khengdauliu Chawang, for their collaboration and insightful discussions during our exploration of iridium oxide.

Also thanks to Elsevier for their permission to reuse the figures in this dissertation.

I would also like to express my appreciation to Dr. Michael Lau and Tim Etchells for their invaluable support and instructions.

My time at UC Irvine has been enriched by my labmates who have extended both friendship and academic support. Dr. Hung Anh Nguyen, Dr. Sadaf Sarafan, Dr. Paul Marsh, Dr. Jimmy Zhang, Isaac Clark, Lauren Heine, Zhenghan Xu, Justin Chen, Zhijie Zhang, Sung Sik Chu, Crystal Chien Han, Fatemeh Mohseni, Daniel Jilani, Manoj Vishwanath, Amir Naderi, Floranne Ellington, Reza Sayfoori, Tai Le, Charlie Vuong, Ramses Serefino Trigo Torres, Mao-Hsiang Huang and Mohamed Benomar - your support and inspiration have made the challenges of this journey surmountable and enjoyable. I have learned a lot from many of you, not only on research. My experiences in the HERO Lab will always be cherished. Wish you all the best of luck!

Above all, my deepest appreciation goes to my advisor, Professor Hung Cao. I value the opportunity to work on a myriad of exciting projects under your guidance in HERO Lab. I can see my huge growth in all aspects with your education and motivation.

VITA

Xing Xia

2017	B.S. in Physics, University of Science and Technology of China
2019-2023	Research Assistant, University of California, Irvine
2020-2022	Teaching Assistant, University of California, Irvine
2020	M.S. in Electrical and Computer Engineering, University of California, Irvine
2023	Ph.D. in Electrical and Computer Engineering, University of California, Irvine

FIELD OF STUDY

Biosensors in lab animal research

PUBLICATIONS

“Intravascular sensors to assess unstable plaques and their compositions: a review”. Progress in Biomedical Engineering

“Microelectrode array membranes to simultaneously assess cardiac and neurological signals of xenopus laevis under chemical exposures and environmental changes”. Biosensors and Bioelectronics

“Wireless Iridium Oxide-Based Ph Sensing Inside Small Tubes with Enhanced Stability” SSRN

ABSTRACT OF THE DISSERTATION

Miniaturized Bio-sensing Systems for Wearable Devices in Small Animal Model Studies

by

Xing Xia

Doctor of Philosophy in Electrical and Computer Engineering

University of California, Irvine, 2023

Professor Hung Cao, Chair

This dissertation addresses the challenges associated with electrophysiological research in small animal models, such as rodents, amphibians, and zebrafish, by developing and implementing miniaturized, wearable, and non-invasive biosensors. Existing methods are limited by factors like invasiveness, interference with normal activities, and potential discomfort. By refining and miniaturizing these devices using advancements in microelectromechanical systems (MEMS) technology and the electronics industry, this research seeks to improve the welfare of the animals involved, enhance the accuracy of the data collected, and broaden the applications of electrophysiological research in biology, ecology, and human health. The integration of supplementary sensors, including wearable pH sensors, high-precision tracking and location systems, and potentiostats for in vivo monitoring of metabolic substrates, allows for a more comprehensive understanding of the complex relationships between animals and their environment. A significant contribution of this research is the development of stability-enhanced iridium oxide-based pH sensors, which offer improved accuracy and reliability for environmental assessment, particularly in aquatic environments. Additionally, the integration of wireless power and data transmission methods streamlines the design of these integrated systems, enhancing their convenience and user-friendliness. The dissertation is organized into sections covering a comprehensive literature review, analysis of several animal models, detailed examination of an unconventional animal model (Xenopus laevis), introduction of the developed devices, presentation of results highlighting their effectiveness, and exploration of future research directions. Through this in-depth examination, the dissertation contributes to the advancement of knowledge in electrophysiological research involving small animal models, providing valuable insights into the intricate interactions between animals and their environment, as well as their physiological adaptations in response to various stressors.

INTRODUCTION

In the field of biological research, the utilization of various animal models is dictated by the specific research objectives and intended applications[1-5]. Smaller animal species often present a more attractive option due to several factors, including their comparatively lower maintenance costs, rapid reproductive rates, reduced ethical concerns, and the possibility for earlier handling and experimentation[6-9]. A crucial aspect of certain investigations involves understanding the subjective experiences of the animals under study. In these cases, biosensors such as electrophysiological sensors are employed to assess the animals' responses and internal states[10-14]. The correlation between electrophysiological changes and specific environmental impact factors enables researchers to gain insights into how animals adapt to and are affected by alterations in their surroundings. This knowledge is invaluable for monitoring environmental changes, understanding their potential implications for humans, and informing strategies for conservation and public health. To ensure the highest degree of reliability and validity in the data collected from these studies, it is essential that the sensors employed do not disrupt the animals' normal behavior or cause them undue distress. Consequently, there is a growing interest in the development and application of biosensors that possess several key characteristics, including wearability, compactness, wireless connectivity, non-invasiveness, and lightweight design[15]. These attributes facilitate the unobtrusive integration of the sensors into the animals' daily lives, minimizing any potential interference with their natural behaviors and enabling researchers to collect data in a more ecologically valid manner. The advancement of such biosensing technologies holds great promise for advancing our understanding of the complex relationships between animals, their environments, and the broader implications for human well-being.

Small animal models, such as rodents, amphibians, and zebrafish, have been extensively employed in electrophysiological research, with numerous biosensors specifically designed and developed for these species. Conventional electroencephalogram (EEG) and electrocardiogram (ECG) sensors have been successfully integrated into rodent models, such as mice and rats. Typically, these sensors are implanted using skull screws for surface EEG recordings and subdermal metal wires for ECG measurements. In contrast, amphibians have been relatively underutilized for electrophysiological research, with only a limited number of studies demonstrating the application of rudimentary ECG and EEG recording techniques. Zebrafish, on the other hand, have been extensively employed as animal models in various research contexts. However, due to their diminutive size and the inherent challenges associated with handling these organisms, electrophysiological measurements are often performed using needle electrodes under anesthesia.

Various stimuli or environmental modifications can be employed to elicit electrophysiological changes in these animal models. These may include drug-induced seizures, alterations in temperature or oxygen levels, and changes in water quality (particularly relevant for aquatic species). By analyzing the electrophysiological responses to these environmental perturbations, researchers can gain valuable insights into the physiological adaptations and coping mechanisms employed by these organisms, which may have broader implications for our understanding of both animal and human biology. The continued development of sophisticated, minimally invasive biosensors for small animal models is essential for advancing our knowledge in this domain and furthering the potential applications of electrophysiological research.

Despite the significant progress made in electrophysiological research involving small animal models, there remain certain limitations with existing methods that have yet to achieve optimal functionality or compatibility. Several factors contribute to these shortcomings, with the primary issues stemming from the inconvenience, discomfort, or interference with normal activities that wearable sensors may impose on the animals. Such concerns can have a detrimental effect on the reliability and validity of the results obtained from these studies, necessitating the exploration of alternative solutions. One critical area of focus in addressing these challenges is the miniaturization of the devices employed in electrophysiological research.

Advancements in microelectromechanical systems (MEMS) technology, coupled with development and innovations in the electronics industry, have accelerated the development of miniaturized biosensors and bioelectronic devices. These technological breakthroughs provide promising avenues for overcoming the aforementioned limitations. A comparison of wearable biosensors from the early 21st century to those available today reveals remarkable improvements in various aspects, including size, functionality, and overall performance.

A primary objective within this field is to harness existing resources and capitalize on the latest technological advancements in order to develop compact, minimally invasive devices suitable for use with small animal models. By persistently refining and miniaturizing these devices, researchers can mitigate the challenges associated with traditional methodologies, ultimately enhancing the welfare of the animals involved and improving the accuracy of the electrophysiological data collected. The pursuit of this objective is crucial for propelling further advancements in our understanding of the intricate relationships between animals, their environments, and the physiological adaptations they employ in response to diverse stimuli and stressors. This knowledge, in turn, holds significant implications for the broader fields of biology, ecology, and human health.

In addition to electrophysiological monitoring systems, considerable efforts have been devoted to actively incorporating various supplementary sensors to obtain additional biosignals and environmental data. Rigorous research has been undertaken to develop sensors proficient in evaluating environmental factors, such as wearable and compact pH sensors, high-precision tracking and location systems, and potentiostats for in vivo monitoring of metabolic substrates, including glucose and lactate levels. These state-of-the-art sensors enable a more comprehensive understanding of the intricate relationships between animals and their environment, as well as the effects of diverse stimuli on their physiology. Moreover, our research embeds wireless power and data transmission methods within the design of these integrated systems. The implementation of wireless technology not only enhances the convenience and user-friendliness of these devices but also contributes to a more streamlined and compact form factor. The incorporation of supplementary sensors and wireless functionalities expands the potential applications of electrophysiological monitoring systems, fostering a more holistic approach to the study of small animal models. This comprehensive methodology offers promising avenues for advancing our understanding of the complex interactions between animals and their environment, as well as the physiological adaptations they exhibit in response to various stressors.

The organization of this dissertation is structured as follows: The background section will furnish a comprehensive overview of the background and existing methods within the field of electrophysiological research, with a focus on identifying areas that demand improvement and expansion. Subsequently, we will delve into an analysis of several animal models utilized in our research, delineating their respective advantages and disadvantages, as well as the rationale behind their selection as appropriate subjects for our investigations. In particular, we will provide a detailed examination of an unconventional animal model in this field, Xenopus laevis, elucidating the reasons for their inclusion in our research endeavors. Following this, we will introduce the devices developed as part of our research, expounding upon the innovations and contributions that our work has brought to the field of electrophysiological research involving small animal models. This section will encompass a discussion of the functionality of the devices, buttressed by the presentation of results that underscore their effectiveness in practice. Moreover, we will present several pertinent projects that serve to complement and situate our research within the broader scientific landscape. Lastly, we will delineate our future plans and explore potential avenues for further research, accentuating the continued significance of advancing electrophysiological methodologies and their applications in the study of small animal models. Through this comprehensive examination of the current state of the field, our contributions, and the potential for future research, this dissertation aims to provide a thorough understanding of the challenges and opportunities inherent in electrophysiological research involving small animal models, ultimately contributing to the advancement of knowledge in this critical area of scientific inquiry.

CHAPTER 1 – Background

1.1 Animal Models

The utilization of animal models in research has been of paramount importance for elucidating various facets of human physiology, pathology, and potential therapeutic interventions. A diverse array of organisms, ranging from rodents such as mice and rats to zebrafish, amphibians, and non-human primates, have substantially contributed to the comprehension of the complexities of human biology and disease. Concomitantly, the advent and implementation of wearable sensors for these animal models have ushered in a new era in the manner in which researchers collect, monitor, and analyze data in real-time. These cutting-edge technologies furnish unparalleled insights into the animals' behavior, physiological responses, and overall well-being, rendering them indispensable tools for executing more accurate and efficacious preclinical investigations.

Rodents, particularly mice and rats, are the most widely used animal models in biomedical research, primarily due to their small size, ease of handling, and relatively low cost. Their short generation time and the availability of numerous genetically modified strains make them ideal models for studying human disease and testing wearable devices in a controlled environment. Moreover, rodents' small size allows for the development of miniature wearable devices that require less power and material, making them more cost-effective. Despite their advantages, rodents' small size can pose challenges for wearable device development. It can be difficult to design and implement sensors and devices that do not interfere with the animal's natural behavior, movement, or physiological function. Additionally, data collected from rodent models may not always be directly applicable to humans due to differences in anatomy, physiology, and behavior.

Zebrafish are a popular vertebrate model for developmental biology, gene function, and disease modeling. Their optical transparency during development, rapid generation time, and ease of genetic manipulation make them attractive candidates for developing wearable devices. The aquatic environment also allows for the development of unique sensors and devices capable of monitoring physiological parameters in real-time, both above and below water. The aquatic environment of zebrafish can create challenges for wearable device development, including issues with waterproofing, durability, and long-term stability. Additionally, the small size of zebrafish may limit the types of wearable devices that can be developed and tested in this model. Similar to rodents, data collected from zebrafish may not always directly translate to human applications.

Non-human primates, such as macaques and marmosets, offer significant advantages as animal models for developing wearable devices due to their close genetic, physiological, and behavioral similarities to humans. This makes data collected from these models more likely to be directly applicable to human populations. Additionally, their larger size allows for more complex and sophisticated wearable devices, including those designed to monitor brain activity or test novel drug delivery systems. The primary disadvantage of using non-human primates as animal models for wearable device development is the increased cost, ethical concerns, and stricter regulations surrounding their use in research. Additionally, the larger size and higher cognitive abilities of non-human primates may make it more challenging to design devices that do not interfere with their natural behavior or cause discomfort.

In conclusion, rodents, zebrafish, and non-human primates each offer unique advantages and challenges for the development and testing of wearable devices in biomedical research. Eventually, the choice of animal model depends on the specific research goals and the balance between the advantages and limitations each model presents, while acknowledging that data collected may not always directly translate to human applications. Specifically, if the goal is to develop wearable sensors for the animals, one should always consider the cost-effectiveness and feasibility of the model. As such, the size and the body structure of the model organism should be taken into account.

1.2 Wearable Biosensors

Conventional methods for biosensing often depend on large-scale signal acquisition systems, which can obstruct convenient animal monitoring. A majority of these measurements necessitate the use of anesthesia, consequently limiting the assessment's scope. In contrast, awake monitoring yields more accurate and reliable results by closely approximating the conditions of the animals' natural environment. The elimination of anesthesia allows for the observation of physiological responses and behaviors that accurately represent the animals' experiences, thereby providing a more comprehensive understanding of the underlying biological processes. Consequently, miniaturizing the system is of paramount importance in order to furnish improved tools for laboratory animal research. By reducing the size and weight of the monitoring equipment, researchers can minimize stress and interference in the animals' behaviors, thus facilitating a more accurate and ethically responsible investigation of various biological phenomena.

Incorporating wireless technology is another essential aspect of effective biosensing, especially when investigating neurological conditions such as stroke or epilepsy. Animal models of these disorders often exhibit abrupt and vigorous movements, posing significant challenges for tethered systems. The potential displacement or detachment of electrodes due to these sudden movements can undermine the quality and reliability of the collected data. By utilizing wireless systems, researchers can mitigate the risk of such complications and ensure continuous, high-quality monitoring of the animals' physiological responses and behaviors. This approach ultimately facilitates a deeper understanding of the underlying disease mechanisms and promotes advancements in the study and treatment of these conditions.

Various types of wearable biosensors have been developed to monitor different physiological parameters in animal models. Examples include devices for monitoring heart rate, blood pressure, body temperature, ECG signals, and EEG signals, among others. These devices often employ wireless technologies, allowing for continuous data collection without interfering with the animal's natural behavior. They may also incorporate advanced signal processing and machine learning techniques to analyze the collected data and detect abnormal patterns or changes in physiological parameters.

Animal wearable biosensors have numerous applications in biomedical research, including the study of disease mechanisms, the development of new therapies, and the assessment of drug safety and efficacy. They are particularly useful for longitudinal studies where continuous monitoring is required, as well as for studies involving free-roaming animals in their natural habitats. Examples of specific applications include monitoring cardiovascular function in rodent models of heart disease, assessing neurological function in non-human primates during the development of neuroprosthetics, and tracking the activity and behavior of zebrafish in studies of anxiety and stress.

Despite their potential, animal wearable biosensors also face several challenges. Some of these challenges include the development of devices that are small and lightweight enough to be worn without affecting the animal's behavior or comfort, ensuring the devices are durable and resistant to environmental factors such as water and temperature changes, and addressing ethical concerns related to the use of these devices in research. Furthermore, researchers must continue to develop advanced algorithms for data analysis and interpretation, as well as work to standardize data collection and reporting methods across different studies and devices.

1.3 Animal Models and Biosensors in Ecology

The application of animal models and biosensors in environmental assessment has been a subject of significant interest in recent literature. A growing body of research underscores the importance of understanding the effects of environmental factors on living organisms and ecosystems. Animal models, such as rodents, zebrafish, and non-human primates, have been employed extensively in these studies due to their diverse physiological and behavioral characteristics. In conjunction with biosensors, these animal models provide valuable insights into the impact of various environmental factors, including pollutants, toxins, and climate change, on health and ecological systems.

Biosensors have emerged as a powerful tool in environmental assessment, as they can measure physiological responses in animal models in real-time and often non-invasively. Recent literature has documented the development of various biosensors, such as optical, electrochemical, and acoustic sensors, for monitoring specific physiological parameters in animal models exposed to environmental stressors. These sensors can detect changes in heart rate, oxygen levels, temperature, and other vital signs, which can be indicative of an organism's response to its environment. This information enables researchers to identify potential risks and assess the effectiveness of remediation efforts.

Despite the numerous advantages of using animal models and biosensors in environmental assessment, literature reviews also highlight some challenges and limitations. One major concern is the extrapolation of data from animal models to human populations and ecosystems, as interspecies differences in physiology and behavior may limit the applicability of the findings. Additionally, the development of sensors suitable for use in diverse environmental conditions, such as extreme temperatures, humidity, or underwater settings, remains a challenge. Furthermore, ethical considerations and welfare concerns associated with the use of animal models must be carefully addressed. Moving forward, it is essential to continue refining biosensor technology and animal model selection while considering these limitations to ensure accurate and meaningful insights into environmental impacts.

CHAPTER 2 – Small Animal Electrophysiology

2.1 Overview

Electrophysiology, especially ECG and EEG are indispensable non-invasive techniques in the field of biomedical research, enabling researchers to gain insights into the electrical activity of the heart and brain, respectively. These diagnostic tools have significantly contributed to our understanding of various physiological and pathological conditions in both humans and animals. In recent years, ECG and EEG acquisition from small animals, such as rodents and zebrafish, has become crucial in advancing our understanding of cardiac and neurological functions, as well as developing novel therapies and evaluating pharmacological interventions. Despite unique challenges, including the need for specialized equipment, precise electrode placement, and species-specific considerations, these non-invasive techniques enable researchers to gain valuable insights into the electrical activity of the heart and brain in small animal models. The continuous refinement of technology and methodology ensures improved quality and reliability of data, propelling further discoveries in cardiovascular and neuroscientific research.

Significant effort has been dedicated to developing methods for electrophysiological monitoring. Compared to other signals, ECGs are generally easier to obtain due to their higher signal amplitude and easily identifiable patterns. An ECG recording comprises a series of waveforms representing various phases of the cardiac cycle. The primary components of an ECG tracing include the R peak, P wave, QRS complex, and T wave, which may vary based on differences in heart structure among animals. The R peak, typically the clearest and strongest peak in the ECG, is often used to determine overall heart rate and detect abnormal rhythms. The P wave signifies atrial depolarization, corresponding to atrial contraction and the initiation of blood flow into the ventricles. The QRS complex, formed by three individual waves (Q, R, and S), represents ventricular depolarization, which corresponds to ventricular contraction and blood ejection into the circulatory system. Finally, the T wave signifies ventricular repolarization, which corresponds to ventricular relaxation and blood refilling in preparation for the next contraction. EEG signals offer a non-invasive and direct means of observing neuronal activity across various brain regions. These signals can be analyzed in the time domain, frequency domain, or time-frequency domain to extract meaningful features. Time-domain features commonly include amplitude, waveform morphology, and event-related potentials (ERPs). Frequency-domain analysis entails decomposing the EEG signal into its frequency components using methods such as Fourier transformation or wavelet analysis, which facilitates the evaluation of spectral power and coherence between distinct brain regions. Extracted features undergo statistical analysis to discern significant differences between experimental groups or conditions. Advanced techniques, including machine learning and multivariate analysis, can also be employed to reveal intricate patterns and relationships within the EEG data.

Numerous methods have been developed for mice and rats, as they are the most frequently utilized laboratory animals. ECG monitoring in these species typically involves surface electrodes attached to the animal's limbs or chest[16, 17]. Mice and rats are often anesthetized during ECG recordings to minimize movement artifacts and alleviate stress. In some instances, implantable telemetry devices enable continuous ECG monitoring in conscious, freely moving animals. Such devices offer valuable insights into cardiac function under physiological conditions and throughout various experimental manipulations. EEG monitoring in mice and rats typically involves the implantation of electrodes into the skull, allowing for direct contact with the surface of the brain[18, 19]. The electrode placement is determined by the brain regions of interest and can be customized according to the experimental design. Following a recovery period, animals can be monitored in conscious, freely-moving conditions or during sleep. Wireless telemetry systems can be used to minimize movement artifacts and improve data quality.

Zebrafish is highly regarded in cardiovascular research due to its distinctive heart features. ECG recording in zebrafish presents unique challenges due to their small size and aquatic environment. Specialized microelectrodes are employed to record ECG signals from the zebrafish's surface, typically while the animal is immobilized[20-22]. The advent of high-speed video microscopy techniques and computer algorithms for automated analysis of zebrafish heartbeats has significantly advanced ECG research in this model organism. EEG monitoring in zebrafish also poses challenges due to their small size, weak signal, and aquatic environment. However, recent developments in miniature electrode technology have enabled neural activity recording from zebrafish[23, 24]. These innovative methods permit researchers to investigate the development and function of neural circuits in zebrafish, providing valuable insights into the evolution and conservation of brain function across species.

Obtaining simultaneous ECG and EEG recordings is often challenging. The device must be meticulously designed to accommodate the body structure of the animals, ensuring high-quality signal acquisition without causing excessive discomfort. However, due to the small size of the animals, the device must be compact enough for placement, and the electrodes require precise positioning. Additionally, the targeted signals are typically weak, necessitating efforts to minimize noise contamination in the recordings. As previously mentioned, the complexity of acquiring such signals is largely determined by the animals' body structure. For example, Error! Reference source not found. illustrate the placement of electrodes.

Figure 2. 1. Electrodes arrangement on different small animal models.

Rats, mice, and zebrafish are frequently utilized as laboratory animal model organisms. Researchers aim to establish stable electrocardiogram (ECG) and electroencephalogram (EEG) recordings from these species. The traditional method for signal acquisition involves positioning electrodes near the source: ECG electrodes near the heart and EEG electrodes above the brain. In most vertebrate animals, the heart is situated in the anterior region of the chest, while the brain is located on the opposite side. Consequently, different types of electrodes are typically employed for ECG and EEG recordings. For instance, in rodents, EEG electrodes often consist of needle or screw electrodes, which can be affixed to the animal's skull to obtain surface EEG readings. ECG electrodes are commonly implanted subcutaneously in the chest region and connected to the headstage for data output, alongside EEG signals. For zebrafish, acquiring these signals presents greater challenges due to their small body size and weak signals. Currently, there is no literature available on obtaining simultaneous EEG and ECG recordings. Owing to the weak nature of the signals, ECG acquisition requires the placement of electrodes close to the chest, sometimes even necessitating open chest surgery or penetrating needle electrodes. Acquiring EEG signals is even more challenging. With existing methods, it is nearly impossible to develop a suitable wearable device for real-time, simultaneous ECG and EEG recordings in this model organism.

2.2. Simultaneous ECG and EEG Monitoring on Xenopus Laevis

Compared to other widely used laboratory animal model organisms, Xenopus exhibits several unique advantages that enable non-invasive, simultaneous monitoring of electrophysiological signals from both the brain and the heart (**Error! Reference source not found.**). Noteworthy anatomical features, such as the heart's location, the absence of ribs, and the specialized structure of the transverse process on vertebrae, facilitate easier acquisition of posterior ECG signals compared to anterior ECG signals. Furthermore, the close proximity between the heart and brain in Xenopus and the flat, streamlined skull shape allow for the capture of ipsilateral ECG and EEG signals using a microelectrode array (MEA) on a single flexible membrane. The hairless and smooth skin of X. laevis also helps alleviate the difficulties in obtaining low-noise and stable biopotentials. These advantages enable the minimization of device size without compromising comfort and signal quality, thereby promoting the use of Xenopus as a potential model for drug screening and other research applications. Based on these insights, we developed a simple method, using microelectrode array membranes for simultaneous assessment of cardiac and neurological signals in Xenopus Laevis under chemical exposures and environmental changes. In this study, we developed a MEA featuring gold electrodes on a flexible polyimide film to simultaneously record ECG and EEG in adult X. laevis. The acquired multichannel electrophysiological signals were amplified using a differential amplifier and digitized by an analog-to-digital converter (ADC) for subsequent data analysis. Our system facilitated the monitoring of ECG and EEG signals under drug exposures and temperature variations. The system demonstrated rapid and accurate responses to phenotypic changes, highlighting its potential and practicality for developing compact wearable electrophysiology monitoring devices based on X. laevis for various biological studies and monitoring applications.

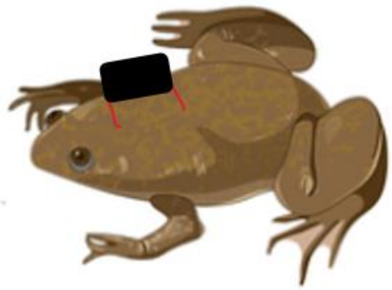

Figure 2. 2. Possible electrode placement on Xenopus Leavis.

2.2.1 Microelectrode Array Fabrication

To ensure biocompatibility and flexibility of the sensors for uniform and secure contact with Xenopus skin, we fabricated electrodes on polyimide films with varying thicknesses ranging from 25 to 125 μm (Kapton, Dupont, Wilmington, DE, USA). The fabrication process is illustrated in Error! Reference source not found., began with the deposition of a 20 nm Cr and 200 nm Au layer on Kapton polyimide films using E-beam evaporation (Temescal CV-8). Shipley 1827 photoresist was then spin-coated and patterned using conventional photolithography procedures. Following this, uncoated Au and Cr were etched off by wet etching, and the photoresist layer was removed using an organic solvent. Next, another layer of photoresist was spin-coated, and this layer was subsequently patterned and baked to form a hardened protective layer with sensing pads and contact pads exposed (Shipley 1827, MICROPOSIT).

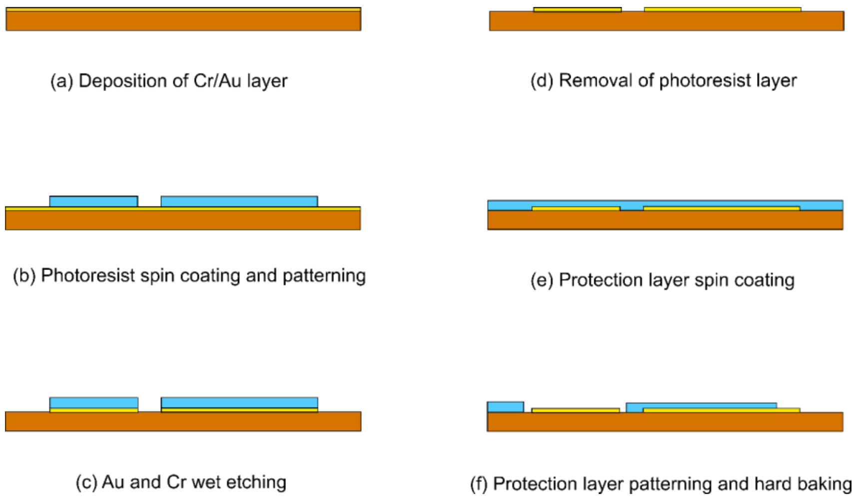

Figure 2. 3. Fabrication procedure of the flexile electrodes.

In accordance with Xenopus brain structure, we positioned the 4-channel EEG recording electrodes on the scalp above the right and left sides of the telencephalon and mesencephalon (Error! Reference source not found.**. A**). The reference electrode was situated above the cerebellum's center. Three total lengths (25, 35, and 45 mm) of MEAs were designed to accommodate different flexibility requirements. The ECG recording electrodes were integrated on the 35- and 45-mm membranes. The distance between the ECG electrode and the reference electrode was 20 mm, corresponding to the average heart-brain distance of Xenopus we measured. The ECG and EEG recording electrodes shared a common reference electrode. The baseline noises in ECG caused by brain signals from the cerebellum area can be filtered out through additional signal processing. The electrodes were traced to contact pads with a size of 2 mm × 0.35 mm each, fitting Flat Flexible Cable (FFC) connectors (5034800, Molex, Lisle, IL). An auxiliary printed circuit board (PCB) was designed to improve connections between the electrodes and the cables leading to the subsequent signal collection system. On the PCB, a FFC connector with a 0.5 mm pitch was routed to a 2-row, 2.54 mm female socket header connector. The flexible electrode membrane could be easily inserted and locked into an FFC connector, and the signal transmitting cables were connected to the female sockets on the PCB using male pin headers (Error! Reference source not found.. **B**).

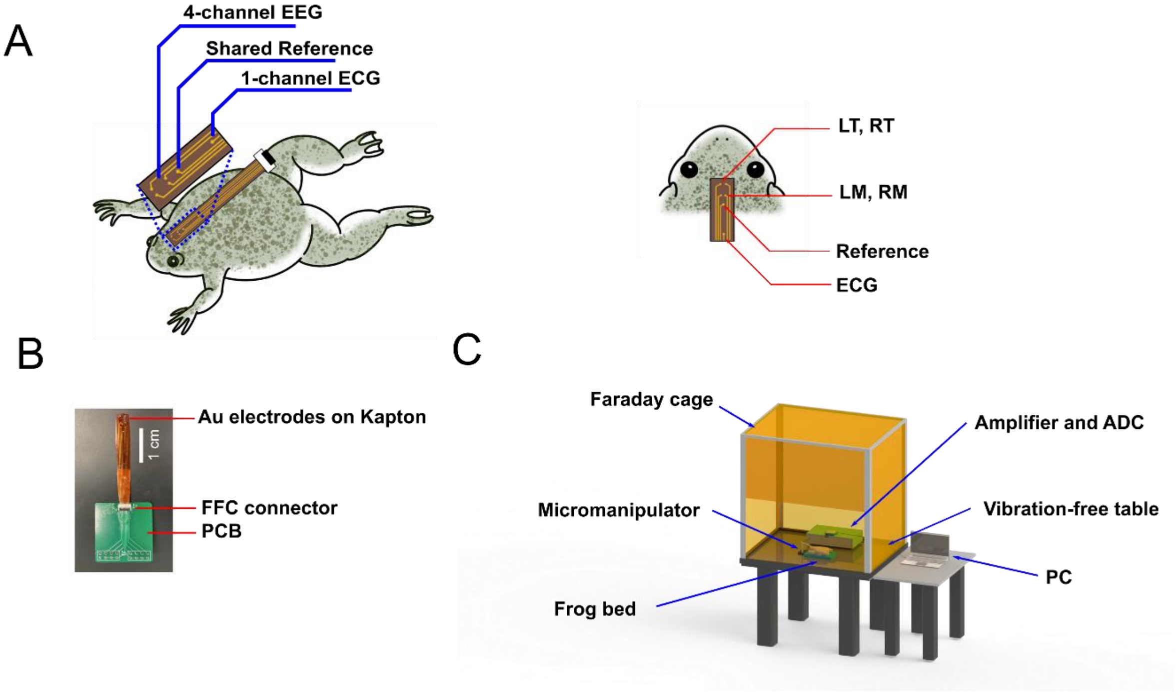

Figure 2. 4. The experimental setup and devices to record EEG and ECG simultaneously.

2.2.2 Methods and Experimental Setup

X. laevis were deeply anesthetized by immersion in a buffered solution of 1.5 g/L tricaine methane sulfonate (MS-222). The subjects were deemed sufficiently anesthetized upon the loss of toe pinch response. Following anesthesia, the Xenopus were placed on a polydimethylsiloxane (PDMS) test bed, specifically designed with a concave surface to accommodate the anatomical shape of Xenopus. Subsequently, the MEA was positioned dorsally based on the brain and heart locations and secured using a manual micromanipulator (M3301, World Precision Instruments Inc., Sarasota, FL) to minimize vibrations. Due to differential shrinkage between the Xenopus skin and the Kapton membrane, the electrodes adhered to the skin automatically, enhancing electrical conductivity. During the recordings, the anesthetized Xenopus and accompanying devices were placed in a Faraday cage on a vibration-free table. The signals were amplified 10,000-fold by a differential amplifier (A-M Systems Inc. 1700 Differential Amplifier, Carlsberg, WA) and filtered between 1 and 500 Hz with a 60 Hz cut-off frequency (notch). The filtered signals were then digitized at a sampling rate of 1,000 Hz using a Data Acquisition Hardware (National Instruments USB-6251 DAQ device, Austin, TX, and LabVIEW) and stored for further data analysis. The complete system setup is illustrated in Error! Reference source not found.**.** **C**.

PTZ-induced epilepsy and anti-epileptic drug (valproic acid (VPA)) experiments were conducted to validate the system for drug exposure. Due to the exceptional absorbability of

Xenopus skin, the subjects were treated by direct immersion into drug solvent. The Xenopus were placed into a container filled with 200 mL of drug solvent, with their eyes and noses above the solvent level. The drugs were passively transported. Compared to injection, this method took longer to be effective. In this study, 30 mM PTZ dissolved in 1.5 g/L MS-222 was used for PTZ exposure. The Xenopus were immersed in PTZ solution for 15 minutes. For VPA treatments, the Xenopus were immersed in 3 mM VPA solution for 1 hour. During the drug treatment, the containers were covered with lids to prevent the Xenopus from escaping. After recordings, the Xenopus were moved to a tank with flowing water to aid in recovery from anesthesia and drug effects. It took approximately 30 minutes for Xenopus to fully recover. The drug-treated Xenopus were separated and maintained in recirculating tanks for 7 days.

A series of temperature-dependent electrophysiology measurements were performed. Once the Xenopus were fully anesthetized, 15-minute recordings were taken with the subjects immersed in MS-222 solution (21°C, 1.5 g/L). The anesthesia solution was then replaced with pre-chilled MS-222 solution (12°C, 1.5 g/L), introduced into the experimental setup gently without any electrode displacement. The recording continued for 15 minutes while the temperature of the bath was continuously monitored using a digital aquarium thermometer. Upon completion of the recordings, the Xenopus were allowed to recover in freshwater for 30 minutes at room temperature before being transferred to a separate aquarium.

Accurate detection of ECG characteristics relies heavily on noise cancellation. The low-pass filter and Savitzky-Golay finite impulse response (FIR) smoothing filter (SG filter) were employed to suppress powerline interference and remove baseline wander. The baseline drift caused by respiration could be normalized using a low-pass filter. The SG filter, proposed by Savitzky and Golay, is based on local least-squares polynomial approximation and has been demonstrated as one of the most popular noise cancellation and smoothing methods.

The acquired EEG signals were filtered using a 6th-order Butterworth bandpass filter from 0.5 – 40 Hz, based on the frequency bands of interest, which include delta (0.5 - 4 Hz), theta (4 – 8 Hz), alpha (8 – 12 Hz), beta (12 – 30 Hz), and gamma (> 30 Hz). The Fourier transform (FFT) of the filtered signal was then calculated and visually compared between different groups to analyze the differences in frequency compositions of the signals. For analyzing the temperature effects on EEG, similar procedures were performed. The power of EEG recording was calculated in the aforementioned frequency bands and compared across the two temperature settings. Relative power of different frequency bands was analyzed using the formula:

Accurate detection of ECG characteristics relies heavily on noise cancellation. The low-pass filter and Savitzky-Golay finite impulse response (FIR) smoothing filter (SG filter) were employed to suppress powerline interference and remove baseline wander. The baseline drift caused by respiration could be normalized using a low-pass filter. The SG filter,

proposed by Savitzky and Golay, is based on local least-squares polynomial approximation and has been demonstrated as one of the most popular noise cancellation and smoothing methods.

The acquired EEG signals were filtered using a 6th-order Butterworth bandpass filter from 0.5 – 40 Hz, based on the frequency bands of interest, which include delta (0.5 - 4 Hz), theta (4 – 8 Hz), alpha (8 – 12 Hz), beta (12 – 30 Hz), and gamma (> 30 Hz). The Fourier transform (FFT) of the filtered signal was then calculated and visually compared between different groups to analyze the differences in frequency compositions of the signals. For analyzing the temperature effects on EEG, similar procedures were performed. The power of EEG recording was calculated in the aforementioned frequency bands and compared across the two temperature settings. Relative power of different frequency bands was analyzed using the formula:

$$Relative\ band\ power\ = \frac{Power\ in\ specific\ frequency\ band}{Total\ power}$$

These calculations were performed using the bandpower function in MATLAB, which employs a modified periodogram to determine the average power in a specific frequency range.

These calculations were performed using the bandpower function in MATLAB, which employs a modified periodogram to determine the average power in a specific frequency range.

2.2.3 Results

Four-channel EEG and single-channel ECG signals were obtained from 24 Xenopus, which were divided into four separate groups and subjected to different drug exposures. Each recording session lasted between 20 and 40 minutes, depending on how long the Xenopus remained in deep anesthesia. Anesthetizing the Xenopus fully took approximately 12 minutes with a 1.5 g/L MS-222 solution. When the Xenopus no longer exhibited toe-pinch reactions, we transferred them from the anesthesia solution to the test bed. Positioning the Xenopus and adjusting the MEA membrane took an additional 2-3 minutes. Following these steps, experimenters moved away from the experimental area to minimize any disturbances to the recordings. We tested three distinct lengths (25 mm, 35 mm, 45 mm) and thicknesses (25 µm, 75 µm, 125 µm) of the polyimide membrane. The 75-µm thick, 25-mm long probe, and the 125-µm thick, 35-mm and 45-mm long probes demonstrated the best performance. These probes exhibited flexibility and strength similar to Xenopus skin, resulting in significantly enhanced conformability and longevity. In some recordings, excessive mucus on the Xenopus scalp caused noisy EEG signals. By gently wiping the area with paper towels before applying the electrodes, the signal quality improved substantially. All experiments took place in a Faraday cage on a vibration-free table, ensuring a favorable signal-to-noise ratio (SNR).

A representative recording of PTZ-treated Xenopus four-channel EEG is depicted in Error! Reference source not found.. **A**. Signals were collected from electrodes positioned near the left and right sides of the telencephalon (LT and RT) and the left and right sides of the mesencephalon (LM and RM). This recording segment included 20 seconds of normal EEG (baseline), followed by 20 seconds of EEG during epileptic seizures. Periodic sharp spikes exhibiting a significantly higher amplitude than the baseline EEG were observed and used as criteria for ictal seizures Error! Reference source not found.. **B** displays the typical EEG patterns before and after each epileptic seizure. There were periods where signals had substantially higher amplitude spikes compared to regular EEG. We classified these periodic spikes with 200-600 μV high amplitudes as ictal events. During the 20-second recording, two ictal events occurred. High amplitude spikes in ictal events appeared 3-5 times per second, with each ictal event containing 5-10 such spikes, consistent throughout the entire recording. Between the two ictal events, less frequent periodic bumps with lower amplitude and less sharpness were detected. We identified these bumps as interictal events. Interictal events only emerged after the first appearance of an ictal event and disappeared before the ictal events ended. The small spikes of interictal intervals were around 40 μV, occurring 1-2 times per second. The control group did not exhibit ictal and interictal events due to the absence of focal epilepsy. Furthermore, a closer examination of the four-channel EEG during seizure events is provided in Error! Reference source not found.. The EEG signals obtained from different locations displayed unique patterns and amplitudes, indicating the approximate origins of epileptic neural activities.

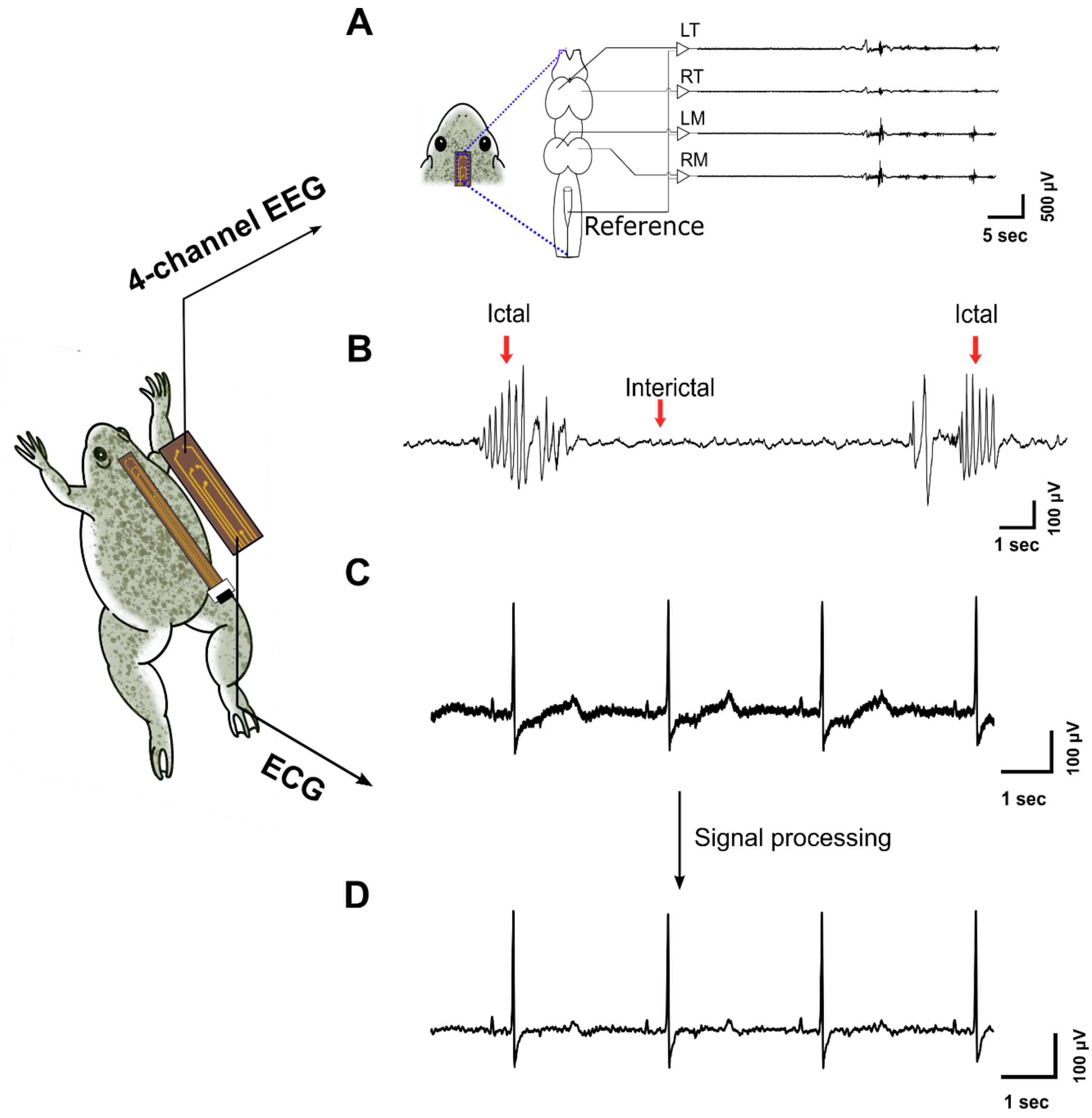

Figure 2. 5. The experimental setup and devices to record EEG and ECG simultaneously.

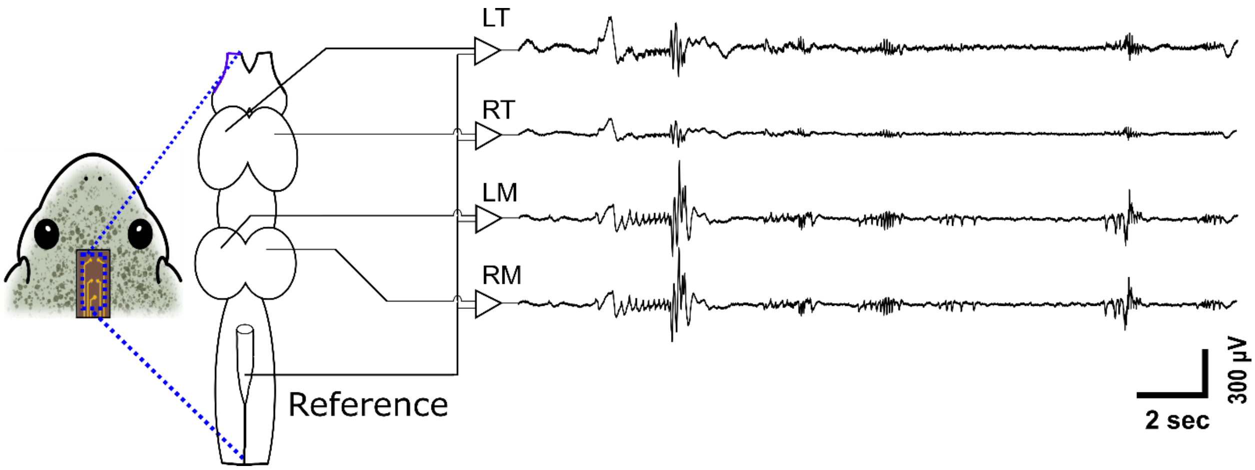

Figure 2. 6. 4-channel EEG during seizure events.

Simultaneous ECG signals were recorded using working electrodes dorsally positioned near the heart. Due to the short heart-brain distance in Xenopus, the ECG recording electrode was placed close to the four-channel EEG electrodes, reducing the size of the MEA membrane to less than 2 cm × 0.5 cm while maintaining high-quality ECG and EEG recordings. We also opted to use a single ECG/EEG reference electrode, positioned on the Xenopus cerebellum, to further minimize device size and maximize animal comfort during monitoring. Although mixed ECG and EEG signals were obtained from the same channel, the recorded ECG signals were of sufficient quality for morphological analysis. Error! Reference source not found.. **C** illustrates an example of a raw signal segment recorded by the ECG electrodes. The R peaks had amplitudes around 250 µV, significantly higher than the baseline noise (less than 20 µV). The R peaks were discernible without additional filtering, allowing for manual extraction of heart rate (HR) and R-R intervals. We also experimented with recording ECG using an individual ECG reference electrode placed on the Xenopus's right leg. While this approach provided better ECG signals, the trade-off between total size and signal quality made it less ideal. Error! Reference source not found.**.** **D** displays the ECG signals after noise cancellation and smoothing filtering. Following data processing, the PQRST waves were clearly defined.

Before finalizing the placement of the electrodes, we tested ECG electrodes at different locations and compared the signal quality. As shown in Error! Reference source not found., the unique location of the Xenopus heart and the relative dorsolateral derma plica enabled dorsal ECG signal recording without losing crucial ECG information. This discovery encouraged us to implement ipsilateral ECG and EEG recordings. Additionally, the distinct neck structure of Xenopus not only flattens their dorsum but also significantly reduces the distance between the heart and the brain. These characteristics of Xenopus combined to enable simultaneous ECG and EEG recordings using electrodes fabricated on a single, small, flexible substrate, further minimizing device size. These findings strongly support the natural advantages of using Xenopus as a model for simultaneous ECG and EEG monitoring. We also compared ECG signals recorded by the same system from humans, zebrafish, and Xenopus, as shown in Error! Reference source not found..

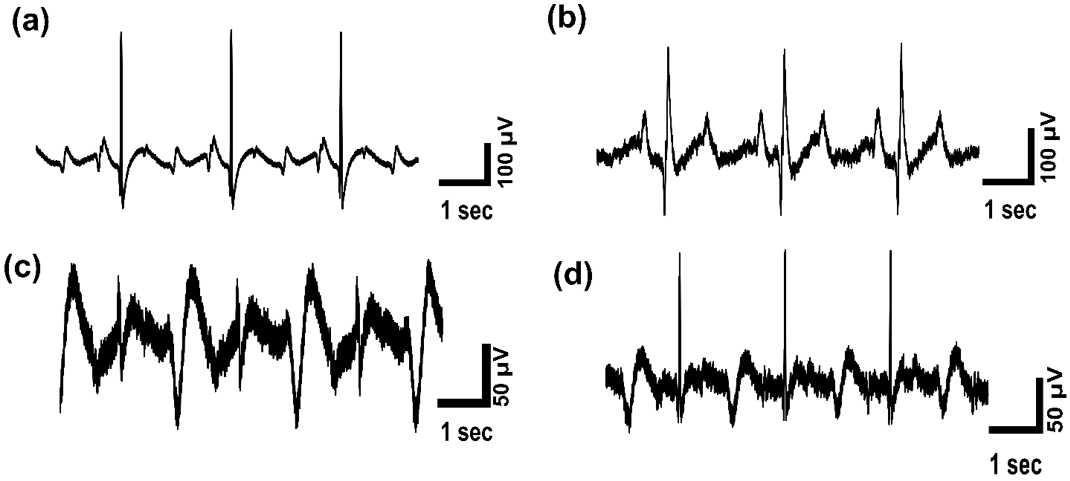

Figure 2. 7. ECG recorded by the electrodes placed on different locations.

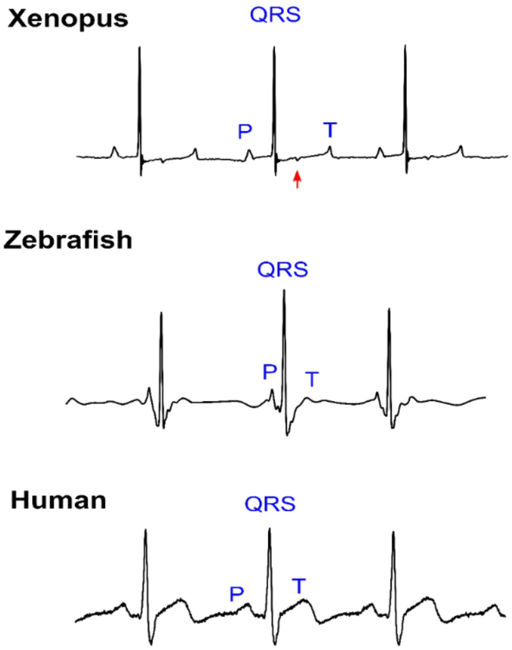

Figure 2. 8. ECG patterns of Xenopus, zebrafish, and human.

The majority of electrophysiology recording systems for small animal models focus on rodents or zebrafish, while other animal models remain largely unexplored. In our study, we demonstrate the feasibility of electrophysiology recording in Xenopus as a promising alternative, offering substantial potential in diverse applications owing to its unique advantages. Capitalizing on these unique advantages, we can readily investigate environmentally induced cardiac and neurological influences by analyzing simultaneous ECG and EEG recordings in Xenopus. Here we provide two example applications with the results.

ECG and EEG signals were recorded and analyzed from four groups of Xenopus. A total of 24 Xenopus were divided according to different drug treatment conditions: (1) PTZ group, in which Xenopus were treated with a 200 mL solution containing 30 mM PTZ mixed with 1.5 g/L MS-222; (2) VPA+PTZ group, where they were immersed in a 5 mM VPA solution for 1 hour before being transferred to the same PTZ treatment as the PTZ group; (3) VPA group, in which Xenopus were treated with 5 mM VPA for 1 hour, then transferred to MS-222 solution; and (4) Control group, with no drug treatment administered before anesthesia. Each Xenopus was anesthetized in 1.5 g/L MS-222 and then recorded for more than 25 minutes.

Typical 1500-second-long recordings of raw EEG signals from the control, PTZ, and VPA+PTZ groups are demonstrated in Error! Reference source not found.**. A-C**, respectively. The 1500-second-long samples were recorded by the LT working electrodes (channel 1); the other three EEG channels showed similar results statistically, as all channels were able to record the same number of ictal events. The obtained signals of the experimental groups were noticeably different in the occurrences and amplitudes of PTZ-induced seizures. EEG recordings in the control group did not show any occurrence of seizures, with an average amplitude of 10 μV. In the PTZ and VPA+PTZ groups, the ictal event occurrence, previously identified by spikes in amplitudes of 200-600 μV, was 34 times and 2 times, respectively. However, upon closer examination of the EEG patterns in the VPA+PTZ group, we found the average amplitudes of the ictal spikes decreased by 81.0%, from 370 μV to 70 μV. Taking this factor into account, the criteria for an ictal event in the VPA+PTZ group were adjusted to 37.8-113.5 μV, proportional to the decrease in spike amplitudes. After recalculation, the ictal events in the VPA+PTZ group in the 1500-second-long recording appeared nine times, resulting in a 73.5% reduction compared with the PTZ group subjects. These results confirmed that VPA can alleviate PTZ-induced seizures in terms of occurrences and intensities, which is consistent with studies on other models. The recordings obtained from different groups also validate our device's capability and longevity for collecting high SNR EEG in long-term monitoring.

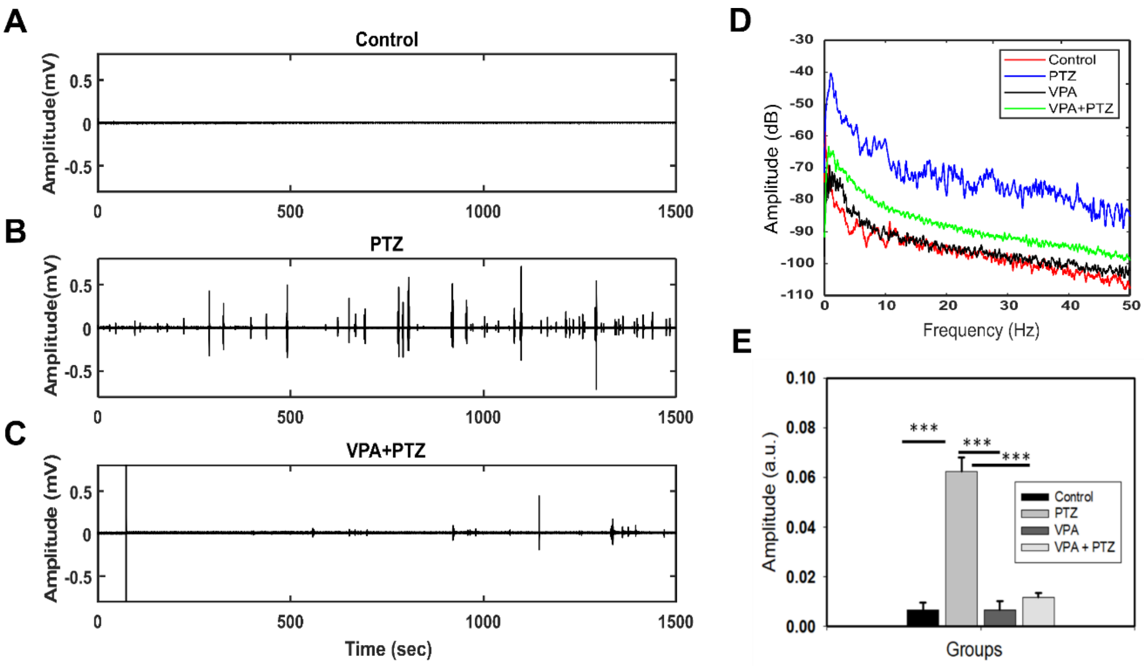

Figure 2. 9. PTZ and VPA effects to Xenopus EEG.

The Fast Fourier Transform (FFT) spectra, averaged across the four recorded channels of the four groups, are shown in Error! Reference source not found.. **D**. These spectra quantify the number of different frequency components present in the given signal. In general, all four groups exhibited higher amplitudes in low frequencies, a characteristic of all EEG signals. It is observable that the amplitude of the PTZ group was 30 dB higher than the control and VPA groups for the entire frequency range (0-50 Hz). The average amplitude of EEG signals in the four groups was also calculated and compared, as shown in Error! Reference source not found.. **E.** The control and VPA groups did not exhibit noticeable differences, indicating that VPA did not cause significant EEG changes in the frequency domain. With PTZ exposure, the average EEG amplitude increased by 833.9% compared to the control group. In the VPA-treated groups, the amplitude increased by 70.0% after PTZ immersion, resulting in a 91.6% mitigation of PTZ effects. The average amplitude in the control and VPA-treated groups did not show significant differences, which indicated that VPA did not have a mitigating effect on non-seizure EEG amplitude.

Electrocardiogram (ECG) alterations resulting from drug exposure were observed in our study. We analyzed heart rate (HR), R-R intervals, QTc intervals, and morphological features of Xenopus ECG. Average HR was computed at 2-minute intervals for each Xenopus post-pentylenetetrazole (PTZ) treatment. Owing to considerable variation in HR among individual Xenopus (ranging from 11 to 52 bpm in our dataset), relative heart rate (RHR), defined as the instantaneous HR divided by the mean HR for the entire recording, was employed to represent HR fluctuations. Error! Reference source not found.. **A** displays the mean RHR variation for the six Xenopus following PTZ administration. The initial manifestations of epileptic seizures were ascertained from concurrently recorded electroencephalogram (EEG) signals. The onset of an ictal event in EEG signals marked the transition between the preictal and ictal stages. This boundary emerged approximately 10 minutes into the ECG recordings, and the two stages were denoted using distinct colors in the figure.

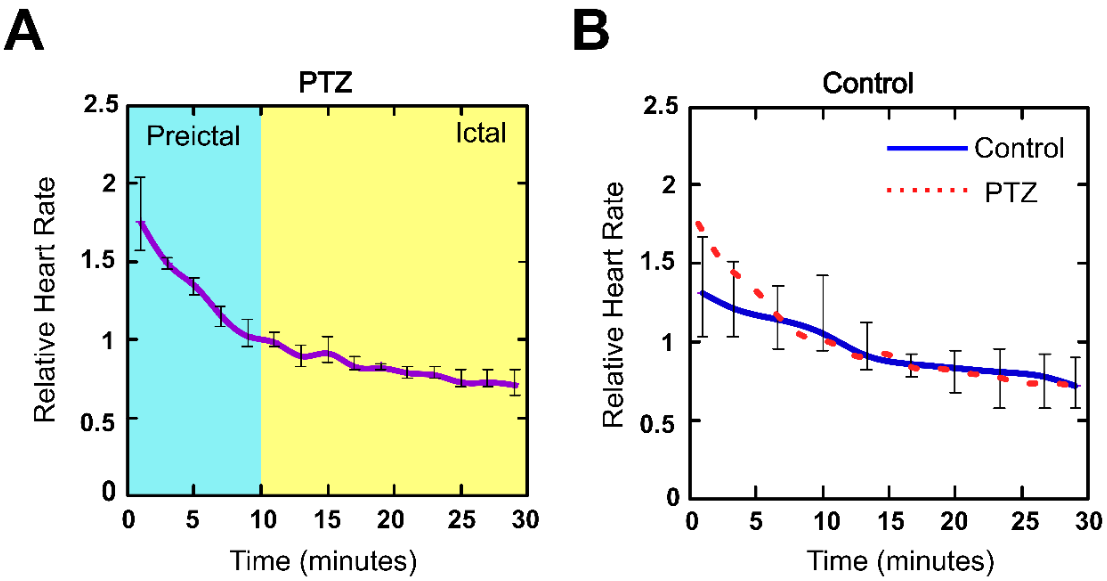

Figure 2. 10. Relative heart rate altering.

Examination of the Xenopus HR trends within the PTZ group revealed no RHR increase during seizure events. In fact, HRs were lower in the ictal stage than in the preictal stage for all tested Xenopus. To assess the impact of anesthesia on HR, a control group comprising Xenopus treated solely with MS-222 at the same concentration and duration as other experimental groups was established. Error! Reference source not found.. **B** presents RHR variation during 30-minute recordings for the control group, with the PTZ group's RHR curve depicted as a red dotted line for comparison. Both groups exhibited similar HR fluctuations between the 10th and 30th minutes of recording, designated as the ictal stage for the PTZ group. However, the RHR variation during the preictal stage for the control group was more moderate. This comparison suggested that PTZ induced transient increases in HR that subsequently normalized. Furthermore, HR did not elevate when ictal events were detected in EEG signals, signifying the onset of epileptic seizures.

PTZ administration additionally induced morphological alterations in ECG patterns; however, these changes were not consistent across all Xenopus. Within the PTZ group, one Xenopus exhibited progressively inverted T waves during recording. Error! Reference source not found.**. A** presents the post-PTZ treatment ECG, with four intervals selected: (a) the recording's commencement, (b) the preictal period's conclusion, (c) the ictal events' initiation, and (d) the recording's termination. From (a) to (d), R-R intervals increased from 1.7 to 4.7 seconds, while T waves transitioned from upright in (a) and (b) to flat in (c) and ultimately inverted in (d). Apart from T waves, no significant morphological changes were observed for other waves, as illustrated in the figure.

Another Xenopus experienced a three-minute arrhythmia episode during seizure onset, as shown in Error! Reference source not found.**. B**. The arrhythmia manifested immediately after the first ictal event. R-R intervals were approximately 2.8 seconds both before and after the three-minute arrhythmia period. During the arrhythmia, heartbeats occurred in pairs, characterized by one rapid and one slow rhythm, with R-R intervals of 1.6 and 2.7 seconds, respectively. In comparison, ECG morphology remained relatively stable for all subjects in the control group.

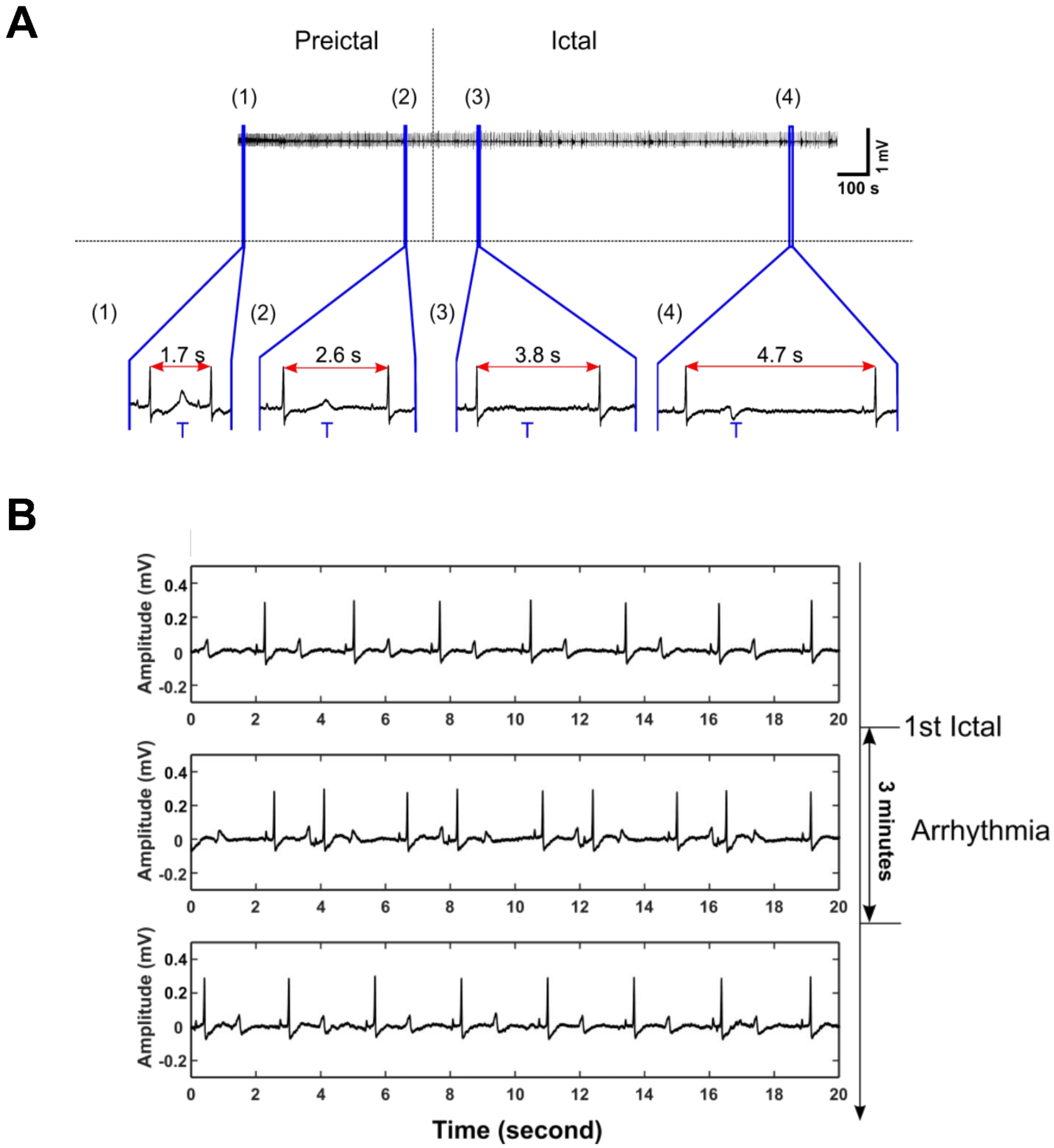

Figure 2. 11. Abnormal ECG found in PTZ-treated Xenopus.

The experiments adhered to the timeline illustrated in Error! Reference source not found.. **A**, with temperature and RHR changes during the experiment presented in Error! Reference source not found.. **B**. Prior to the introduction of the cold MS-222 solution, the temperature remained stable, whereas the cold tricaine temperature subsequently increased along a quasi-logarithmic curve. HR alterations were derived from ECG signals, with the mean RHR for four Xenopus calculated and displayed as a red dotted line. The RHR exhibited a minor increase from 0.95 to 1.08, which was less pronounced compared to the PTZ results. The influence of cold temperatures on the relative band power of distinct EEG bands is evident in Error! Reference source not found.. **C–F**: Figure 12.C displays the relative band power trends of the recorded EEG signals, encompassing the average, maximum, and minimum relative band power of the samples in the Delta wave band; Figure 12.D in the Alpha wave band; Figure 12.E in the Theta wave band; and Figure 12.F in the Beta wave band.

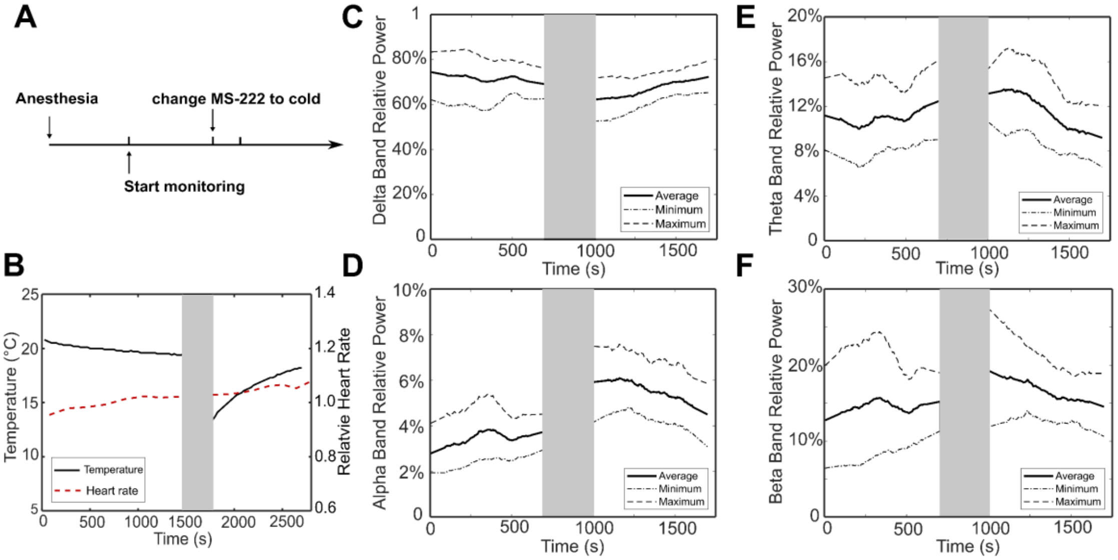

Figure 2. 12. Temperature dependent EEG

For the Delta band, the relative power remained stable until the temperature dropped, at which point the cold MS-222 solution was introduced. The relative band power decreased by an average of 7.0% and subsequently rose from 62.1% to 72.3% over the following 700 seconds, while HR remained constant throughout the measurement. More marked changes were observed in the Alpha band, as depicted in Error! Reference source not found.. **D**. The relative power increased by 59.4%, from 3.7% to 5.9%, during the cold MS-222 solution exchange. Post-introduction of the cold solution, the Alpha relative band power declined from 5.9% to 4.4% over 700 seconds. The Theta and Beta relative band powers exhibited trends similar to those of the Alpha band (Error! Reference source not found.. **E and F**). Overall, the Alpha band relative power experienced the most significant fluctuations in response to temperature changes. High-frequency signals increased and then gradually returned to normal levels while Xenopus remained in cold environments, whereas low-frequency signals in the Delta band exhibited the opposite trend.

Amphibians are particularly susceptible to climatic condition changes due to factors such as physiological processes and temperature- and moisture-dependent breeding patterns. Limited dispersal capacity implies that alterations in external climatic conditions may result in minor evolutionary differences among various population groups. Considering that Xenopus is among the most geographically widespread amphibians, inhabiting four continents (North America, South America, Europe, and Asia), and that climate change is likely to increase Xenopus invasion potential and population growth [25], its employment as a model organism to investigate global environmental changes is essential.

2.2.4 Conclusion

In this study, we developed a multichannel ECG-EEG recording system for use with Xenopus. Although X. laevis has not been extensively employed in electrophysiological monitoring research, we identified considerable potential for utilizing this animal model in environmental monitoring and drug screening applications. The flexible MEA membrane, placed dorsally on anesthetized Xenopus, noninvasively recorded ECG and EEG signals simultaneously. The sensor is compact and simple to set up. The PTZ and VPA drug tests, along with the temperature control test, demonstrated the system's feasibility for real-time

ECG and EEG monitoring in relation to neurological and cardiovascular conditions. Both signals exhibited discernible and unique characteristics during various seizure stages. Given Xenopus' excellent skin permeability and the ease of obtaining electrophysiological signals, it may serve as a suitable model for sensing and monitoring chemical exposure and environmental changes. Future work will involve developing a miniaturized system using a more flexible substrate, such as parylene C, incorporating embedded microelectronics and wireless communication. This advancement will enable the monitoring of awake electrophysiological signals without interference from Xenopus behavior. Overall, the real-time electrophysiology monitoring system using the Xenopus model holds potential for many applications in drug screening and remote environmental monitoring.

CHAPTER 3 – Wearable Electronics Systems

3.1 Overview

Biosensors function as essential transducers, converting biosignals or characteristics of biomarkers into electrical signals that can be collected and quantified by corresponding bio-electronics systems. These devices capture and translate biological phenomena, offering invaluable insights into an organism's physiological processes, cellular mechanisms, and molecular interactions. Electronic systems for biosensing are integral to advancing our understanding of diverse biological processes and phenomena. These systems employ state-of-the-art technologies that facilitate the acquisition, processing, and analysis of biological signals from living organisms. Ongoing advancements in microelectronics and nanotechnology have enabled the miniaturization of biosensors, considerably improving their portability and applicability across various contexts. Moreover, the incorporation of wireless communication and low-power consumption components has broadened the potential for real-time, continuous monitoring, empowering researchers to examine physiological responses and behaviors of subjects in their natural habitat. As the field of biosensing progresses, it is expected that cutting-edge electronic systems will propel groundbreaking discoveries in life sciences and foster the development of increasingly effective diagnostic tools and therapeutic interventions.

Figure 3. 1 depicts the typical signal path of an electronics system, wherein the signals undergo a series of transformations, filtering, amplification, and digitization. Initially, biosensors convert bio-signals into electrical signals, which may include voltage or current signals. These signals are generally characterized by low amplitude (microvolts, nanoamps, or even lower) and are prone to interference from external environmental noise. Subsequently, the signals pass through the first stage filter and are amplified by an amplifier. This step adjusts the signals to fit within the conversion range of the analog-to-digital converter (ADC). Following the second stage of filtering, the signals are digitized by the ADC, transforming them into data that can be transmitted to subsequent stages. Wireless data transmission can be employed at this juncture to transmit the digital data, further optimizing the process and enhancing the system's overall efficiency and versatility.

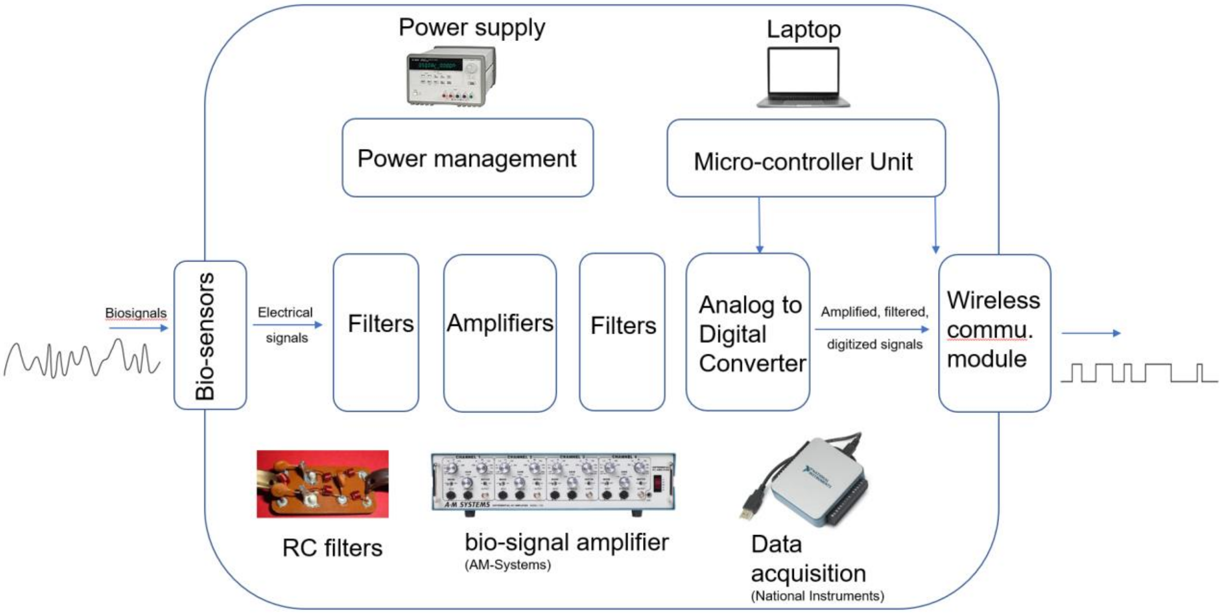

Figure 3. 1. Electronics system diagram of a wearable devices with the common functional blocks

Generally, traditional electrophysiological measurements employ and combine specialized instruments, such as power supplies, biosignal amplifiers, data acquisition systems, and standalone filters. These setups tend to be bulky, cumbersome, and necessitate a dedicated laboratory space for operation. The objective of developing the aforementioned system is to miniaturize and integrate all components onto a compact, centimeter-scale printed circuit board (PCB) that is lightweight enough to be carried by animals. In addition to the benefits previously discussed, the localized acquisition and processing of signals yield results that are more closely aligned with reality and exhibit less noise from transmission cables. The subsequent paragraphs will address the selection of components that meet these requirements.

The properties of biosensors exhibit significant heterogeneity across different sensor categories. Although the mechanisms and contributing factors vary among distinct sensors, the dominant output modality is consistent, presenting as electrical signals. Sophisticated electronic systems are designed to improve the detectability and resolution of these signals, thus facilitating their analysis in subsequent data processing stages. However, as the primary focus of the electronic systems discussed in this chapter is not on biosensors, a comprehensive examination of their intricacies will not be included.

Biosignals characteristically exhibit low amplitudes and include environmental noise, necessitating the use of filters to eliminate such interference. Low-frequency noise, such as motion-induced disturbances, can be particularly prominent; if not removed before amplification, the amplifier's output may be dominated by this low-frequency noise, potentially resulting in saturation. First-stage filters often incorporate a high-pass filter, such as a capacitance-resistance (CR) filter, to initially process input signals. CR filters utilize a combination of capacitors and resistors to selectively permit specific frequency ranges to pass through while attenuating others. Owing to their simplicity, cost-effectiveness, and ease of implementation, CR filters remain a popular choice in bioelectronics applications. The 3-decibel (dB) attenuation frequency is determined by the capacitor and resistor values, which can be expressed by the following equation:

$$f\_c = 1 / (2\pi RC)$$

In practical applications, resistor and capacitor sizes are typically related to their values. This relationship becomes more critical in designs with limited size, such as wearable electronics systems for animals, where filters often employ 0201-sized resistors and capacitors to achieve a compact design. As of 2023, the currently available capacitor with the highest capacitance in the 0201 size is 4.7 µF (based on search results from Digikey). For resistors, an additional consideration concerning thermal noise is related to the resistance value. Meanwhile, thin-film resistors are generally preferred due to their superior noise performance. The currently available thin-film resistors in 0201 sizes have a maximum value of 73.2 kOhms (based on search results from Digikey). By substituting the values into the equation, the calculated high-pass filtering cut-off frequency is determined to be 0.46 Hz. This frequency represents the maximum attainable value and is essentially sufficient to filter out motion noise while preserving higher frequency signals, such as those found in ECG.

Following the initial filtering stage, the signals are typically amplified by an amplifier to ensure that the signal amplitude aligns with the input requirements of the Analog-to-Digital Converter (ADC). Amplifiers for low-amplitude biomedical signals are meticulously designed, taking several essential aspects into account. Gain is the most fundamental consideration; the acquired signal amplitude and the input range and resolution of the subsequent stage dictate the gain selection to optimize signal quality. Input impedance is critical for weak electrical signals, as low input impedance may lead to signal attenuation.

The Common-mode Rejection Ratio (CMRR) is another vital parameter, particularly for differential signals such as those found in electrocardiograms (ECG) and electroencephalograms (EEG). CMRR is a measure of an amplifier's ability to reject common-mode noise. A high-quality biosignal amplifier typically has a CMRR of around 100 dB. Additionally, other factors such as low power consumption and feedback driving signals (e.g., Right Leg Drive) are considered desirable attributes for amplifiers in these applications. In general, an effective amplifier should be able to provide the best signal-to-noise ratio (SNR) after amplification while meeting the ADC's input requirements. Instrumentation amplifiers are often excellent options, as the extra stage of amplification offers very high impedance while maintaining low noise levels and low distortion in the signal.

The second-stage filter is positioned after the amplifier stage and before the ADC stage. An RC low-pass filter is often placed before the ADC stage to eliminate high-frequency noise before the signals are digitized. The cutoff frequency is calculated similarly to the high-pass filter, as demonstrated by the equation provided earlier. Typically, the cutoff frequency is set around 5 kHz to 50 kHz for electrophysiological signals. Signals with frequencies higher than 10 kHz are generally not of interest, and if the ADC is sampling at a lower or similar rate, the high frequency noise can significantly influence the results.

The Analog-to-Digital Converter (ADC) is another crucial component in biosignal acquisition. Resolution plays a vital role, as higher resolution ADCs offer improved signal representation, which is particularly important for small-amplitude biosignals. Generally, a resolution of 12 to 24 bits is employed in most biosignal applications, depending on specific requirements and signal characteristics. The sampling rate (SR) is another significant factor. In accordance with the Nyquist-Shannon sampling theorem, the sampling rate must be at least double the highest frequency component of the biosignal to prevent aliasing. For ECG and EEG signals with a frequency range of 0.1 Hz to 200 Hz, a 500 Hz or 1000 Hz SR is typically required. The input range of an ADC often corresponds to the voltage supply range. In battery-powered systems, the range can be 0-3.7 V for a unipolar supplied ADC. The minimum definable actual resolution can be calculated as follows:

$$Actual\ Resolution = \frac{Input\ range}{2^N}$$

Where N represents the number of bits. This value must be sufficiently smaller than the amplified signals. For instance, consider a 16-bit ADC with an input range of 0-3.7 V; the actual resolution is calculated to be 56.4 μV. With an amplifier gain of 1,000, the minimum definable signal is 56.4 nV (excluding noise considerations). Upon digitization, the signal undergoes further processing or transmission via a microcontroller unit (MCU). The minimum transmission speed can be ascertained by accounting for factors such as sampling rate, channel quantity, and data structure. For instance, a 24-bit, four-channel measurement at a 1000 Hz sampling rate necessitates a minimum data transmission rate of 12 kBps.

Microcontroller units (MCUs) and wireless communication modules are utilized for processing digitized data. Several companies provide integrated MCUs and wireless communication modules. Various wireless data communication options exist, including Wi-Fi, Bluetooth, Zigbee, and Cellular. Given the requirements of animal wearable devices, Bluetooth emerges as the most suitable method, owing to its low power consumption and adequate data transmission rate. Bluetooth Low Energy, an enhanced version with optimized power efficiency, is ideal for numerous applications.

The aforementioned discussion outlines the general process of selecting electronic components for designing wearable electronic systems intended for biosignal acquisition. The choice of components can vary significantly depending on specific applications and priorities. A comprehensive review of specific projects, including actual chip selections, will be presented in the subsequent section.

3.2 Review of Designs

3.2.1. Rodent EEG Board Version I

For the majority of projects aiming to create miniaturized wireless wearable devices, factors such as chip and antenna size, power consumption, data rate, and other aspects are critical. Bluetooth Low Energy (BLE) has emerged as a suitable option, and it has been widely adopted in our projects. The nRF52 series, a versatile System-on-Chip (SoC) developed by Nordic Semiconductor, is designed for Internet of Things (IoT) devices, wearables, and smart home systems. Equipped with a 32-bit ARM Cortex-M4F processor, 512kB of Flash memory, and 64kB of RAM, the nRF52832 supports multiple wireless protocols, including BLE, ANT, and proprietary 2.4GHz protocols, ensuring seamless communication with various devices. With a maximum data rate of 2 Mbps, it provides adequate data processing and transfer speeds for most projects, while consuming minimal power due to its efficient power management system.

The initial prototype system (**Figure 3. 2** 1st Rodent EEG device prototype), which comprises the ADS1299 and MDBT42Q, consists of stacked boards interconnected by board-to-board connectors. Texas Instruments developed the ADS1299, a high-performance, 8-channel, 24-bit ADC, specifically designed for acquiring and processing EEG and other biopotential signals. Although primarily intended for human EEG recording, we employed it in our first prototype to obtain rodent EEG due to its outstanding performance in various aspects. The microcontroller unit, MDBT42Q, interfaces with the ADS1299 via SPI and transmits the received digitized data to a mobile phone through a BLE service. The system is divided into two separate boards: an analog signal board, which primarily contains the analog signal processing functions, including filters and the ADS1299; and a digital and power board, which houses the power management components and the microcontroller unit. This configuration helps prevent analog signals from being affected by digital signal crosstalk from the MCU.

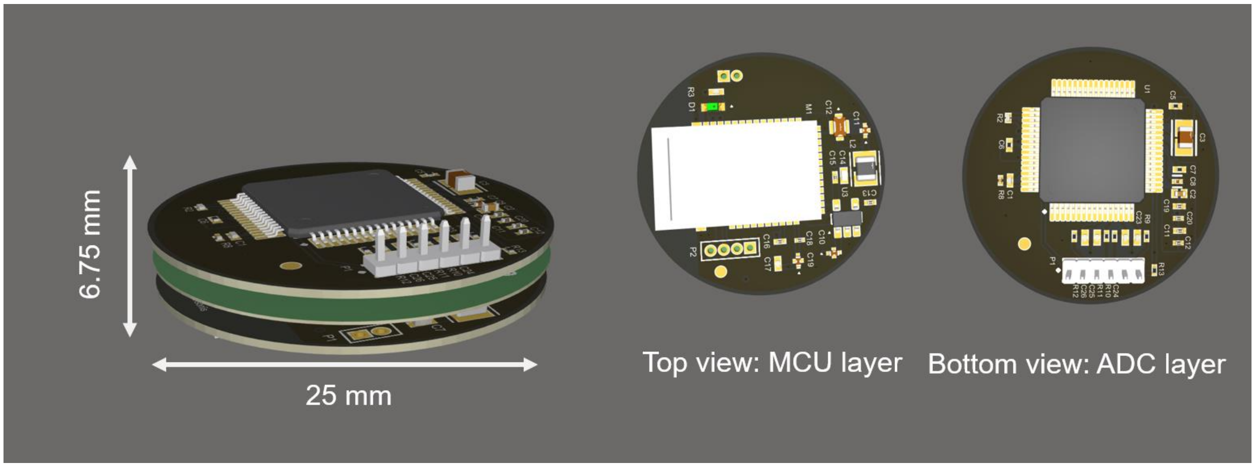

Figure 3. 2 1st Rodent EEG device prototype

Nonetheless, several areas require improvement. First, the system lacks an instrumentation amplifier, leading to signals being directly fed into the ADC after filtering. Although the high-resolution 24-bit ADC, featuring an integrated programmable gain amplifier with a maximum gain of 24, provided some recordings, the absence of an instrumentation amplifier compromised data quality. Second, the ADS1299's power consumption, approximately 39 mW, is excessive for small battery-powered devices, limiting the device's runtime to only a few hours when powered by a 300 mAh battery. Additionally, the prototype lacks a reliable solution for connecting and securing the implanted electrodes. Lastly, the unit's dimensions (25 mm in diameter and 6.75 mm in thickness) exceed the desired specifications, complicating the attachment of the board to a rat. Despite these limitations, this prototype set the general design direction, with numerous common features found in subsequent designs.

3.2.2. Rodent EEG board version II

The most pressing issues that require immediate resolution are those of power consumption and device size. Consequently, we developed a second prototype as shown in **Figure 3. 3**. Instead of employing a power-intensive 24-bit high-precision ADC, we opted for the embedded 12-bit ADC present in the MCU. The nRF52 series features an 8-channel 12-bit ADC with analog inputs. This approach not only decreases power consumption but also eliminates the need for the ADS1299, which measures 10 mm by 10 mm. Given the lower accuracy of the ADC, we introduced instrumentation amplifiers (INAs) to enhance signal quality. INAs with small package sizes and low power consumption were selected, ultimately leading to the choice of the INA2321 after several rounds of comparisons. This dual-channel micropower instrumentation amplifier offers low-cost, low-noise amplification of differential signals while consuming only 40μA of current. Gain was set to 1,000 by pairs of thin-film resistors. The INA2321's size is compatible with that of the MDBT42Q, allowing for placement on both the top and bottom sides of the boards. The final dimensions of the device were 19.2 mm x 16.6 mm, a 34.9% reduction in surface area compared to the previous design. Additionally, the thickness was significantly decreased due to the elimination of a stacked board design.

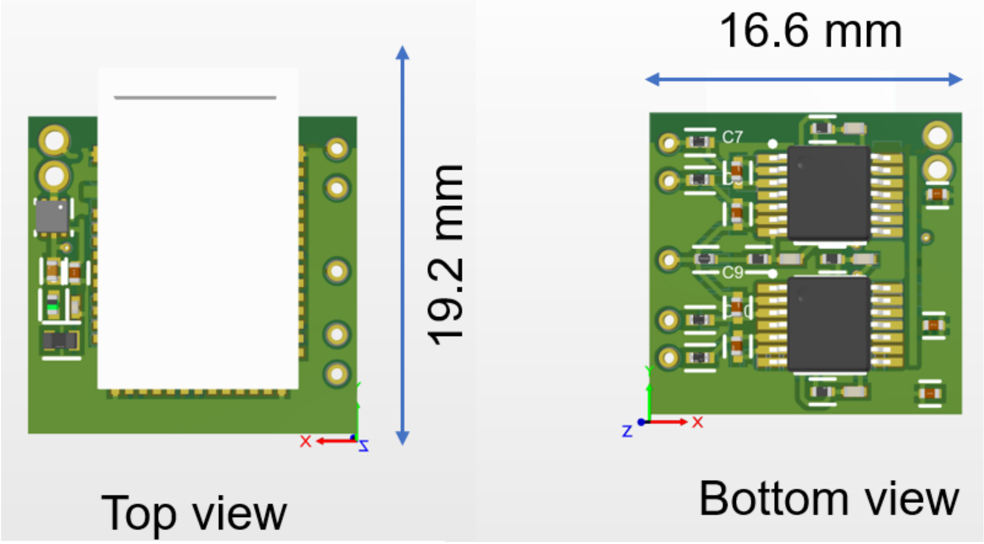

Figure 3. 3. 2nd version rodent EEG board prototype

The dimensions of the board are comparable to the skull size of a medium-sized rat, making it suitable for use as a head-mounted EEG recording device. **Figure 3. 4** presents a comparison between a rat skull model and the actual device. In this design, we also employed standard EEG screws to test the device on anesthetized mice. The screws were connected to through-holes on the board using insulated silver wires. However, the size remains considerably large for application on mice, posing challenges for creating a wearable solution.

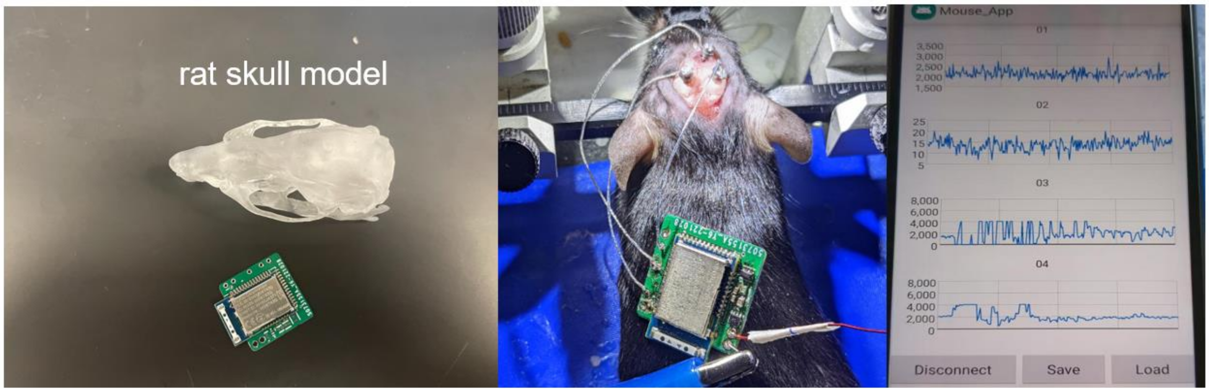

Figure 3. 4. Device testing and demonstration on a mouse

With this device, we successfully obtained data via Bluetooth. A screenshot of the real-time signal acquired from the animal was displayed in the figure. The mouse was administered epilepsy-inducing chemicals, and approximately 20-30 minutes later, we observed the signals, as depicted in channels 3 and 4. These results demonstrate the applicability of the battery-powered device for wireless EEG recording.

To improve the design further, it is necessary to reduce the device size to a 1 cm scale, allowing for installation atop a mouse's skull. However, the current chips are too large. The present design is approaching the smallest feasible limit for a PCB at this scale, given the selected chips. To make significant advancements, innovative designs must be explored, with more advanced and smaller microchips.

3.2.3. Rodent EEG Board Final Version

The final version of the rodent EEG board represents a significant advancement over previous iterations. This prototype, now much more compact, successfully meets the criteria for head-mounted installation. Furthermore, the transition to a “fully wireless” design not only simplifies its usage but also mitigates noise caused by movement at the interfaces, reducing it to an absolute minimum. The culmination of substantial engineering efforts, this improved version stands up to the various challenges encountered during real-world measurement and experimentation.

Presently, most EEG recording devices, whether commercially available or described in academic literature, utilize EEG recording screws to capture signals. These screws are typically connected to the recording apparatus via a flexible metal wire sheathed in an insulating layer. Our previous designs also applied the same methodology (as depicted in Figure 3.4). However, during the installation of these devices, several challenges were observed. Primarily, the electrode placement consumed a significant portion of the available headspace, thereby limiting the area for secure device installation. In addition, establishing an effective electrical connection by wiring the electrode to the device proved labor-intensive and cumbersome. Finally, the pathway for unfiltered and unamplified signals through the wire was susceptible to extraneous noise interference due to its length. Notably, the flexibility of these wires also proved to be a liability as their movement generated additional noise.

The common solution that many engineers and researchers have relied on is to include a socket or a guide cannula, to streamline the collection and arrangement of wires and enhance connection reliability. However, this approach is not without its shortcomings. The additional occupation of sockets leads to a constricted workspace. Moreover, the intricate task of installing the wires correctly into the sockets can be labor-intensive and challenging, given the delicate nature of these wires. This cumbersome and user-unfriendly interface may lead to eventual failure. Lastly, these wires can often be a source of electrical and motion noise, further complicating the process.

These challenges observed during experimentation prompted the inception of an innovative concept. The Figure 3. 5 elucidates the implementation of this concept. Ultimately, a fully wireless device was designed, with integrated electrodes that allow for unified installation. This advancement eliminates the need for manual wire connections, greatly simplifying the installation process while providing a more user-friendly interface.

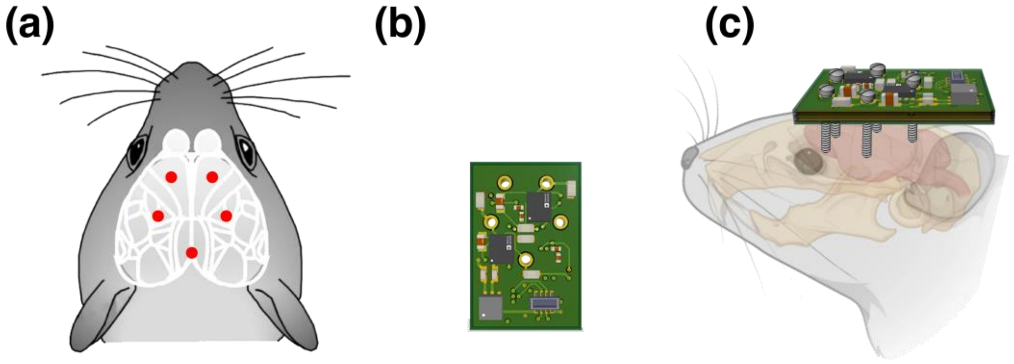

Figure 3. 5 Flow diagram of the design and implementation of the device

The development of this innovative solution involves three main stages. Firstly, we align the design with the research objectives by acquiring a detailed brain map that corresponds to the brain sections under exploration. This ensures that our system targets the precise areas of interest. Next, we leverage the brain map to tailor the circuit layout to coincide with the positions of the electrodes. As an illustration, the red dots shown in Figure (a) signify the electrode positions designated for acquiring signals from the visual cortex. The layout illustrated in Figure (b), complete with five through-holes, aligns accurately with these positions. Subsequently, screws are installed through these holes on the board and skull. In addition to serving as EEG recording electrodes, these screws also provide crucial anchorage for the secure fixation of the device.

The existing challenge lies in the compactness of the device; it must be small enough to fulfill the design specifications. Given the petite size of the brain and the narrow distances separating each electrode, space is critically limited. The initially chosen INA and ADC cannot be accommodated within the board. Fortunately, Analog Devices recently launched several chips that are significantly smaller than conventional devices, rendering our design feasible. The INA, AD8233, and ADC, AD4130-8 were chosen for this design. Both are equipped with a Wafer Level Chip Scale Package (WLCSP). The AD8233 measures a minuscule 2mm × 1.7 mm, and the AD4130-8 is 2.74 mm × 3.6 mm. As a bonus add-on, both devices feature ultra-low power consumption, making them an optimal choice for our project.

To achieve the objectives of size reduction and prevent crosstalk between digital and analog signals, a stacked board design was implemented. This approach involved two distinct boards that were connected using a small board-to-board connector, BM-29. The bottom board served as the signal board, comprising the through holes aligned with the electrode positions, along with four INAs and an ADC. These components facilitated the acquisition and processing of analog signals. The top board primarily housed the BLE module, MDBT42V, which enabled wireless connectivity. Through this stacked board configuration, the overall size of the device was significantly reduced as shown in Figure 3. 6. The bottom signal board measured a mere 8 × 12 mm, while the BLE board encompassed approximately 10 mm × 9 mm, inclusive of the chips. This compact arrangement ensured the efficient integration of the necessary components, while effectively addressing potential signal interference between the digital and analog domains.

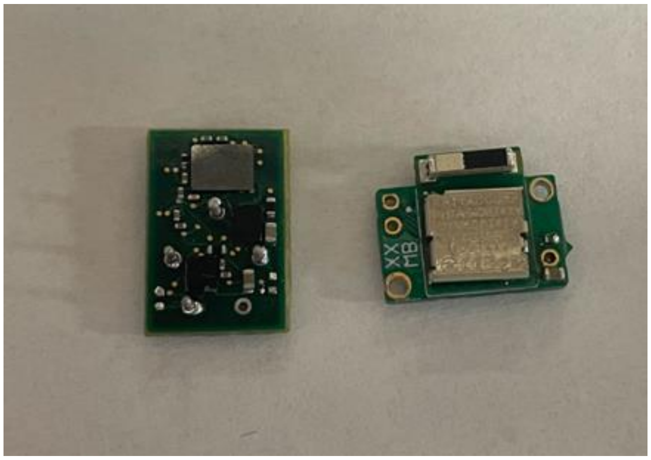

Figure 3. 6. Photo of the top and bottom boards

The choice of battery was meticulously made to ensure seamless integration with the remaining components of the design. After numerous iterations and exploration of potential alternatives, the optimal choice emerged as Tabbed Lithium Coin Cells, with an output of 125 mW. The implementation of this power source necessitated the modification of the system's center of mass, thus ensuring its alignment with the central region of the predetermined brain map positions. The total weight of the whole device is 3.787 g, which is light enough for mice to carry. A photographic representation of the entire device was obtained after combining all the components, as presented in Figure 3. 7.

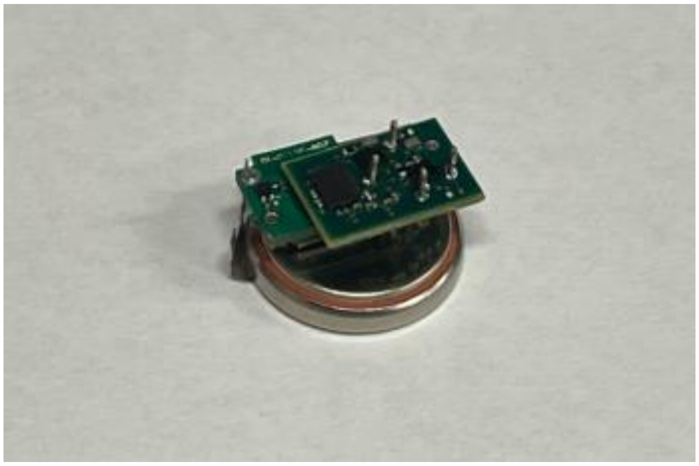

Figure 3. 7. Photograph of the entire device after combining

To guarantee the robustness of the signal and the overall integrity of the device, a custom housing was fabricated using 3D printing, utilizing a resin material for optimal durability and protection. Concurrently, the underside of the device was safeguarded with a meticulously applied layer of Parafilm, providing an additional layer of protection and stability, and avoiding direct touching of the electronics and the animal. Figure 3. 8 depicts the whole device after implementing the housing designs.

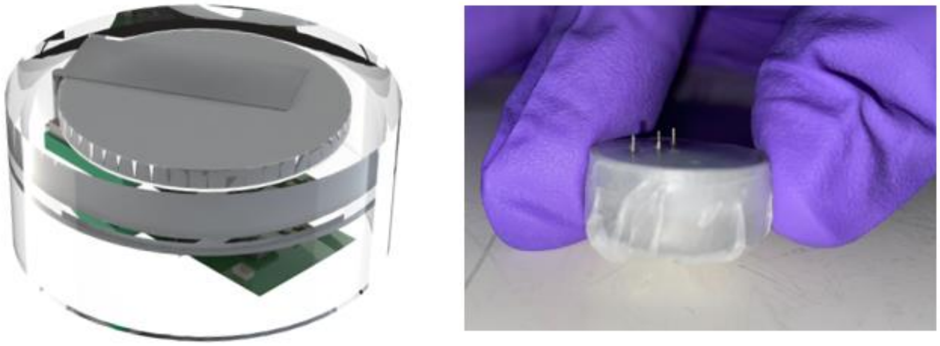

Figure 3. 8. The device housing design.

CHAPTER 4 – Flexible pH Sensors

4.1 Overview

Electrophysiology is frequently associated with environmental changes and external stimuli. To monitor these influences on the animal models, numerous sensors have been employed to detect and quantify the alterations. These sensors may encompass temperature, humidity, light, and chemical sensors, among others, to capture a comprehensive view of the environment. By integrating such sensors with electrophysiology recording systems, researchers can gain a better understanding of the relationship between environmental factors and the functioning of the nervous and cardiovascular systems. This knowledge can ultimately help in the development of targeted interventions or treatments to mitigate the adverse effects of environmental stressors on health and well-being.

In aquatic systems, pH is a critical parameter. However, developing an accurate wearable pH sensor for small aquatic animals remains a challenge. In laboratory settings, pH meters serve as the standard tool for determining the pH of aqueous solutions by measuring the potential difference between a reference electrode and a sensing electrode. Traditional benchtop pH meters employ pencil-like, glass-type combination electrodes with ion-selective membranes, known for providing stable and precise pH measurements. Nonetheless, these sensors exhibit limitations that impede their applications in various scenarios. For example, the inherent brittleness and complexity of the electrode structure create challenges for miniaturization. To facilitate environmental monitoring on small animals, the development of flexible and compact wearable pH sensors is becoming increasingly desirable.

Among the alternatives for more flexible and smaller-sized pH sensing methods, solid-state metal oxide-based pH sensors have been widely discussed. Specifically, iridium oxide (IrOx) electrodes have stood out for their good stability, faster response time, long lifetime and wider working ranges compared to other metal oxide electrodes [26, 27]. Various IrOx electrodes fabrication methods have been proposed, leading to two primary types of products: anhydrous electrodes and hydrous electrodes, with notable differences in performance [28-36]. Anhydrous electrodes possess about 59 mV/pH sensitivity and are known for their relative better stability and reproducibility. Fabrication of this type of electrodes typically involves thermal treatment at high temperature for several hours to eliminate hydrous compositions from IrOx. Hydrous electrodes, on the other hand, have a sensitivity range of 60 to 90 mV/pH. The fabrication methods include anodic electrochemical growth of IrOx film on iridium wire or electrodeposition of IrOx film on noble metal electrodes. The formed films were generally named as anodic iridium oxide films (AIROF) and the latter as electrodeposited iridium oxide films (EIROF), referring to the different preparation methods. EIROFs, in particular, have attracted growing interest in recent years due to their lower cost, reproducibility, rapid fabrication process, and potential for on-chip integration [37-39]. The deposition process can be done at room temperature by immersing noble metal electrodes into an iridium complex-containing solution and applying cyclic voltages. This simple and cost-effective method of fabrication makes EIROFs well-suited for integration into various designs of microelectrode arrays and other microfabrication technologies and are particularly promising in miniaturization of wearable and biocompatible devices.

Our research primarily focuses on electrodeposited iridium oxide pH sensors. In this chapter, we will review the development of flexible pH sensors, identify the significant underlying issue associated with this type of pH sensor, and propose an efficient solution to address the problem. Subsequently, we will discuss how these advancements can contribute to the development of wearable pH sensors for animals and explore the potential future directions of this research.

4.2 Initial Explorations and Underlying Problems

This research builds upon the ongoing work of the group. In 2011, Huang et al. introduced a flexible pH sensor based on a polymeric substrate, fabricated using a low-cost sol-gel process for iridium oxide (IrOx) sensing film [40]. Since 2017, the group has published several research articles focusing on flexible pH sensors using electrodeposited iridium films [41, 42]. Some intensive research has been conducted to investigate the performance, understand the mechanism and explore the possible applications of the electrodeposited IrOx film. Overall, these methods offer a potential alternative for integrating pH-sensitive films into other sensors and wearable devices, which can establish a comprehensive monitoring system for aquatic animals.

However, during the course of exploration, an underlying issue has been identified that significantly hinders the direct application of these sensors in wearable sensing systems. Previous studies have demonstrated that EIROF-based pH sensors exhibit suboptimal performance compared to those fabricated using other techniques [43-45]. To maximize the benefits of EIROF in practical applications, it is essential to address known stability issues such as hysteresis, potential drift in long-term recordings, and non-linearity. Moreover, due to the variability of multiple components in the hydrous deposition environment, the performance of the produced films may be inconsistent, even when using precisely controlled electrochemical deposition procedures. In such cases, calibration becomes a crucial step for each sensor after fabrication. Furthermore, sensor performance may degrade over time, resulting in decreasing sensitivities or drifting, and consequently necessitating frequent recalibrations after use. Therefore, there is a pressing need for post-production improvement of these sensors.

Figure 4. 1 presents an example of open-circuit potential (OCP) measurement during a typical calibration process. The fabricated IrOx pH sensors were immersed in pH 4, 7, and 10 buffers and allowed to stabilize for 180 seconds. During the immersion, the OCP was measured against an Ag/AgCl reference electrode. As shown in the figure, the measurement in the pH 4 buffer was unsatisfactory, as it displayed a noticeable downward drift in the OCP.

The zoomed-in view provides a more detailed perspective on the OCP measurements, highlighting the downward drift in the pH 4 buffer, as shown in **Figure 4. 2**. This close-up observation emphasizes the need for addressing the sensor's stability issues to improve its performance.

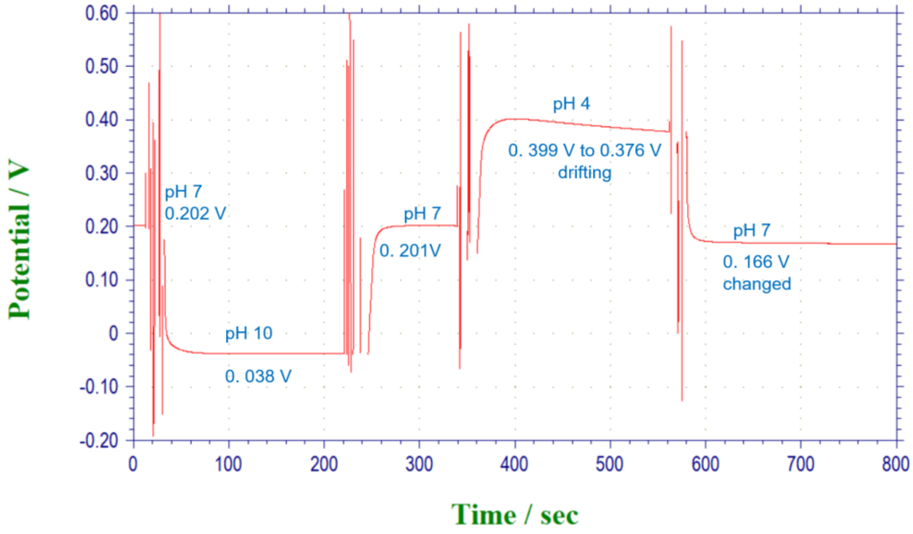

Figure 4. 1 An example of OCP measurement in different pH buffers

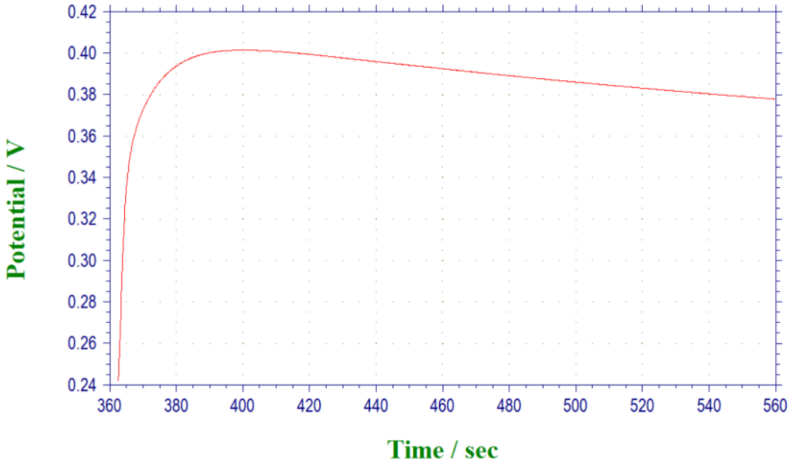

Figure 4. 2. The zoomed-in view of OCP drift

4.3 Performance enhancements

Researchers have been exploring methods to modify pH sensing performance of the EIROF sensor post-deployment. Carroll et al. showed that, with a proper constant voltage treatment, it is possible to standardize individual electrodes in an electrode array to have similar absolute potential outputs and identical calibration curve slopes [46]. Steegstra et al. correlated pH sensitivity of hydrous iridium and its oxidation states [47]. Their findings revealed a relationship between pH sensitivity and different constant voltages used in the treatment of EIROFs. Olthuis et al. pointed out that the drifting potentials changed differently in different oxidation states [48]. These studies suggested that the surface oxidation states EIROF pH sensors can potentially be modified and controlled by applying external voltages, which in return can improve sensor performance to greater degrees.

We attempted to replicate previous experiments reported in the literature. These studies claimed that the use of constant voltage treatment (CVT) could potentially alter the surface oxidation state and standardize individual electrodes. We tested various treatment voltages, and the results are presented below. The calibration curves were plotted for different groups subjected to distinct treatment conditions. Notably, varying treatment voltages resulted in upward and downward shifts of the calibration curves. The experiment confirmed the correlation between the oxidation state changes and the applied CVT, and represented by the shifts of the calibration curves.

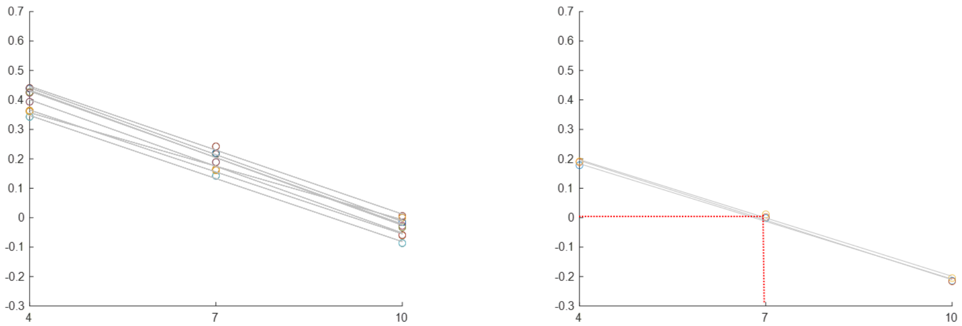

Untreated

0 V CVT

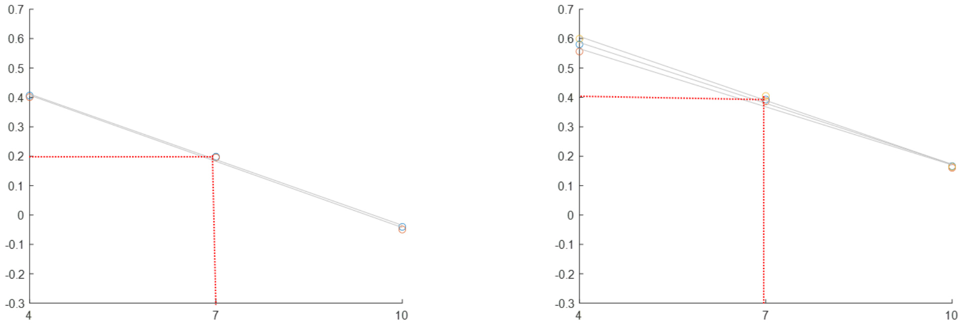

0.2 V CVT

0.4 V CVT

Figure 4. 3. Calibration curves of pH sensors under different voltage treatment

During the tests, a more intriguing observation emerged: the drift could be mitigated by the treatment. Based on this observation, a more rigorous investigation was conducted, and the review of the study will be presented in the following sections

4.3.1. Materials and Methods

The substrate electrodes were fabricated using the following procedure. Silicon wafers with a 500-nm thick thermally-grown silicon dioxide layer were chosen as the substrate for the electrodes employed in stability studies. The electrode fabrication process involved standard lift-off lithography techniques. NR9-1500PY photoresist (Futurrex Inc., NJ, USA) was applied and patterned onto the wafers. Subsequently, layers of Au/Cr with thicknesses of 200 and 20 nm were deposited on the wafers via electron-beam evaporation. The substrate with patterned electrodes was then formed through sonication of the wafers in an organic solvent. To provide a barrier layer on the traces, a 1-μm layer of Parylene-C was deposited using an SCS PDS 2010 Labcoter Parylene Coating System (SCS Equipment, IN, USA), while the sensing areas remained exposed at dimensions of 1 mm × 1 mm. Finally, the wafers were diced into individual probes. **Figure 4. 4** illustrates the fabrication procedures for the two types of substrate electrodes.

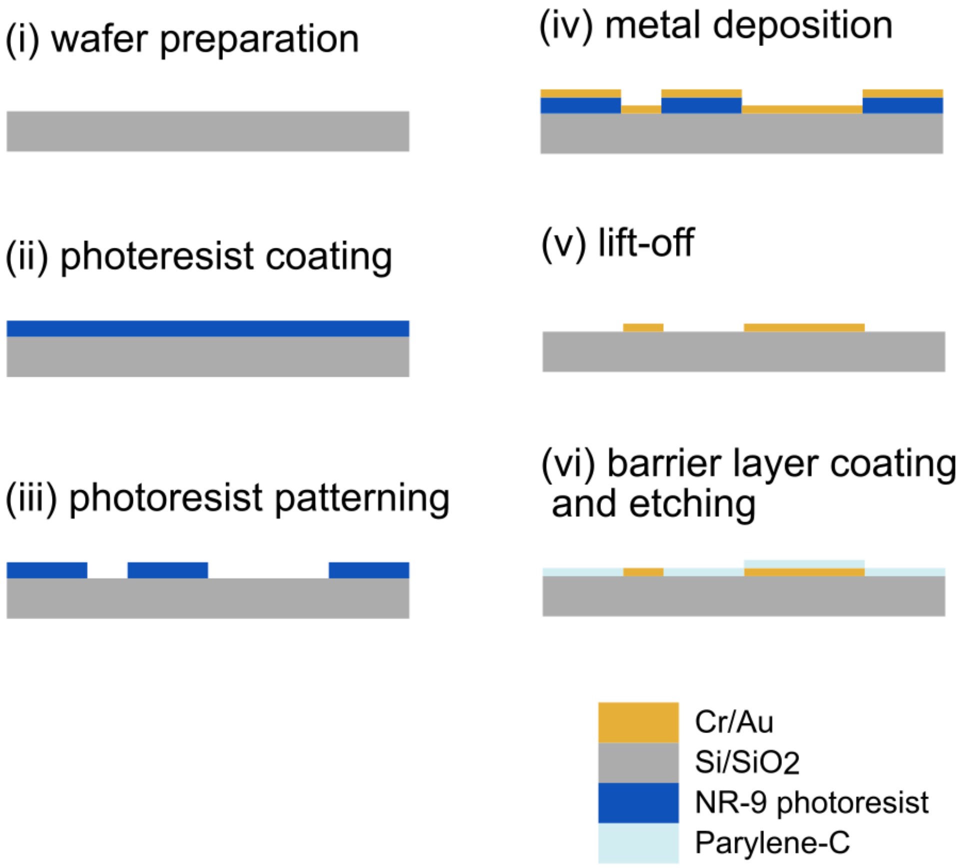

Figure 4. 4. Fabrication process of the substrate electrode

Iridium-oxalate solution was prepared following the recipe described by Yamanaka [49]. In brief, 70 mg of iridium tetrachloride was dissolved in 50 mL of deionized (DI) water, and the solution was stirred for 30 minutes. Then, 0.5 mL of 30% H_2O_2 was added and stirred for additional 10 minutes. Next, 250 mg of oxalic acid dihydrate was added and the solution was stirred for another 10 minutes. The pH was adjusted to 10.5 by the addition of potassium carbonate while stirring. The solution was left at room temperature for 3–4 days and then stored in a refrigerator at 4°C before use.

The electrodeposition process was performed using cyclic voltammetry (CV) with an Electrochemical Workstation (CHI-760E, CH Instruments, TX, USA). The CVs were conducted in a three-electrode configuration, where a Ag/AgCl glass type electrode filled with 1-M NaCl was used as the reference electrode (RE) and a Pt wire served as the counter electrode (CE). The gold electrodes fabricated on Si substrates and Kapton substrates were used as the working electrodes (WEs). The WE potential was sweeping between −0.5 V to +0.65 V against RE at a scan rate of 1 V/s for 600 cycles. The examples voltammograms of CV obtained during the electrodeposition of three sensors were shown in **Figure 4. 5**. After deposition, the electrodes were immersed in DI water for storage until use. **Figure 4. 6** provides a collection of microscopic photographs capturing the electrodes before and after the electrodeposition of iridium oxide.

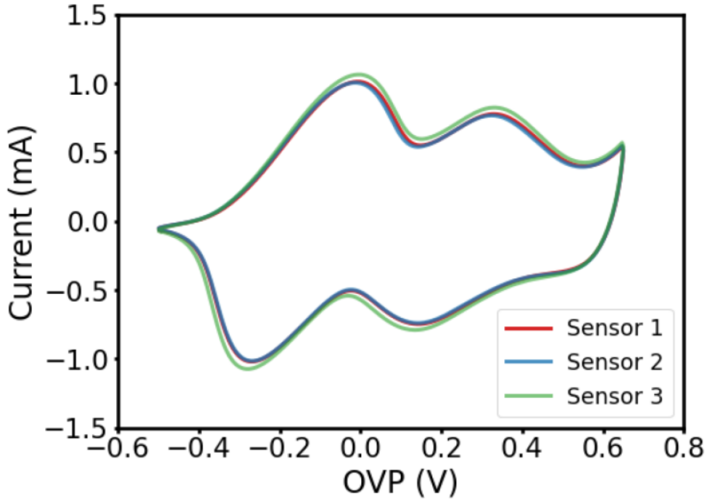

Figure 4. 5. The final cycles voltammogram of 3 electrodepositions

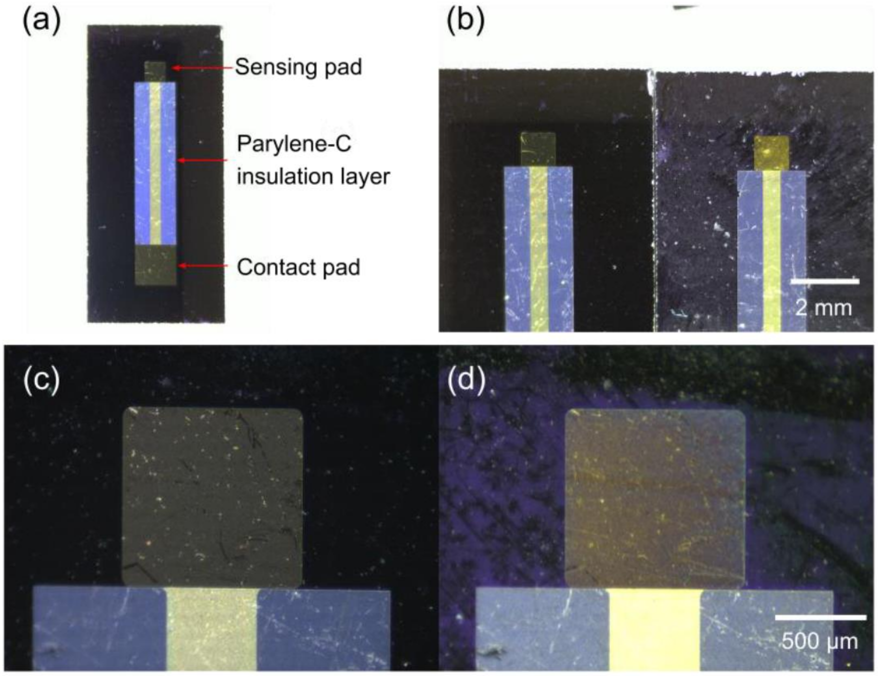

Figure 4. 6. Microscopic photographs of the electrodes before and after electrodepositions.

4.3.2. pH Sensing Window

Following the fabrication of electrodeposited IrOx pH sensors, testing and calibration procedures were conducted. During this process, a phenomenon referred to as the pH sensing window was observed. A careful investigation was performed to validate the findings.

Following electrodeposition, the IrOx-coated electrodes were rinsed with DI water and subsequently stored in either DI water or phosphate-buffered saline (PBS) when not in active use. Upon submersion in either solution, the OCP between the electrode and the RE gradually reached a steady state. Despite precise control of the fabrication process by the potentiostat, the stabilized voltages in the same solution and the sensitivity varied among electrodes. For most freshly fabricated electrodes, the OCP stabilized within the range of 0–0.2 V in 10X PBS, with respect to an Ag-AgCl RE. Afterwards, the sensors were tested in different pH solutions. Significant OCP drifts were observed for some sensors in specific solutions, particularly in strong acids or bases. These drifts could be either rapid in a short period of time or slow but persisting for a longer period of time. Accurate and reliable OCP readings were difficult to obtain in the presence of such drifts. Furthermore, it was discerned that, although the sensor OCP may have remained stable in an acidic solution, significant drifts tended to occur when the sensor was subsequently placed in a basic solution, and vice versa. Based on these observations, we speculated that the EIROF-based pH sensors may have specific pH ranges within which stable OCPs can be acquired with minimal drift, denoted as the pH “sensing window”. When the pH of the solution deviates from this preferred sensing range, the drift effect becomes more pronounced.

To investigate the hypothesis, OCP of sensors in different solutions were monitored following electrodeposition. Figure 4. 7. (a) depicts the OCP changes of 5 sensors that were sequentially immersed in PBS, acidic and basic solutions. The acidic solution was prepared with 1-mM HCl and measured to have a pH of 3.08 by a commercial pH meter. The basic solution was made of 1-mM NaOH, with a measured pH of 11.12. Each measurement segment lasted for 5 minutes. Figure 4. 7. (b) illustrates the correlation between the pH and the OCP of the sensors, showing a varied range of absolute potentials and sensitivities. Overall, the fabricated sensors demonstrated good linearity within the pH range of 3–11. However, the considerable drift rendered the sensors unreliable for long-term or repetitive pH measurements. Upon closer inspection, a moderate correlation between the absolute potential and the drift of the sensors can be observed. The OCP changes during the last 200 seconds of each measurement segment were extracted and quantified as the drift in this experiment. The drift rates, calculated by dividing the drift by measurement time, were compared in Figure 4. 7. (c). The average OCP values measured in PBS, HCl, and NaOH solutions for each sensor were correlated with their respective drift rates. Although the freshly fabricated sensors exhibit similar performance, their drifts in different solutions were observed to differ and exhibit a discernible trend. Notably, the sensors had a more pronounced drift in the NaOH solution. Higher average OCPs tended to be associated with slower drift rates in the NaOH solution, suggesting the sensors' sensing windows were located closer to basic pH ranges.

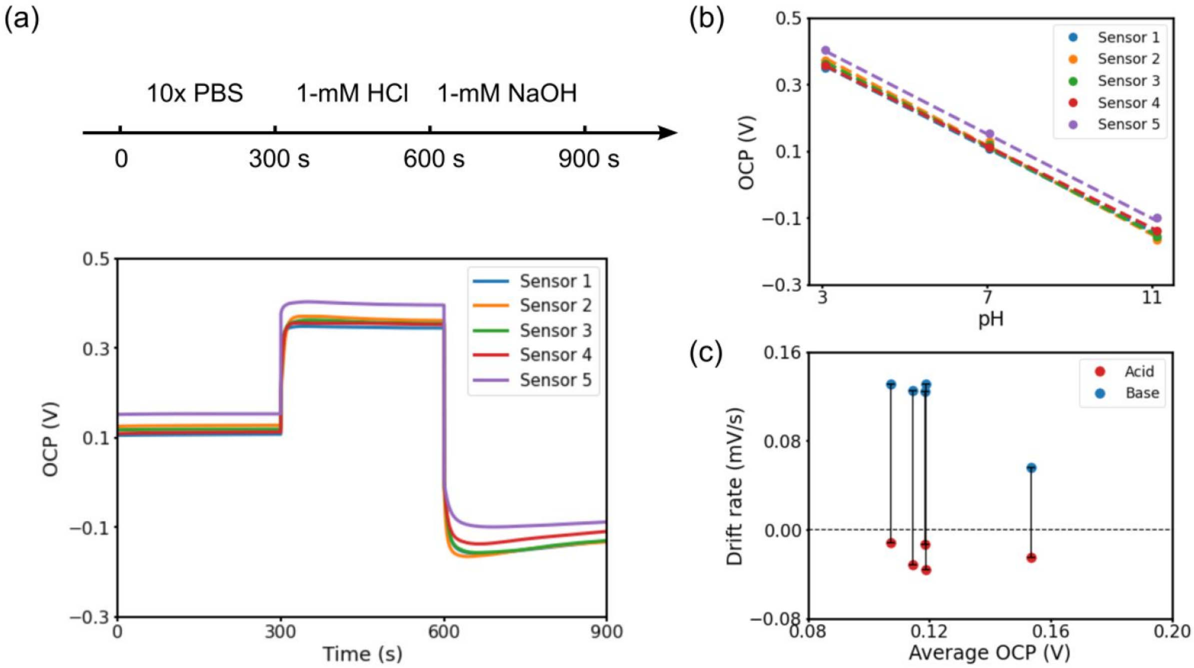

Figure 4. 7. Stability tests conducted on five freshly fabricated pH sensors.

4.3.3. Constant Voltage Treatment

Following the above analysis, we have considered whether altering the absolute potential of sensors would result in a corresponding controlled manipulation and stabilization of their sensing window. Previous studies have reported that by imposing a constant voltage between the sensors and the RE in specific solutions such as 0.1-M KOH solution and pH 7 buffer, calibration curves of the sensors could be adjusted, including both the intercept (i.e., the absolute potential) and the slope (i.e., the sensitivity).

A set of experiments were conducted to examine the effect of constant voltage treatment on the sensor drift. The sensor was sequentially tested in PBS, 1-mM HCl solution, and 1-mM NaOH solution for a duration of 5 minutes each. The original stabilized OCP of the sensor in 10X PBS was measured to be 0.107 V. Subsequently, the sensor was biased at 0.2 V, 0.3 V, 0.4 V and 0 V respectively for 2 minutes in 10X PBS and went through the same testing routine as described in previous paragraph. The results are presented in **Figure 4. 8**. After the constant voltage treatment, the sensor's OCP could be maintained at the applied biasing voltages, without compromising its ability to respond to pH changes. As the drift was more significant in the NaOH solution, when the sensing window of the sensor was manipulated to basic pH ranges, the overall stability can be enhanced. This is reflected in the superior linearity of the calibration curves of the 0.3 V or 0.4 V treated sensor, as depicted in **Figure 4. 8. (b)**.

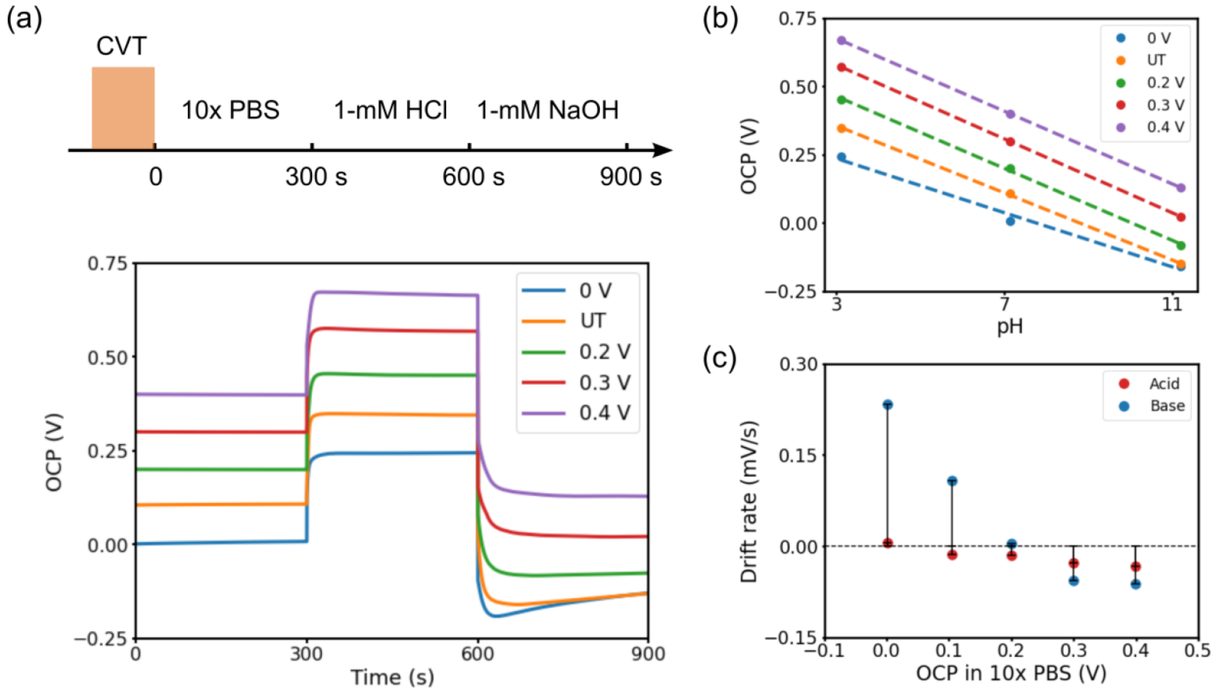

Figure 4. 8. The effects of constant voltage treatment on the performance of an IrOx pH sensor.

Additionally, a proportional modulation of the sensor's drift was observed in response to alterations in its absolute potential. The drift rates were calculated and presented in **Figure 4. 8. (c)** with respect to the initial OCPs in 10X PBS of the sensor under different treatment conditions. The observed trend showed clear correlations, validating the proposed hypothesis that the sensing window of the sensor could be adjusted by manipulating its absolute potential through constant voltage treatment. These findings demonstrate the potential utility of this method to improve the stability and reliability of the EIROF sensors for long-term and multiple pH measurements.

Additionally, a proportional modulation of the sensor's drift was observed in response to alterations in its absolute potential. The drift rates were calculated and presented in **Figure 4. 8. (c)** with respect to the initial OCPs in 10X PBS of the sensor under different treatment conditions. The observed trend showed clear correlations, validating the proposed hypothesis that the sensing window of the sensor could be adjusted by manipulating its absolute potential through constant voltage treatment. These findings demonstrate the potential utility of this method to improve the stability and reliability of the EIROF sensors for long-term and multiple pH measurements.

4.3.4. Stability Improvement

More sensors were examined to assess the stability improvement with the constant voltage treatment. A total of six sensors were evenly divided into two groups, one subjected to an acidic environment (the acid group) and the other to a basic environment (the base group). Prior to the experiment, the sensors were stabilized in 10X PBS, followed by a recording of the OCP for a duration of three minutes. Subsequently, the sensors were moved into a 0.01-M NaOH or HCl solution for 5-minutes recordings. The results are presented in **Figure 4. 9. (a) and (c)**. Afterwards, the sensors were returned to the 10X PBS for treatment. Based on previous results, a biasing voltage of 0.3 V was applied to the base group, while 0 V was selected for the acid group. The constant biasing voltages were sustained for two minutes. Following the treatment, the sensors were returned to 10X PBS and the OCPs were recorded for three minutes, after which they were moved to the same HCl/NaOH solutions for another 5-minutes recordings. The results are illustrated in **Figure 4. 9. (b) and (d)** for comparison with the pre-treatment results. In general, the results indicated that the constant voltage treatment had a positive impact on the performance of the sensors. Specifically, the sensors demonstrated more consistent recordings, and reduced drifting to a certain extent.

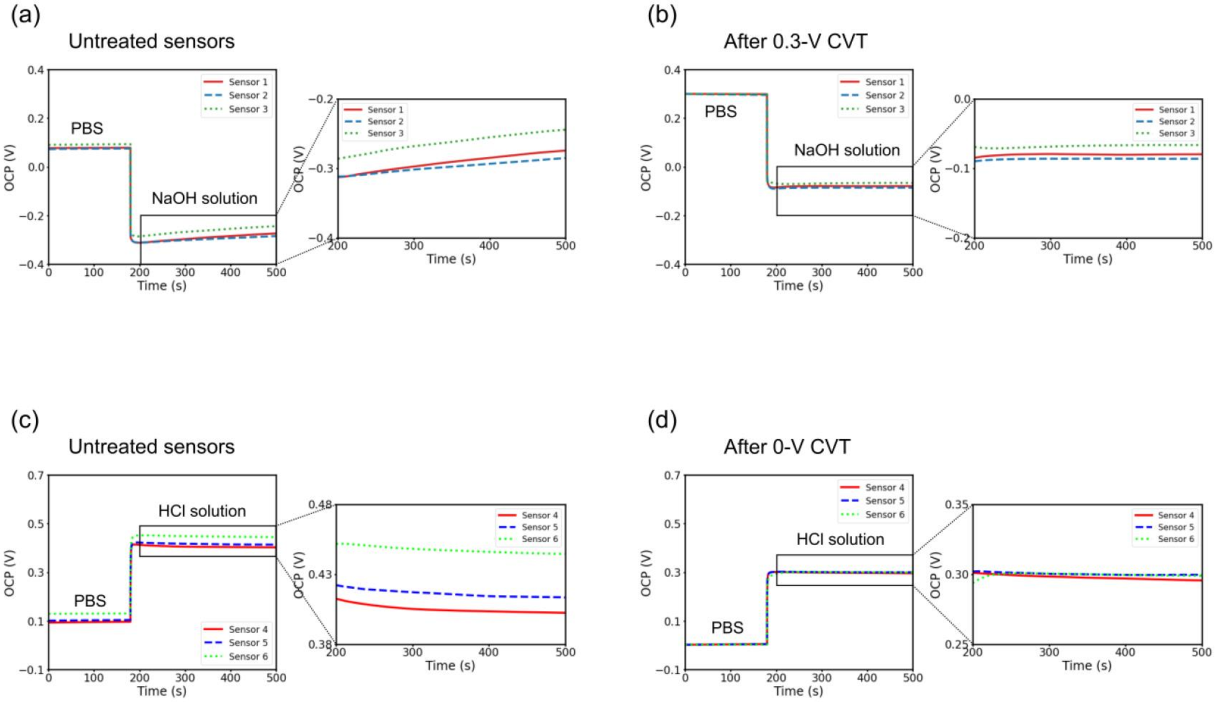

Figure 4. 9. Stability improvement after constant voltage treatment.

To quantitatively evaluate the stability and repeatability of the sensors, three factors, namely potential fluctuation, potential deviation, and potential drift were defined in **Figure 4. 10. (a)**, following a similar approach as outlined by Huang *et al.* [40]. The OCP typically exhibits an overshoot within a short time upon the sensor's entry into the solution due to high-density charges exchange, then it settles to a relatively stable level after equilibrium starts. The potential drift is defined as the difference between the potential at the final recording time point and the turning point, with a positive or negative sign indicating the direction of the drifting. After the turning point, it usually takes around 10 seconds to reach the relatively stable level after the turning point. The duration of 100–300 seconds was selected to evaluate the potential fluctuation during the established relatively stable states. The potential deviation represents the disparity in OCPs measured by different sensors in the same solution.

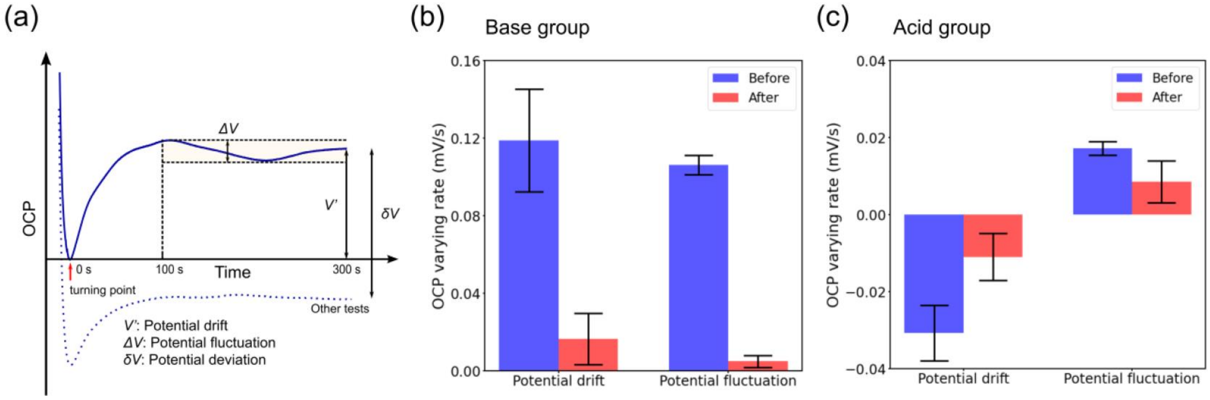

Figure 4. 10. Quantitative comparison of the stability before and after CVT.

		Before treatment			**After treatment**		
Base group	Sensor #	Drift (mV)	Fluctuation (mV)	Deviation (mV)	Drift (mV)	Fluctuation (mV)	Deviation (mV)
	1	38.2	23	40.3	6	1.1	19.8
	2	26.7	16.7		4	0.3	
	3	42	24		4.8	1.5	
	Average	35.6	21.2		4.9	1.0	
	Improvement (%)				86.1	95.4	50.9
Acid group	Sensor #	Drift (mV)	Fluctuation (mV)	Deviation (mV)	Drift (mV)	Fluctuation (mV)	Deviation (mV)
	4	-11.5	3.1	42	-5.4	2.9	4.1
	5	-9	3.8		-2.4	0.8	
	6	-7.2	3.4		-2.1	1.4	
	Average	-9.2	3.4		-3.3	1.7	
	Improvement (%)				64.3	50.5	90.2

Table 4. 1. Stability factor comparison before and after constant voltage treatments

Table 1 shows the parameters of the 6 sensors in respective acid or basic solutions before and after treatment. The statistics are shown in **Figure 4. 10 (b) and (c)**. Overall, newly fabricated sensors had the worse stability in a basic solution. The average potential drift was 35.6 mV during a 5-minute measurement. After the constant voltage treatment at 0.3 V, the average drift was improved by 86.0%, to 4.9 mV. The fluctuation was improved by 95.7%, from 21.2 mV to less than 1 mV. The stability was greatly enhanced. A smaller range of potential fluctuation indicated not only improved stability but also a shorter response time. In the acid solution, newly fabricated sensors showed relatively better stability compared to those in basic solution, and the treatment still improved the sensor stability. Potential drift was improved by 65.7% and the fluctuation was improved by 48.1%. The potential deviations were improved from 40.3 mV to 19.8 mV in basic solutions, and from 42 mV to 4.1 mV in acid solutions, indicating a better consistency and repeatability among sensors after treatment.

To further investigate the drift issues, measurement periods were extended from 5 minutes to 2 hours. After electrodeposition, the electrodes were immersed in 10X PBS until stabilization. Then, they were transferred to 0.01-M NaOH solutions and immersed for 2 hours while the OCP was continuously recorded against a Ag/AgCl glass type RE. Next, they were moved to 10X PBS, and a constant voltage of 0.3 V was applied across the electrodes for 2 minutes. After the biasing was removed, the electrodes stayed in the 10X PBS for another 3 minutes for stabilization before they were placed back in the same 0.01-M NaOH solution for another 2 hours. This test was repeated for three different working electrodes, and the results are shown in **Figure 4. 11. (a)**. The same experimental procedure was conducted for the other three working electrodes, except the NaOH solution was replaced by 0.01-M HCl solution, and the bias voltage was 0 V. The results are shown in **Figure 4. 11. (b)** for the acid group.

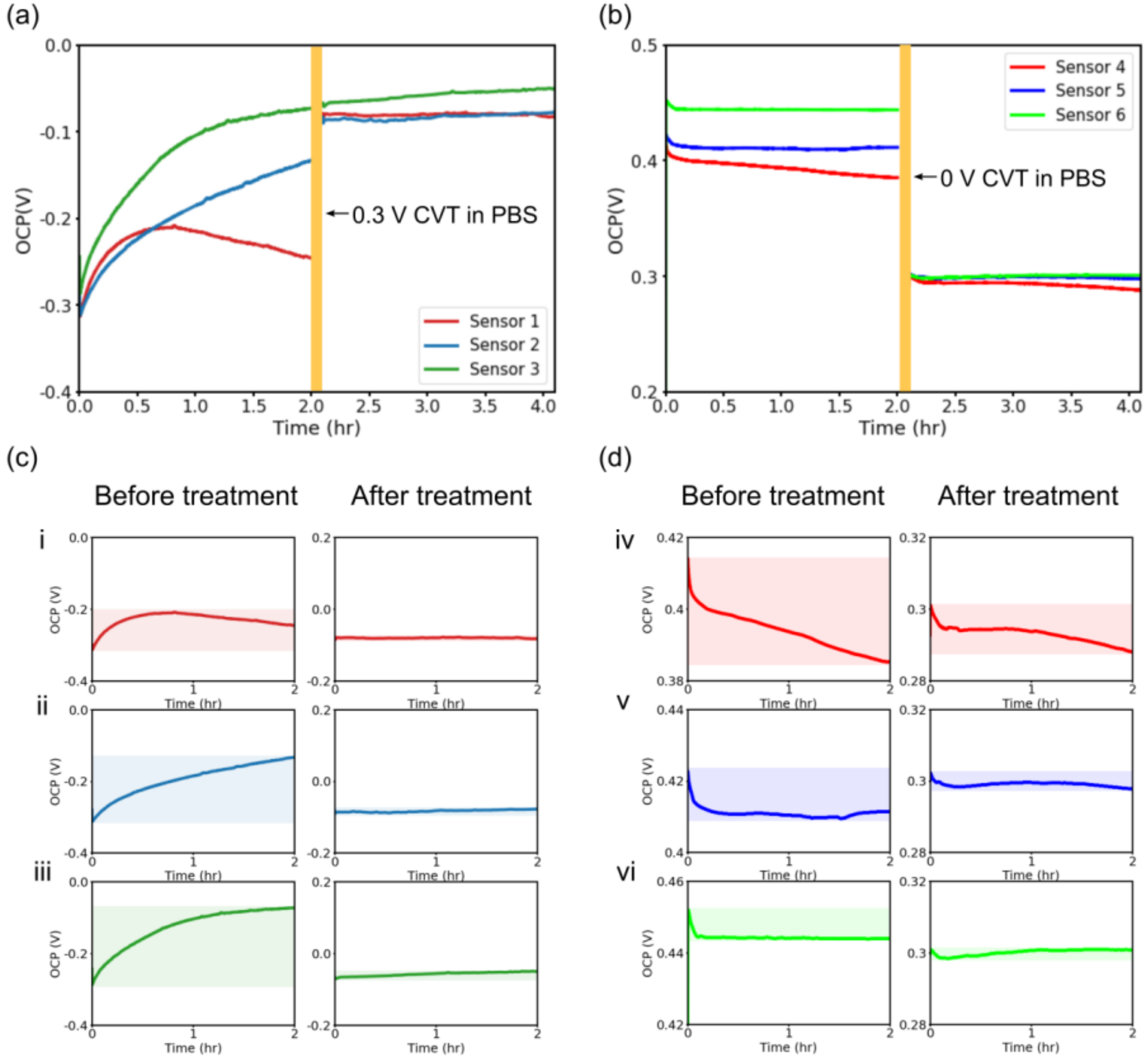

Figure 4. 11. 2-hour pre- and post- treatment stability investigations.

The constant voltage treatment periods are represented by the solid orange bars in the figures. Comparing pre-treatment and post-treatment, the three electrodes in the basic solution against the same glass Ag/AgCl reference electrode show significant drifts. Particularly, one of the working electrodes (the green curve) had non-monotonic OCP before treatment but became monotonic with little drift after treatment. Meanwhile, the variation range of OCPs became narrower after treatment. A similar trend was observed in the acid group, wherein the three working electrodes display reduced drifts in acid solution after treatment. **Figure 4. 11. (c) and (d)** show details of the six electrodes before and after treatment in basic and acid solutions, respectively. The average improvement of drift in the three samples was 91.9% for the base group, and 63.4% for the acid group. The initial potential drifts were higher in the base group, compared to counterparts in acid, which led to more impressive improvement after treatment.

4.3.4. Titration

Universal buffers were titrated from a pH range of 2–12, while a benchtop pH/mV meter and a freshly fabricated IrOx pH sensor were used to monitor the pH changes. The buffer solutions were stirred and kept recording for 60 seconds during each addition of 1-M NaOH solution. The potentials recorded by the pH meter and the OCP of the pH sensor are displayed in **Figure 4. 12. (a)**. The OCP of the pH meter and the pH sensors at the 50th second of each duration were extracted and plotted in **Figure 4. 12. (b)**. The pH meter was calibrated with standard pH buffers (pH = 4, 7, and 10). The pH values read by the pH meter were collected as reference pH in the figures. As observed, compared to the pH meter, the IrOx pH sensor had a faster response rate in general. A general comparison of response rate was shown in **Figure 4. 13**. The pH sensor also displayed excellent linearity with −74.9 mV/pH sensitivity. However, drifts were observed in high and low pH ranges. The drifts of the pH meter and the pH sensor at each pH level were calculated and plotted in **Figure 4. 12. (b)**. The drifted potentials of the pH meter were generally lower than 2 mV with random directions during the titration. In contrast, the IrOx pH sensor drifted in a manner with a clear trend. The results indicate that this sensor has a sensing window centered in the weak basic region, where the pH value was around 9. From low pH to the center, the drifted potential decreased, but then the drift direction inverted when it crossed the region and became higher and higher as the titration continued.

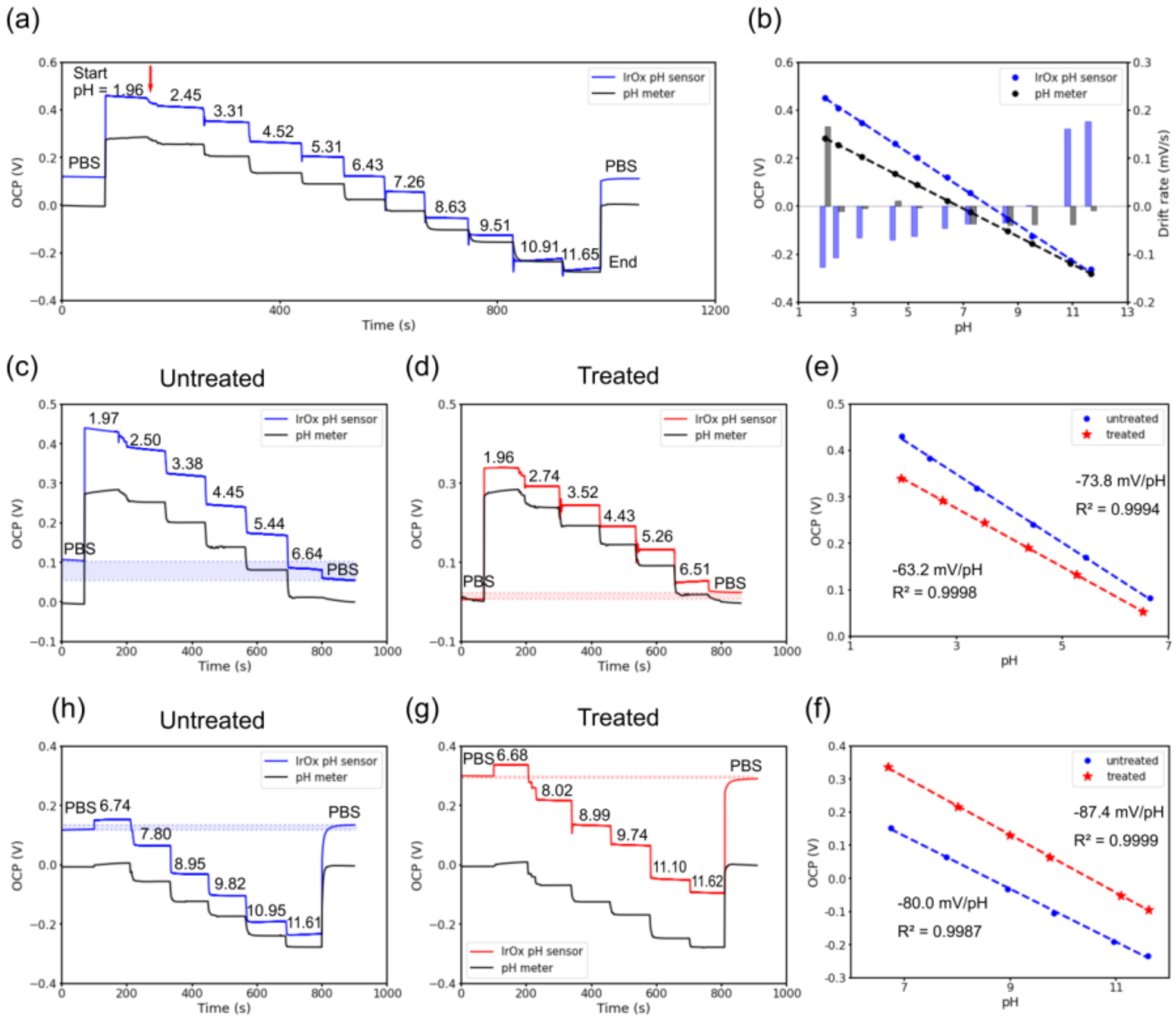

Figure 4. 12. The pH-sensing performance of the sensors, compared to a benchtop pH meter, in varying pH solutions during titrations.

Before treatment:

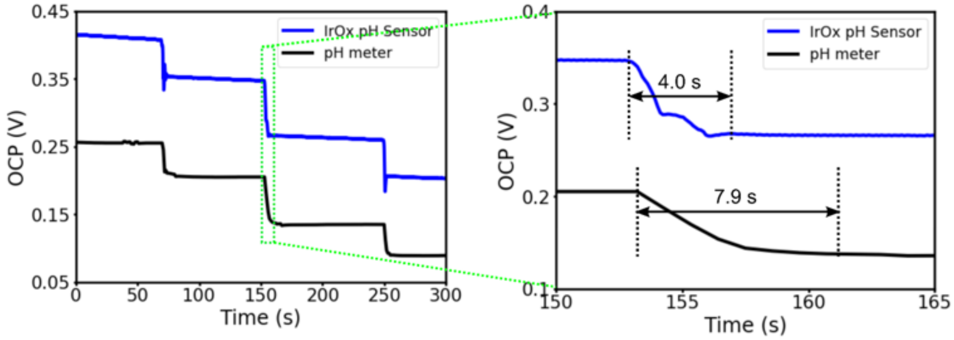

After treatment:

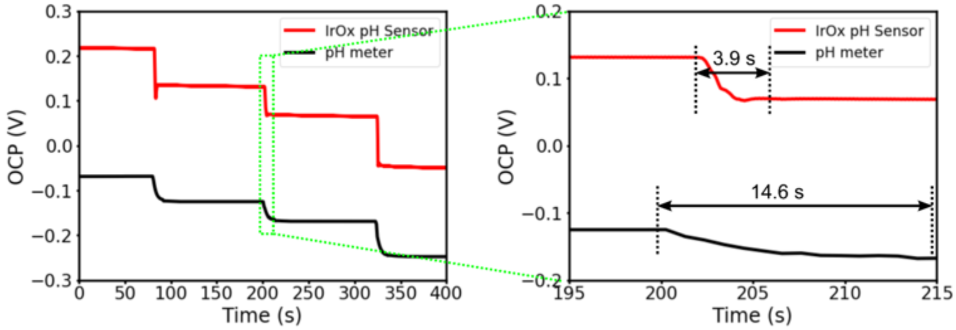

Figure 4. 13. Response rate comparisons between the IrOx pH sensors and the benchtop pH meter.

Since poor stability was observed in low pH or high pH regions, constant voltage treatments at different voltages were applied to shift the sensing window to these regions. The titrations were separately done in pH ranges of 2–7 and 7–12, with a comparison of the electrodes with and without the treatments. **Figure 4. 12. (c) and (d)** show the potential changes during the titration in the pH range from 2–7. The untreated sensor displayed a clear downward drifting trend in the acidic buffer, and the drift became mild when the pH was higher. After the treatment, the drift in the strong acidic region was improved. The OCP relative to the pH read by the pH meter was plotted in **Figure 4. 12. (e)**. After the treatment, better linearity was obtained. The coefficient of determination (R2) improved from 0.9994 to 0.9998. Similarly, in the basic titration from 7–12 in pH, the results were processed and displayed in **Figure 4. 12. (f)–(h)**. The freshly fabricated electrode had less drift than that in the acidic pH range. After the treatment, a slight improvement in stability can be seen. The R2 was improved from 0.9987 to 0.9999. Another parameter, hysteresis, was also induced to investigate the stability. Before and after the titration, the sensor's OCP was tested in 10X PBS. The difference between the two measurements was defined as hysteresis. In the 2–7 titration tests, the hysteresis was improved from −50.06 mV to 17.01 mV. In the 7–12 titration tests, the hysteresis was improved from 14.21 mV to −9.09 mV. The two freshly fabricated electrodes both had the sensing window centered in a weak basic region, similar to the electrode tested in the 2–12 titration.

Additionally, the linearity of the OCP-pH response demonstrated in the calibration curves offers an alternative approach to evaluating sensor stability. The impact of drift was assessed and detailed in the Supplementary Information, accompanied by **Figure 4. 14**. Sensor 1 and Sensor 2 were chosen for their minimal drift in 1 mM NaOH solution and 1 mM HCl solution, respectively. They were first tested in their optimal sensing window and subsequently exposed to a solution with a pH beyond their sensing range. **Figure 4. 14. (a)** shows OCP fluctuations throughout the experiments. **Figure 4. 14 (b**) is the calibration curves, generated from the OCP readings at the beginning of each segment, displayed satisfactory linearity in the absence of severe drifts. **Figure 4. 14(c) and (d)** represent drift rates for Sensor 1 and Sensor 2 during each recording segment, computed using the OCP readings at the initial and final points of the 5-minute experiment. The shaded areas represent the differences between the two OCP points gathered from each segment. These findings underscore the nonlinearity of pH calibration curves induced by drift, emphasizing the necessity of maintaining pH sensing within the sensor's effective range.

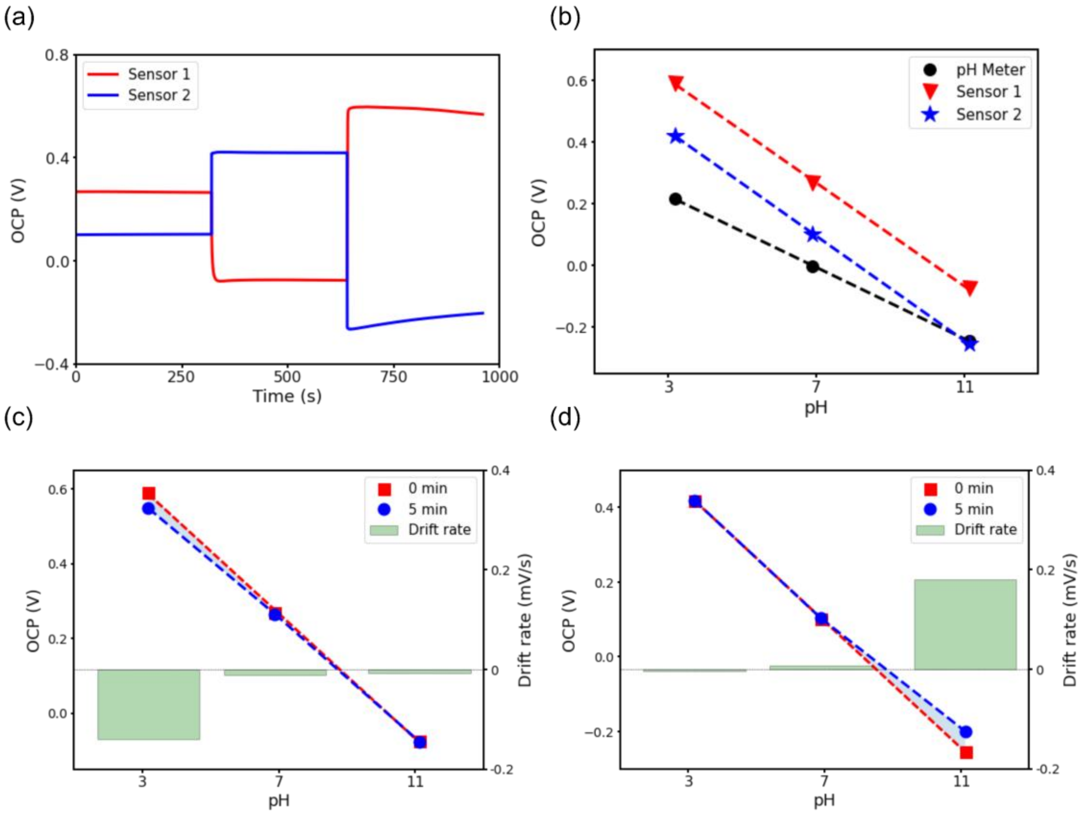

Figure 4. 14. Impact of drift on pH calibration curves.

4.4 Discussions and future directions

Despite research on electrodeposited IrOx pH sensors since the 1980s, various limitations still prevent their widespread use or commercialization. Previous studies have shown EIROF-based pH sensors to underperform compared to counterparts fabricated with other methods [40, 41, 43-46, 48, 50, 51]. Primary shortcomings comprise stability related issues, including potential drift, hysteresis, and non-linearity. Meanwhile, their performance drops significantly in higher acidic or basic pH conditions, substantially limiting their pH sensing range to only moderate pH zones. **Table 4. 2** provides a performance comparison of IrOx pH sensors, focusing on the pH sensing range and stability. Among the listed EIROF-based pH sensors, the typical sensing range remains constrained within 4–10, while sometimes drift significantly impacts the readings. Our initial tests corroborated these patterns. Therefore, to broaden EIROF's practical applicability, there's an urgent necessity for the enhancement of these sensors addressing these concerns.

Type	Sensitivity (mV/pH)	pH sensing range	Typical drift	Reference
Thermal Oxidized	58.9	1-13	1 mV in 10 h at pH 6.6	[35]
AIROF	76±2	2.5-9.98	25 mV in 1 h at pH 11.99	[45]
AIROF	60–80	3-10.5	12 mV in 1 h at pH 9.18	[48]
EIROF	73	3-11	10 mV in 100 s in 4 mM Urea	[50]
EIROF	56.6	4.01-9.18	10 mV in 10 min at pH 9.18	[51]

EIROF	70±5	4-9	…	[41]
EIROF	60-70	4-10	32 mV in 1 min. at pH 4	[46]
EIROF	65-85	4-10	137.5 mV in 1 hour at pH 12	Our study (Before treatment)
		beyond 2 or 12	9.8 mV in 1 hour at pH 12	Our study (After treatment)

Table 4. 2 Comparison of the stability and sensing range of IrOx pH sensors

Researchers have made efforts towards enhancing the stability and performance of IrOx pH sensors. One particular study suggested that storing these sensors in deionized water could mitigate potential drift over time, with observable improvements in 3–100 days [28]. Another research reported that as the dissolved oxygen can slowly oxidize the IrOx film, the pre-induction of oxygen into the system can further diminish drift [48]. These techniques, along with our proposed method, might operate through the same mechanism—stabilizing the oxidation state of the iridium oxide while moisturized, thereby improving stability. Our approach offers a practical and expedient solution, as CVT can alter the oxidation state within minutes. Furthermore, the flexibility in applying varying voltages allows the tuning of the oxidation state, thus controlling the sensing range of the pH sensors.

The EIROF pH sensors reported in this and other studies exhibit higher sensitivity, typical ranging from 65–85 mV/pH, as compared to anhydrous iridium oxide pH sensors produced using other techniques, which typically exhibit a sensitivity of around 59 mV/pH [28, 33, 35, 41]. The pH sensing mechanism has been widely discussed but a consensus has not been reached. We briefly review the possible mechanisms and explanations for the enhanced sensitivity [47, 48, 50, 51].

For anhydrous IrOx pH sensors, the pH sensing mechanism is generally agreed to involve the reaction of IrOx in two oxidation states, namely Ir(III) and Ir(IV), as expressed by the equation:

$$Ir_2O_3 + H_2O \rightleftharpoons 2\,IrO_2 + 2H^+ + 2e^-$$

(1)

This reaction involves the transfer of equal amounts of protons and electrons. According to the Nernst equation, pH sensitivity can be described as

$$pH\ sensitivity = -\frac{RT}{F} \times \frac{\#\ of\ protons\ involved}{\#\ of\ electrons\ involved}$$

(2)

where R, F and T represent the gas constant, Faraday constant, and temperature, respectively. As such, the reaction results in a Nernst response slope of −59 mV/pH at room temperature.

On the other hand, the pH sensing mechanism for hydrous IrOx pH sensors is believed to be more complex. The composition of hydrous IrOx includes various forms of iridium oxides and oxyhydroxides. Considering some redox couples with the existence of hydroxyl groups and their potential deprotonations without electron transfer, the overall reactions could eventually result in an increased slope in the Nernst equation. For example, the Ir(III) and Ir(IV) redox reaction

$$Ir(OH)_3 \rightleftharpoons IrO(OH)_2 + H^+ + e^-$$

(3)

and the possible deprotonations of the hydroxyl groups

$$Ir(OH)_3 \rightleftharpoons Ir(OH)_2O^- + H^+$$

(4)

$$IrO(OH)_2 \rightleftharpoons IrO(OH)O^- + H^+$$

(5)

Substitution of reactions (3) and (4) into reaction (2) yields

$$\begin{aligned}(1-x)\,Ir(OH)_3 + x\,IrO(OH)_2 \\ \rightleftharpoons (1-y)\,IrO(OH)_2 + y\,IrO(OH)O^- + (1+y-x)\ H^+ + e^-\end{aligned}$$

(6)

where x and y are in the range of 0 to 1, results in a number of involved protons/electrons ratio to be (1+y−x): 1. Therefore, the slope of the Nernst equation of this reaction can be expressed as −(1+y−x)(RT/F). Owing to the presence of numerous oxidation states and redox couples in conjunction with hydroxyl groups, the composition of the hydrous IrOx can vary considerably, and the eventual determine the sensitivity [28, 47].

Kötz *et al.* presented a cycle model for charge storage and oxygen evolution on AIROF electrodes based on their X-ray photoelectron spectroscopy (XPS) findings [52]. The model proposed that the evolution of oxygen is related the consecutive deprotonation steps that occur during the chemical transformation of $Ir(OH)_3$ to highly oxidized Ir(VI) state in IrO_3. The simultaneous uptake of a water molecule can trigger the reversal of Ir(VI) oxidation state to its tetravalent state, thus completing the cycle. The charge storage cycle model provides a possible explanation for the underlying mechanisms.

The application of the constant voltage treatment might facilitate the transfer of electrons in or out of the iridium compound, thereby resulting in a reformulation of its oxidation state. **Figure 4. 15** shows a current monitoring obtained from the counter electrode during a constant voltage treatment. The results indicated a rapid decrease in the current during the initial few seconds, which subsequently stabilized to a near-zero level for the remainder of the treatment period. We suppose that the reformulation of the iridium compound occurred primarily within the initial few seconds, which corresponded to the period of high electron transfer. This process gradually became milder over time, eventually resulting in the formation and maintenance of the new oxidation state. Meanwhile, upon voltage treatment application, we observed a clear color change on the electrode surface, indicating the composition or the oxidation state changes during the initial few seconds. Our observations complied with Kötz's model, which related the coloration of the iridium oxide film and the various forms of the iridium compound, as $Ir(OH)_3$ appears bleached, while other forms exhibited a colored appearance. With all the evidence, it is justifiable to deduce that the constant voltage treatment induced a rapid transition of the surface composition of the IrOx film, and the ensuing oxidation state changes further influenced the stability of pH sensing in different pH ranges.

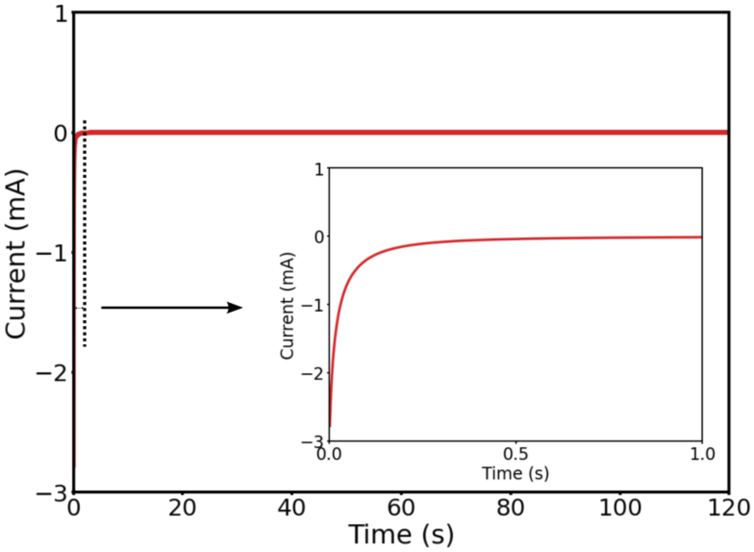

Figure 4. 15. A current monitoring by the counter electrode during a constant voltage treatment at 0.2 V.

The origin of drift and the presence of the sensing window can also be explained by the aforementioned mechanisms. **Figure 4. 16** demonstrates the 400-second OCP recordings following the constant voltage treatments at different voltages in PBS. When the applied voltages were too high or too low, the OCP was unable to maintain its original treatment voltages. Notably, the OCP trends following these "out of boundary" treatments closely resembled the OCP drift observed when the sensors were tested in the pH outside of their sensing windows. We therefore propose that the drift originates from a similar mechanism as the observed OCP trends after overvoltage treatments. Considering that both H^+ and e^- are involved in the cycle of deprotonations, we suppose that overloaded level of H^+ or OH^- beyond the sensing window may trigger further deprotonations in the cycle, leading to gradual charge transfers or oxidation state changes. Hence, the OCP were not able to maintain its original level, and drifts occurred. Through the use of constant voltage treatment, the oxidation state can be reformed to be more stable under certain hydrogen ion concentrations, there we observed the modification of sensing window.

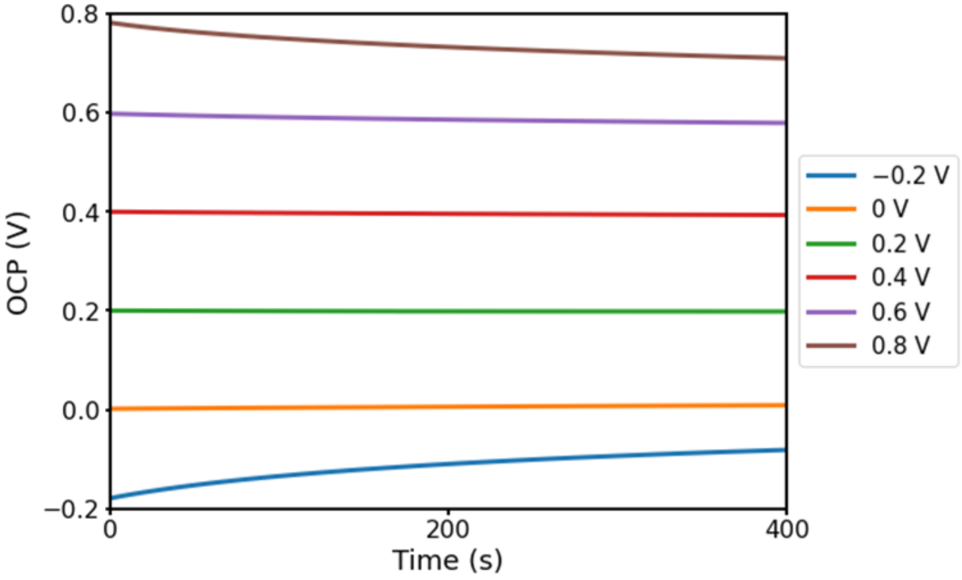

Figure 4. 16. OCP recorded in the treatment solution (PBS) after each constant voltage treatment at different voltages.

Our experimental results demonstrated a distinct correlation between the stability of the sensors and the implementations of constant voltage treatment. The speculations derived from our study primarily rely on empirical evidence. In order to thoroughly explicate the underlying mechanisms associated with the OCP drift, in addition to fully understand how the constant voltage treatment influences the stability, and to provide support for the proposed hypotheses, further examinations of surface chemistry is indispensable.

In conclusion, through the experiments conducted to investigate the stability of the pH sensors across different pH ranges, we observed a regular pattern of instability. We explored the existence of a "sensing window," where the sensor exhibited optimal stability. The sensor demonstrated comparable stability to a commercial pH meter when operating near the center of the sensing window. As a result, if the sensor consistently operates within the sensing window, drift is unlikely to be a significant issue. To address this, we proposed and implemented a constant voltage treatment to manipulate the sensing window. By altering the absolute potential of the sensors, their drift rates were adjusted accordingly, resulting in improved stability for long-term and repetitive pH measurements. This method was demonstrated to be effective in enhancing the linearity and stability of the sensors in both acidic and basic environments. With this method to enhance the performance, more reliable applications of EIROF-based pH sensors in various fields, including environmental monitoring, biomedical diagnostics, and industrial process control, can be foreseen.

CHAPTER 5 – Other Integrated Sensors and Devices

The wireless electrophysiological monitoring system and the pH sensors constitute the primary focus of this study. To cater to diverse research interests, the devices incorporate various features, facilitating numerous collaborative initiatives. This section provides a review of the unique designs inherent in the integrated sensors and the associated electronic systems.

5.1. Social Behavior and Underground Tracking of Rats

Electrophysiological (ExG) monitoring of small animal models constitutes an invaluable tool in numerous areas of research. Among these, the rat, as one of the most popular model organisms, frequently forms the focus of our investigative endeavors. At present, the majority of ExG monitoring devices proposed in the field remain tethered systems. Such systems, however, impose significant restrictions on the rat's ability to move freely, which can potentially confound behavioral observations and data interpretation.

Despite the availability of wireless alternatives, these technologies often present their own set of limitations. Most notably, they frequently display a significantly restricted operational range, thereby still imposing constraints on the spatial mobility of the rats, and necessitating the proximity of a receiver. While these restrictions might be considered tolerable in certain research contexts—given the typically small enclosures in which the animals are housed—these constraints still pose considerable challenges for research necessitating the observation of unimpeded, natural behavior.

It is thus crucial that we remain acutely aware of the potential implications these limitations may have on the validity of our research outcomes, and that we persist in our pursuit of technological advancements to enhance the ecological validity of our experimental designs. The forthcoming section will introduce a study entitled "Social Interactions among Free Rodents" to illustrate these challenges. The standard methodologies encounter significant difficulties when attempting to meet the specific demands of this research.

The intricate sociality of most animals, humans included, suggests that a comprehensive understanding of the human brain requires social animal models. The study of the social brain, however, poses substantial challenges, primarily due to the limited knowledge concerning the cerebral cortex's role in social interactions. Given that most human activities involve interactions and that social interaction difficulties are central to many psychological and psychiatric pathologies, there is a pressing need to elucidate the structure and function of neuronal networks that underpin social behavior.

A significant barrier to advancing our understanding of the social brain is the prevalent practice of housing animal models, predominantly rodents, in small, impoverished cages, which greatly curtail potential social interaction. Even when housed in larger gang cages, the environment remains a far cry from the natural conditions conducive to social interactions.

To address this issue, we propose pioneering the use of an 'enhanced naturalistic habitat' (ENH) within our vivarium, designed to closely replicate rodents' natural environments while allowing for observational studies. The medial forebrain cortex, crucial for social interactions in both rodents and humans, is of particular interest to us. Our aim is to examine its neuronal and neurotransmitter dynamics during social interactions in free-roaming rodents within the ENH, how these dynamics change as rodents separate or are left alone, and whether any synchronization of cortical activity occurs during interaction. Further, we seek to understand how these interactions alter the balance of neurotransmitters in freely roaming rats (**Figure 5. 1**).

Figure 5. 1. A clip of the ENH room camera monitoring

To investigate these questions, we will develop a state-of-the-art tracking system allowing us to continuously identify each rodent in the ENH, thereby enabling us to associate individual behavioral interactions with specific neuronal and neurotransmitter dynamics. We will also include control groups composed of caged rodents and single rodents in the ENH.

Three experiments will be conducted to validate sensor function, verify tracking and recording systems, and study brain synchronization at different exposure times to the ENH. The first experiment will validate Glu/GABA sensor function using potassium solution and Pentylenetetrazol (PTZ) injections. The second experiment will test the ENH tracking system in the naturalistic habitat and control settings. Finally, the third experiment will assess the impact of varying durations of exposure to the ENH on brain synchronization in rodents. It is hypothesized that prolonged exposure to the ENH will lead to increased brain synchronization among the rodents.

When considering the natural behavior of rodents in a wild setting, certain technological solutions may prove to be inadequate. Given that rats are predisposed to burrowing and spending a substantial portion of their time underground, any adopted method must be robust enough to withstand dirt and other environmental obstacles. In addition, due to the rapid movements of rats, a battery-powered system is the most practical solution for powering the device. Consequently, the design of the device should prioritize low power consumption to maximize operational time between charges. In light of these considerations, Bluetooth Low Energy (BLE) technology emerges as a promising option for data transmission. BLE offers a sufficient data rate to meet the requirements outlined above while also boasting low energy consumption. Additionally, the implementation of a mesh network can support the separate recording of more than ten objects simultaneously, further enhancing the versatility and applicability of the system to the social interaction research goals.

Technology	Approx. Accuracy	Power Consumption	Hardware Size	Environmental Conditions
Wi-Fi-based Indoor Positioning	5-15 meters	Moderate	Varies (Based on Wi-Fi routers)	Affected by building structure and other devices
Bluetooth Low Energy (BLE) Beacons	1-3 meters	Low	Small	Less affected by environment
Infrared (IR) Sensors	20 cm	Low to Moderate	Small	Affected by light and temperature conditions
Ultrasonic Systems	High	Moderate to High	Small to Medium	Affected by environmental noise
Radio Frequency Identification (RFID)	High, but short range	Low	Small	Less affected by environment
Visible Light Communication (VLC)	High	Low to Moderate	Small (integrated with LED lights)	Requires line of sight, affected by light conditions
Ultra-Wideband (UWB)	Up to 10 cm	High	Small to Medium	Less affected by walls and other obstacles
Magnetic Field Mapping	High	Low	Varies (Based on device used for measurement)	Affected by changes in local magnetic field

Table 5. 1. Comparisons of the indoor tracking technologies

Several alternatives were examined as potential high-precision localization technologies. Table 5. 1 outlines the typical performance metrics and other characteristics of common indoor tracking methods. Key factors for rat tracking in wilderness conditions include size, power consumption, accuracy, and ease of use. The size of the installed component must be compatible with other components of the wearable device. The device's power consumption should be sufficiently low to support weeks of uninterrupted data collection without necessitating a battery change. The localization's accuracy should fall within a 10 cm range. Moreover, given that rats burrow and tend to inhabit underground spaces, the tracking system must function effectively amidst obstacles such as soil and moisture. Taking into account all factors, Ultra-Wideband (UWB) stands out as a better technique for this application. UWB technology offers a robust solution for monitoring the locomotion of free-roaming rats across diverse environments. Its superior precision and capacity to penetrate obstructions render it exceptionally suitable for tracking small, agile animals in complex indoor conditions. In contrast to conventional tracking methodologies that may involve intrusive procedures or yield less accurate data, UWB enables non-invasive, real-time tracking with an accuracy up to 10 centimeters. Utilizing UWB, researchers can accrue detailed, dependable data concerning the movement patterns of rats, their social interactions, and their responses to environmental variations. This furnishes invaluable insights for disciplines such as neuroscience, behavioral psychology, and pharmaceutical research.

In the evolution of the previously discussed Version II rodent EEG board, a novel device was designed through the integration of an Ultra-Wideband (UWB) indoor tracking system. The DWM1001C module, developed by Decawave, occupies a vital position within this project as the linchpin of the UWB tracking system. It is specifically utilized to monitor the movements of rats in free-roaming conditions. The DWM1001C module is a high-precision UWB and BLE characterized by its compactness and the reliability and accuracy of its location data. It is particularly suited to our research needs due to its ability to provide real-time, high-accuracy positioning - with an impressive precision up to 10 centimeters - even within complex indoor settings. Moreover, the module's low energy consumption characteristics align impeccably with our prerequisite for continuous, long-term data acquisition. The module's diminutive size and lightweight nature make it conducive for seamless integration into wearable devices, thereby minimizing interference with the natural behavior of the rats. Consequently, the fusion of precision, power efficiency, and compact design embodied by the DWM1001C module renders it an optimal selection for our tracking requirements in this research endeavor.

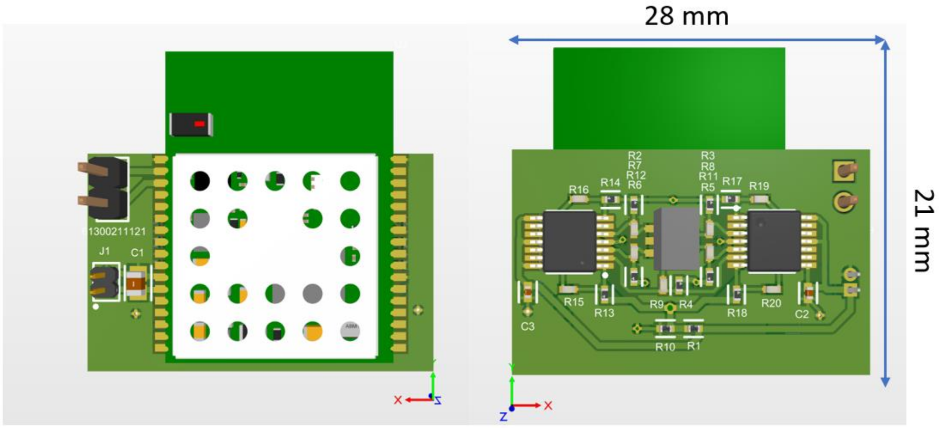

Top view

Bottom view

Figure 5. 2. UWB_BLE board demonstration

Figure 5. 2 presents a device where the DWM1001C serves as the primary microcontroller. This device boasts integrated Ultra-Wideband (UWB) tracking and brain signal processing capabilities. Nonetheless, due to the substantial dimensions of the DWM1001C (19.1mm x 26.2mm), which is hard to align with the head size of a rat, the potential for further size reduction is restricted. Consequently, given the current resources, we focused on enhancing the methodology for securely affixing the large PCB to the rats to ensure that their movements do not dislodge it.

Figure 5. 3 illustrates one of the strategies we have implemented to attain this goal. We designed a 3D-printed helmet equipped with an adjustable chin holder. Resin was selected as the material of choice to ensure a durable, smooth surface that can withstand the

rats' scratching and to provide partial transparency. Using dental cement, the device can be securely affixed to the rats, facilitating stable brain signal recording and tracking information.

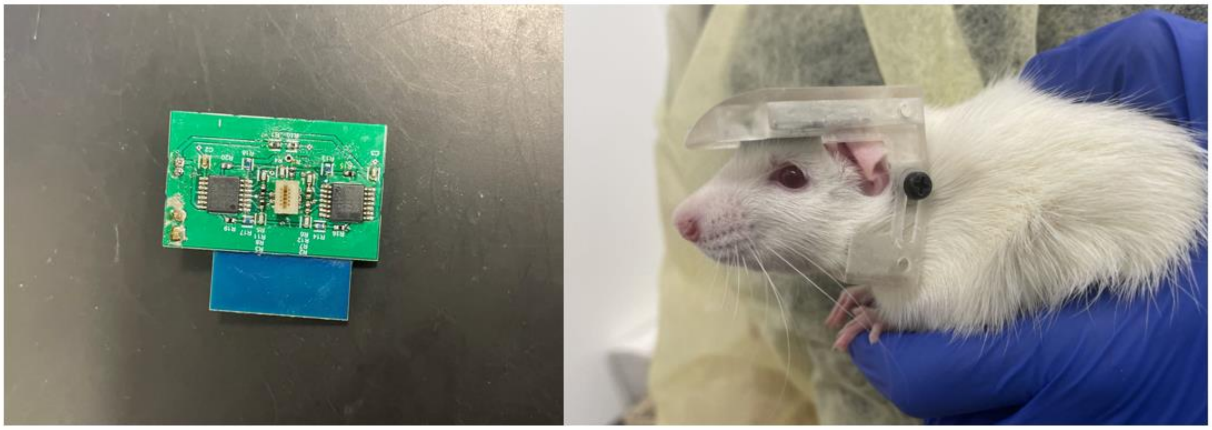

Figure 5. 3. The device and its installation on a rat with the help of a helmet

While the device is functional, it requires further refinements. The second generation of the rodent tracking device, based on the third version of the wearable rodent EEG device, demonstrates significant improvements in both size and power consumption. As the work has not yet been tested or published, a brief introduction and illustration will be provided in CHAPTER 6.

5.2. Test Tube-Integrated pH Sensors with a Wireless Power and Data Transmission System

A miniaturized wireless data acquisition system was developed to enable the pH measurement inside a test tube. The system was designed to be wirelessly powered and transmit data via BLE to the receiver. The power and communication circuit and coil fitted into the cap of a 50-mL test tube. **Figure 5. 4** provides an illustrative overview of the system components and diagrams. Subfigure (a) delineates the primary components of the system, which encompass the test tubes featuring integrated pH sensors and the wireless power transmitter panel strategically located atop the test tube rack. Subfigure (b) presents an exploded view of the pH sensor integrated within the tube. Subfigure (c) showcases a schematic representation of the electronic system's hardware implementation. The Printed Circuit Board (PCB) comprises a wireless power receiver and a management system, designed to supply power to all other board components. The signal procured from the electrodes undergoes amplification and digitization within the circuitry before its wireless transmission through BLE technology.

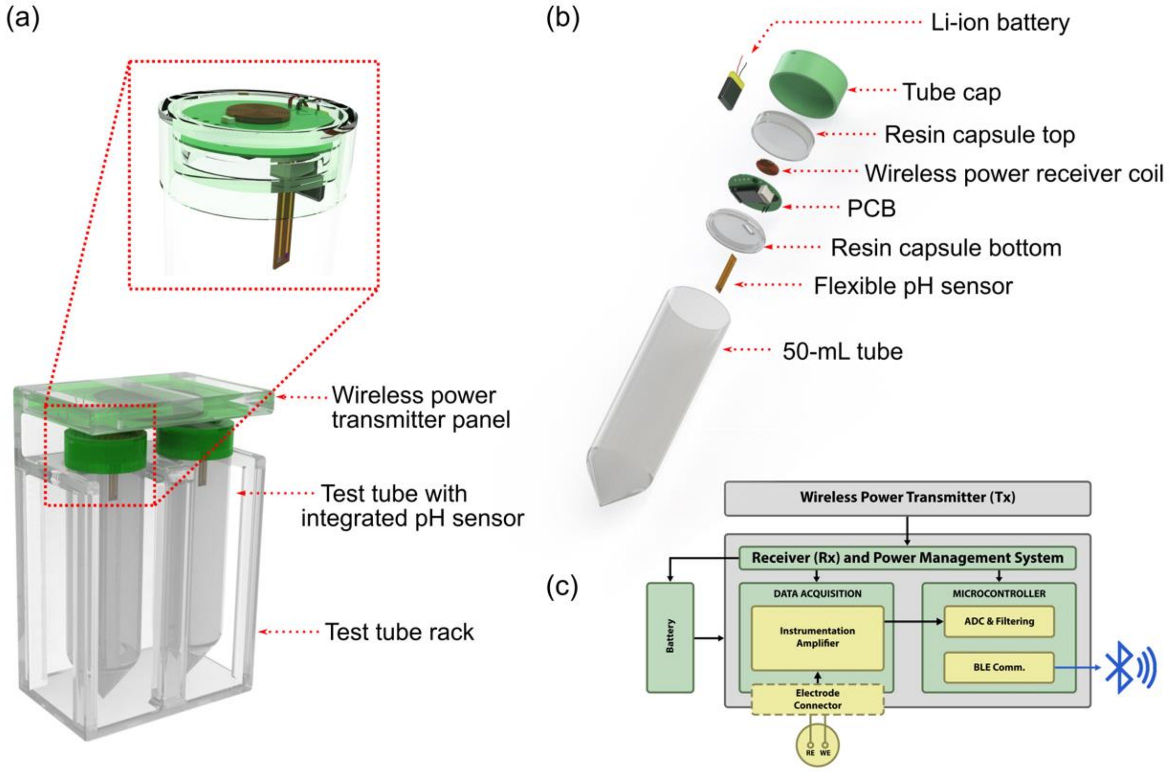

Figure 5. 4. Illustrations of the wireless tube-integrated pH monitoring system.

Figure 5. 5 delineates the hardware implementation of the wireless, test tube cap-integrated pH sensor. Subfigure (a) illustrates the circular PCB outfitted with a flexible pH sensor. Subfigure (b) details the primary components of the main pH sensing system, which include the test tube body, PCB enclosure cap, Lithium-ion battery, PCB with the embedded pH sensor, wireless power receiver coil, PCB enclosure, and test tube cap. Subfigure (c) offers a schematic representation of the data transmission path.

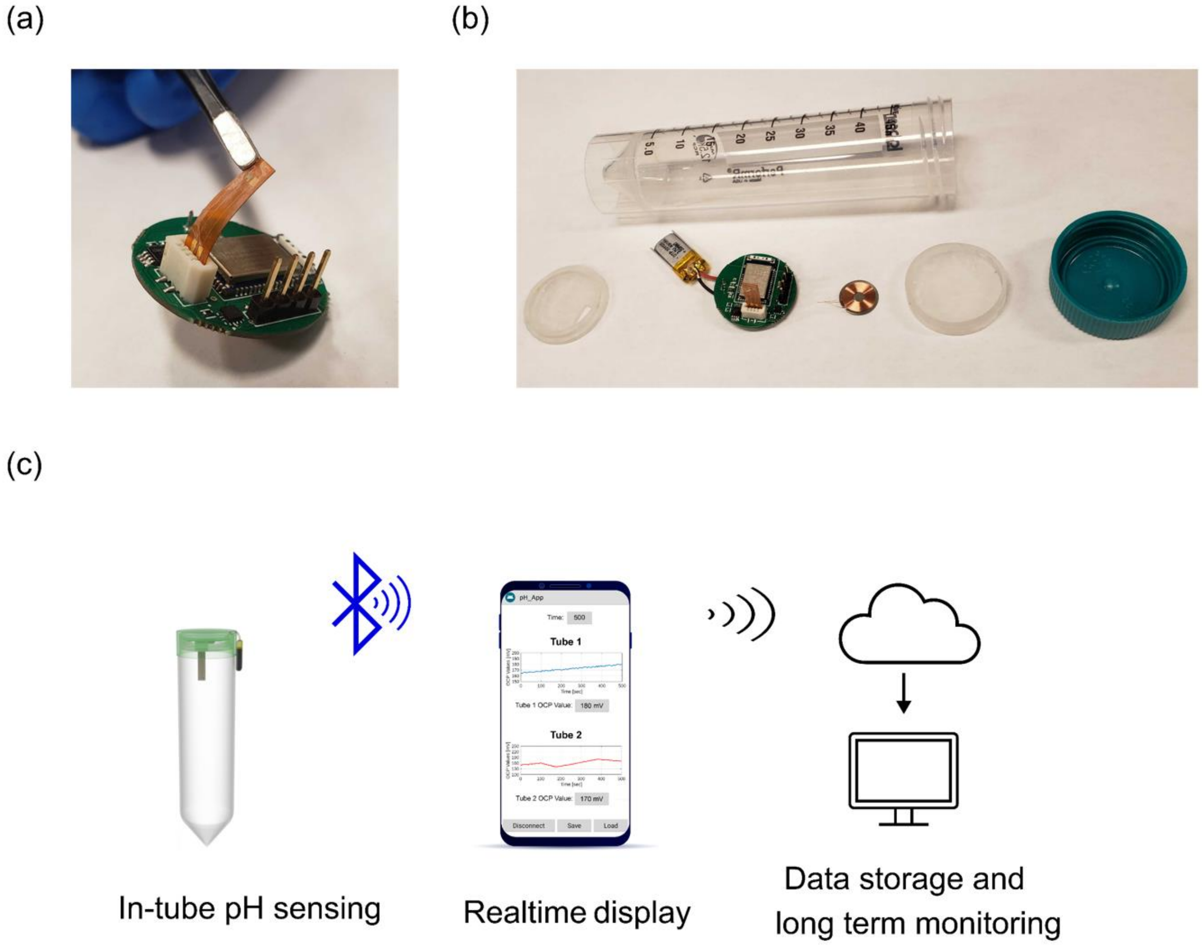

Figure 5. 5. Hardware implementation of the wireless test tube cap-integrated pH sensor.

Signals gathered are digitized and transmitted using Bluetooth Low Energy technology at a sampling rate of 10 samples per second. This data can be received and presented in real-time by a mobile phone, which subsequently uploads the data to a cloud system for secure storage. A laboratory computer can then download this data, facilitating the remote monitoring of pH changes.

The power management system incorporates a receiver coil with an inductance of 8.32 μH and a diameter of 12 mm, designed for inductive coupling, an AC/DC converter, a LTC4126 wireless charger (Analog Devices, MA, USA), and a compact Lithium-ion rechargeable battery. The receiver coil acquires energy from the transmitter coil positioned on the test-tube rack. The receiver LC resonant tank's frequency is harmonized with the transmitter's driving frequency of 216 kHz, with the received power being 31.5 mW.

The sensor gauges pH by comparing the potential difference between the working and reference electrodes to a calibration standard. A low-power instrumentation amplifier and an analog-to-digital converter (ADC) are employed to receive, process, and digitize the potential signals. Given the measurement range, a gain of 5 was selected to achieve the required resolution and fully utilize the input range of the 12-bit ADC integrated into the BLE microcontroller unit (MCU). The ADC sampling rate was set at 0.1 Hz, and the data were wirelessly transmitted via BLE for display on an Android smartphone application, enabling remote monitoring.

The miniaturized wireless data acquisition system was constructed on a circular-shaped PCB with a diameter of 26 mm and a thickness of 0.8 mm. The PCB dimensions were specifically designed to fit the cap of a 50-mL test tube. On the PCB's underside, the pH sensor signal was amplified using an INA321 microPower instrumentation amplifier (Texas

Instruments, TX, USA). The amplified signals were then digitized and transmitted wirelessly via Bluetooth Low Energy (BLE) using a Nordic nRF52832 module MDBT42Q (Raytac, TW). When the system was detached from the charging rack, it was powered by a 3.7 V, 40 mAh Lithium-ion battery, which provided sufficient power for over 24 hours of continuous measurement without the need for recharging.

CHAPTER 6 – Future Research Directions

6.1. Miniaturized Xenopus Wireless Wearable ExG Monitoring System with Integrated pH Sensor.

In amalgamating the previously delineated methodologies, a miniaturized, wireless wearable ExG monitoring system, integrated with a pH sensor, for Xenopus can be constructed. This device, akin to the basic framework of the rodent EEG board, is capable of recording a 4-channel EEG and a single-channel ECG, adhering to the electrode positioning specified in **Section 2.2.** Simultaneous ECG and EEG Monitoring on Xenopus Laevis

For the aquatic Xenopus, adaptations to the device are required to accommodate its unique environmental conditions. It necessitates a waterproof design, coupled with impeccable encapsulation. This aim can be achieved through the use of a 3D printed resin casing or a biocompatible interface between the implantation site and the animal's body. Meanwhile, the inclusion of a miniaturized pH sensor caters to the research interest of observing pH influence on aquatic creatures. Given that amphibians are highly sensitive to environmental fluctuations, partially attributable to their highly permeable skin, the combined approach of pH and ExG monitoring becomes a valuable tool for environmental study. **Figure 6. 1** illustrates the proposed miniaturized fully integrated bio-sensing system on Xenopus for environmental monitoring and studies.

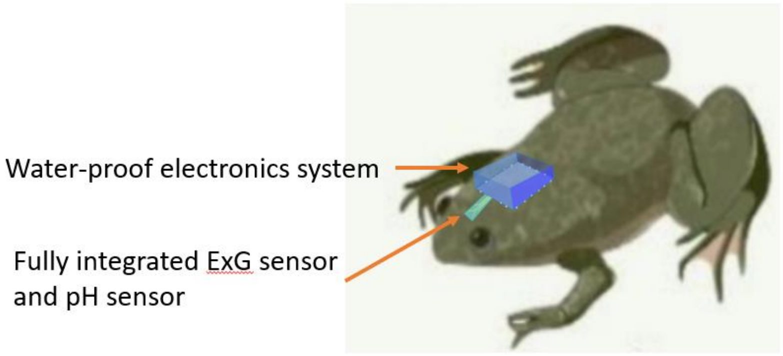

Figure 6. 1. Proposed miniaturized biosensing system on Xenopus

Furthermore, the Xenopus equipped with wearable sensors can function as a target for environmental monitoring. By delving further into the EEG data and extracting pertinent information, researchers can enhance their understanding of local environmental conditions and forecast impending changes.

6.2. Compact ExG Monitoring and Tracking Wearables on Rats

As delineated in preceding chapters, we've engineered a device capable of monitoring neural activity during unencumbered social interaction among mice in their natural habitat. The device, albeit functional, is yet to reach its optimal configuration. We anticipate that future advancements in technology, coupled with the rodent EEG board design we've proposed, will significantly enhance the device. We foresee it becoming smaller, more efficient, and more comfortable for the subjects, all while maintaining improved durability. These refinements will enable the rodents to navigate subterranean environments, engage in natural social interactions, and exhibit more instinctive behaviors such as confrontation. The ability to observe neural activity under these conditions will yield insights that closely mirror natural circumstances, thereby enhancing our understanding of animal behavior and neural dynamics in a significant and meaningful way.

As we edge closer to the future, the advent of next-generation Ultra-Wideband (UWB) micro-chips is paving the way for technological advancement. This progress is exemplified by the device we discussed in section 5.1, which is founded upon a DW1000 series UWB transceiver module. However, it's evident that there are still a multitude of challenges that need to be addressed.

In light of this, the new generation UWB chip introduced by Qorvo signifies a considerable stride forward, having made marked improvements from multiple perspectives. The salient enhancements that hold significant relevance to our project include these features. Firstly, the QM33110W's unique design is centered around optimizing low-power consumption, making it an excellent fit for battery-operated applications that necessitate energy conservation, or for those reliant on smaller, lower-capacity power sources such as coin cells. Secondly, the QM33110W's compact design, featuring a lower Bill of Materials (BOM) count and minimal solution footprint, could pave the way for reduced size and potentially more cost-effective device designs. Furthermore, its smaller package size (3.1 x 3.5 mm), a considerable reduction from the DW1000's dimensions (6.0 x 6.0 mm), affords the opportunity for more compact device designs. Finally, the QM33110W's compatibility with FiRa™, or "Fine Ranging", represents an essential standard aiming to guarantee high accuracy in UWB applications. This compatibility accentuates its suitability for applications necessitating highly precise ranging capabilities. These advancements present the QM33110W as a promising component in the future development of UWB devices.

The integration of the UWB transceiver module with Bluetooth Low Energy (BLE) communication remains a superior solution for this project. By uniting the devices detailed in Chapters 3.2.3 and 5.1, along with the presently accessible compact BLE-UWB module, we can accomplish our intended goals. The sole adjustment required is the replacement of the MDBT-42V BLE module with the ISP3080. This series represents the cutting-edge generation of UWB and BLE smart modules, offering universal coverage. The ISP3080 is furnished with built-in antennas for UWB, Bluetooth 5.1, Thread, Zigbee, ANT+, and NFC, thereby positioning it as an ultra-accurate module. The UWB component of the module draws upon the Qorvo QM33110, while the BLE element is built upon the Nordic Semi nRF52833. In spite of its compact dimensions of 12 x 10 x 1.0 mm, the module incorporates decoupling capacitors, a 38.4 MHz crystal for UWB, 32 MHz and 32.768kHz crystals for BLE, DC-DC converters, RF matching circuits, two antennas, and the wireless System on Chips (SoCs).

The ISP3080 is distinguished by its low power consumption and advanced power management, thereby enabling extended battery lifetimes of several months on a coin cell battery. One of the unique features of the ISP3080 is the integration of a multi-band antenna in the package, which supports both the BLE frequency band at 2.4 GHz and the UWB frequency band at 6.5 / 8.0 GHz. This innovation represents a novel concept developed by Insight SiP. Ultimately, the final device will provide substantial improvements over the current prototype: it will be significantly smaller (offering a size reduction of more than five times), it will consume much less power, and it will deliver superior location accuracy. These enhancements will ensure it meets the demands of the research studying social interactions among freely moving rats.

CONCLUSION

The field of electrophysiological research utilizing small animal models presents a crucial realm of scientific inquiry. The manifold advantages presented by small animals in research, from lower maintenance costs to reduced ethical concerns and early experimentation potential, have led to a surge in biosensor development and application. Although significant strides have been made, including the successful integration of traditional sensors like EEG and ECG in animals such as rodents, amphibians, and zebrafish, limitations persist. Challenges revolve primarily around the inconvenience and potential distress caused by wearable sensors, impacting the reliability of research results.

Recognizing these challenges, the field is shifting focus towards device miniaturization, made possible due to advancements in MEMS technology and innovations in the electronics industry. The goal is to produce compact, minimally invasive devices capable of unobtrusively integrating into the animals' daily lives and minimizing disruption of their natural behaviors. This emphasis on the reduction of sensor size and impact, while increasing function, would also have broader implications for the animals' welfare and the accuracy of the collected data.

Furthermore, supplementary sensors have been introduced to monitor additional biosignals and environmental factors, creating a more holistic approach to animal monitoring. The integration of wireless technology further enhances the convenience and compactness of these devices, leading to a more efficient and user-friendly design.

Our research has embraced this multidimensional approach, focusing on understanding all components of the biosensing system, from sensors to connectors, readout electronics systems, communication systems, to the power supply. A detailed comprehension of these elements is paramount in creating an integrated system, giving due consideration to all possible signal pathways and engineering integrity.

In conclusion, this research underscores the essential role of a comprehensive and intricate understanding of all components when designing biosensing systems for small animal models. The successful integration of miniature, non-invasive biosensors and supplementary sensors into these systems will not only foster a better understanding of the complex interactions between animals and their environment, but also facilitate advances in the broader fields of biology, ecology, and human health. Future research will undoubtedly focus on the continuous refinement of these systems, integrating cutting-edge technology to further reduce their impact on the animals, while also expanding their monitoring capabilities. Ultimately, these advancements will significantly contribute to our understanding of the physiological adaptations of animals in response to various environmental factors, with profound implications for both animal and human biology.

REFERENCES

[1] P. Mukherjee, S. Roy, D. Ghosh, S.K. Nandi, Role of animal models in biomedical research: a review, Laboratory Animal Research, 38(2022) 18.

[2] G.J. Lieschke, P.D. Currie, Animal models of human disease: zebrafish swim into view, Nature Reviews Genetics, 8(2007) 353-67.

[3] S. Kumar, P.K. Yadav, R. Srinivasan, N. Perumal, Selection of animal models for COVID-19 research, VirusDisease, 31(2020) 453-8.

[4] M.S. Rand, Selection of Biomedical Animal Models, in: P.M. Conn (Ed.) Sourcebook of Models for Biomedical Research, Humana Press, Totowa, NJ, 2008, pp. 9-15.

[5] A. Abbott, The Renaissance rat, Nature, 428(2004) 464-6.

[6] C. Riehle, J. Bauersachs, Small animal models of heart failure, Cardiovascular Research, 115(2019) 1838-49.

[7] J. Giacomotto, L. Ségalat, High-throughput screening and small animal models, where are we?, British Journal of Pharmacology, 160(2010) 204-16.

[8] M.L. Andersen, L.M. Winter, Animal models in biological and biomedical research-experimental and ethical concerns, Anais da Academia Brasileira de Ciencias, 91(2017).

[9] O.E. Varga, A.K. Hansen, P. Sandøe, I.A.S. Olsson, Validating animal models for preclinical research: a scientific and ethical discussion, Alternatives to Laboratory Animals, 38(2010) 245-8.

[10] X.H. Wehrens, S. Kirchhoff, P.A. Doevendans, Mouse electrocardiography: an interval of thirty years, Cardiovascular research, 45(2000) 231-7.

[11] D.J. Milan, I.L. Jones, P.T. Ellinor, C.A. MacRae, In vivo recording of adult zebrafish electrocardiogram and assessment of drug-induced QT prolongation, American Journal of Physiology-Heart and Circulatory Physiology, 291(2006) H269-H73.

[12] X. Xia, M. Vishwanath, J. Zhang, S. Sarafan, R.S.T. Torres, T. Le, et al., Microelectrode array membranes to simultaneously assess cardiac and neurological signals of xenopus laevis under chemical exposures and environmental changes, Biosensors and Bioelectronics, 210(2022) 114292.

[13] S.-J. Cho, D. Byun, T.-S. Nam, S.-Y. Choi, B.-G. Lee, M.-K. Kim, et al., Zebrafish as an animal model in epilepsy studies with multichannel EEG recordings, Scientific Reports, 7(2017) 3099.

[14] R.A. Bergstrom, J.H. Choi, A. Manduca, H.-S. Shin, G.A. Worrell, C.L. Howe, Automated identification of multiple seizure-related and interictal epileptiform event types in the EEG of mice, Scientific reports, 3(2013) 1483.

[15] D.L. Tomasello, D. Wlodkowic, Noninvasive Electrophysiology: Emerging Prospects in Aquatic Neurotoxicity Testing, Environmental Science & Technology, 56(2022) 4788-94.

[16] R. Rajanathan, T.M. Pedersen, M.B. Thomsen, H.E. Botker, V.V. Matchkov, Phenylephrine-Induced Cardiovascular Changes in the Anesthetized Mouse: An Integrated Assessment of in vivo Hemodynamics Under Conditions of Controlled Heart Rate, Frontiers in Physiology, 13(2022).

[17] F. Steijns, M.I. Tóth, A. Demolder, L.E. Larsen, J. Desloovere, M. Renard, et al., Ambulatory Electrocardiographic Monitoring and Ectopic Beat Detection in Conscious Mice, Sensors2020.

[18] H.-B. Han, B. Kim, Y. Kim, Y. Jeong, J.H. Choi, Nine-day continuous recording of EEG and 2-hour of high-density EEG under chronic sleep restriction in mice, Scientific Data, 9(2022) 225.

[19] A. Zayachkivsky, M.J. Lehmkuhle, F.E. Dudek, Long-term Continuous EEG Monitoring in Small Rodent Models of Human Disease Using the Epoch Wireless Transmitter System, Journal of Visualized Experiments : JoVE, (2015).

[20] T. Le, J. Zhang, X. Xia, X. Xu, I. Clark, L. Schmiess-Heine, et al., Continuous Electrocardiogram Monitoring in Zebrafish with Prolonged Mild Anesthesia, 2020 42nd Annual International Conference of the IEEE Engineering in Medicine & Biology Society (EMBC)2020, pp. 2610-3.

[21] H. Cao, F. Yu, Y. Zhao, X. Zhang, J. Tai, J. Lee, et al., Wearable multi-channel microelectrode membranes for elucidating electrophysiological phenotypes of injured myocardium, Integrative Biology, 6(2014) 789-95.

[22] T. Le, J. Zhang, A.H. Nguyen, R.S. Trigo Torres, K. Vo, N. Dutt, et al., A novel wireless ECG system for prolonged monitoring of multiple zebrafish for heart disease and drug screening studies, Biosensors and Bioelectronics, 197(2022) 113808.

[23] Y. Lee, K.J. Lee, J.-W. Jang, S.-i. Lee, S. Kim, An EEG system to detect brain signals from multiple adult zebrafish, Biosensors and Bioelectronics, 164(2020) 112315.

[24] J.-N. Shin, K.-B. Lee, W. Butterworth, S.-K. Park, J.-Y. Kim, S. Kim, Zebrafish EEG predicts the efficacy of antiepileptic drugs, Frontiers in Pharmacology, 13(2022).

[25] F. Ihlow, J. Courant, J. Secondi, A. Herrel, R. Rebelo, G.J. Measey, et al., Impacts of Climate Change on the Global Invasion Potential of the African Clawed Frog Xenopus laevis, PLOS ONE, 11(2016) e0154869.

[26] L. Manjakkal, D. Szwagierczak, R. Dahiya, Metal oxides based electrochemical pH sensors: Current progress and future perspectives, Progress in Materials Science, 109(2020) 100635.

[27] Z. Zhu, X. Liu, Z. Ye, J. Zhang, F. Cao, J. Zhang, A fabrication of iridium oxide film pH micro-sensor on Pt ultramicroelectrode and its application on in-situ pH distribution of 316L stainless steel corrosion at open circuit potential, Sensors and Actuators B: Chemical, 255(2018) 1974-82.

[28] X. Liu, Y. Pei, Y. Wang, X. Liu, X. Chen, C. Sun, et al., Performance of IrOx pH Sensor Prepared by Electrochemical and Thermal Oxidation, IEEE Sensors Journal, 22(2022) 12560-9.

[29] H. Jang, J. Lee, Iridium oxide fabrication and application: A review, Journal of Energy Chemistry, 46(2020) 152-72.

[30] M. Zea, A. Moya, M. Fritsch, E. Ramon, R. Villa, G. Gabriel, Enhanced Performance Stability of Iridium Oxide-Based pH Sensors Fabricated on Rough Inkjet-Printed Platinum, ACS Applied Materials & Interfaces, 11(2019) 15160-9.

[31] M. Khalil, S. Wang, J. Yu, R.L. Lee, N. Liu, Electrodeposition of Iridium Oxide Nanoparticles for pH Sensing Electrodes, Journal of The Electrochemical Society, 163(2016) B485.

[32] C.M. Nguyen, S. Rao, X. Yang, S. Dubey, J. Mays, H. Cao, et al., Sol-Gel Deposition of Iridium Oxide for Biomedical Micro-Devices, Sensors2015, pp. 4212-28.

[33] T.Y. Kim, S. Yang, Fabrication method and characterization of electrodeposited and heat-treated iridium oxide films for pH sensing, Sensors and Actuators B: Chemical, 196(2014) 31-8.

[34] A.N. Bezbaruah, T.C. Zhang, Fabrication of Anodically Electrodeposited Iridium Oxide Film pH Microelectrodes for Microenvironmental Studies, Analytical Chemistry, 74(2002) 5726-33.

[35] S. Yao, M. Wang, M. Madou, A pH Electrode Based on Melt-Oxidized Iridium Oxide, Journal of The Electrochemical Society, 148(2001) H29.

[36] T. Katsube, I. Lauks, J.N. Zemel, pH-sensitive sputtered iridium oxide films, Sensors and Actuators, 2(1981) 399-410.

[37] F. Deku, A. Joshi-Imre, A. Mertiri, T.J. Gardner, S.F. Cogan, Electrodeposited Iridium Oxide on Carbon Fiber Ultramicroelectrodes for Neural Recording and Stimulation, Journal of The Electrochemical Society, 165(2018) D375.

[38] Y. Lu, T. Wang, Z. Cai, Y. Cao, H. Yang, Y.Y. Duan, Anodically electrodeposited iridium oxide films microelectrodes for neural microstimulation and recording, Sensors and Actuators B: Chemical, 137(2009) 334-9.

[39] R.D. Meyer, S.F. Cogan, T.H. Nguyen, R.D. Rauh, Electrodeposited iridium oxide for neural stimulation and recording electrodes, IEEE Transactions on Neural Systems and Rehabilitation Engineering, 9(2001) 2-11.

[40] W.-D. Huang, H. Cao, S. Deb, M. Chiao, J.C. Chiao, A flexible pH sensor based on the iridium oxide sensing film, Sensors and Actuators A: Physical, 169(2011) 1-11.

[41] P. Marsh, L. Manjakkal, X. Yang, M. Huerta, T. Le, L. Thiel, et al., Flexible Iridium Oxide Based pH Sensor Integrated With Inductively Coupled Wireless Transmission System for Wearable Applications, IEEE Sensors Journal, 20(2020) 5130-8.

[42] P. Marsh, M. Huerta, T. Le, X. Yang, J.C. Chiao, H. Cao, Wireless Iridium Oxide-Based pH Sensing Systems, 2018 IEEE SENSORS2018, pp. 1-4.

[43] F. Mariani, M. Serafini, I. Gualandi, D. Arcangeli, F. Decataldo, L. Possanzini, et al., Advanced Wound Dressing for Real-Time pH Monitoring, ACS Sensors, 6(2021) 2366-77.

[44] R.H.G. Mingels, S. Kalsi, Y. Cheong, H. Morgan, Iridium and Ruthenium oxide miniature pH sensors: Long-term performance, Sensors and Actuators B: Chemical, 297(2019) 126779.

[45] M.L. Hitchman, S. Ramanathan, Evaluation of iridium oxide electrodes formed by potential cycling as pH probes, Analyst, 113(1988) 35-9.

[46] S. Carroll, R.P. Baldwin, Self-Calibrating Microfabricated Iridium Oxide pH Electrode Array for Remote Monitoring, Analytical Chemistry, 82(2010) 878-85.

[47] P. Steegstra, E. Ahlberg, Influence of oxidation state on the pH dependence of hydrous iridium oxide films, Electrochimica Acta, 76(2012) 26-33.

[48] W. Olthuis, M.A.M. Robben, P. Bergveld, M. Bos, W.E. van der Linden, pH sensor properties of electrochemically grown iridium oxide, Sensors and Actuators B: Chemical, 2(1990) 247-56.

[49] K. Yamanaka, Anodically Electrodeposited Iridium Oxide Films (AEIROF) from Alkaline Solutions for Electrochromic Display Devices, Japanese Journal of Applied Physics, 28(1989) 632.

[50] L.D. Burke, J.K. Mulcahy, D.P. Whelan, Preparation of an oxidized iridium electrode and the variation of its potential with pH, Journal of Electroanalytical Chemistry and Interfacial Electrochemistry, 163(1984) 117-28.

[51] L.D. Burke, D.P. Whelan, A voltammetric investigation of the charge storage reactions of hydrous iridium oxide layers, Journal of Electroanalytical Chemistry and Interfacial Electrochemistry, 162(1984) 121-41.

[52] R. Kötz, H. Neff, S. Stucki, Anodic Iridium Oxide Films: XPS-Studies of Oxidation State Changes and, Journal of The Electrochemical Society, 131(1984) 72.